Air Force Institute of Technology
AFIT Scholar

Theses and Dissertations   Student Graduate Works

6-17-2010

Electronic Structure of Lithium Tetraborate

David J. Wooten

Follow this and additional works at: https://scholar.afit.edu/etd

Part of the Inorganic Chemistry Commons, and the Optics Commons

**ELECTRONIC STRUCTURE OF
LITHIUM TETRABORATE**

DISSERTATION

David J. Wooten, Lieutenant Colonel, USA
AFIT/DS/ENP/10-J01

**DEPARTMENT OF THE AIR FORCE
AIR UNIVERSITY**

AIR FORCE INSTITUTE OF TECHNOLOGY

Wright-Patterson Air Force Base, Ohio

APPROVED FOR PUBLIC RELEASE; DISTRIBUTION UNLIMITED

The views expressed in this thesis are those of the author and do not reflect the official policy or position of the United States Air Force, the United States Army, the Department of Defense, or the United States Government. This material is declared a work of the U.S. Government and is not subject to copyright protection in the United States.

ELECTRONIC STRUCTURE OF
LITHIUM TETRABORATE

DISSERTATION

Presented to the Faculty

Graduate School of Engineering and Management

Air Force Institute of Technology

Air University

Air Education and Training Command

In Partial Fulfillment of the Requirements for the

Degree of Doctor of Philosophy

David J. Wooten, MS
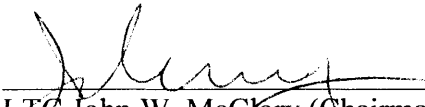
Lieutenant Colonel, USA

June 2010

APPROVED FOR PUBLIC RELEASE; DISTRIBUTION UNLIMITED

ELECTRONIC STRUCTURE OF
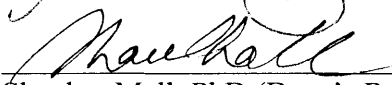# LITHIUM TETRABORATE

David J. Wooten, MS

Lieutenant Colonel, US Army

Approved:
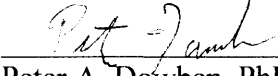
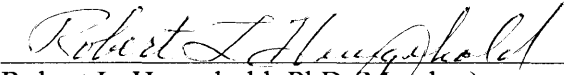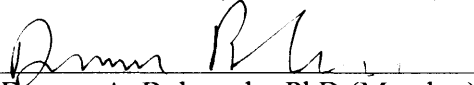|	
LTC John W. McClory (Chairman)	3 JUNE 10 Date
Shankar Mall, PhD (Dean's Representative)	6/3/10 Date
Peter A. Dowben, PhD (Member)	5/28/10 Date
Robert L. Hengehold, PhD (Member)	5/28/10 Date
James C. Petrosky, PhD (Member)	5/28/10 Date
Dursun A. Bulutoglu, PhD (Member)	5/28/10 Date

Accepted:

M. U. Thomas
Dean, Graduate School of
Engineering and Management

6/4/10
Date

Abstract

Due to many of its attributes, $Li_2B_4O_7$ provides a possible material for incorporation as either a primary or companion material in future solid state neutron detectors. There is however a lack of fundamental characterization information regarding this useful material, particularly its electronic configuration.   To address this, an investigation of $Li_2B_4O_7(110)$ and $Li_2B_4O_7(100)$ was undertaken, utilizing photoemission and inverse photoemission spectroscopic techniques. The measured band gap depended on crystallographic direction with the band gaps ranging from 8.9±0.5 eV to 10.1±0.5 eV. The measurement yielded a density of states that qualitatively agreed with the theoretical results from model bulk band structure calculations for $Li_2B_4O_7$; albeit with a larger band gap than predicted, but consistent with the known deficiencies of Local Density Approximation and Density Functional Theory calculations. The occupied states of both surfaces were extremely flat; to the degree that resolving periodic dispersion of the occupied states was inconclusive, within the resolution of the system. However, both surfaces demonstrated clear periodic dispersion within the empty states very close to theoretical Brillouin zone values. These attributes also translated to a lighter charge carrier effective mass in the unoccupied states. Of the two surfaces, $Li_2B_4O_7(110)$ yielded the more consistent values in orthogonal directions for energy states. The presence of a bulk band gap surface state and image potential state in $Li_2B_4O_7(110)$ was indicative of a defect-free surface. The absence of both in the more polar, more dielectric $Li_2B_4O_7(100)$ was attributed to the presence of defects determined

to be O vacancies. The results from $Li_2B_4O_7(110)$ were indicative of a more stable surface than $Li_2B_4O_7(100)$. In addition, Li 1s bulk and surface core level components were determined at the binding energies of -56.5 ± 0.4 and -53.7 ± 0.5 eV. Resonance features were observed along the [001] direction and were attributed to a Coster-Kronig process. Finally, the pyroelectric and piezoelectric character of $Li_2B_4O_7$ was explored more deeply and a non-zero, off-axis pyroelectric coefficient for the $Li_2B_4O_7(110)$ direction was discovered.

AFIT/DS/ENP/10-J01

For my family

Acknowledgements

I'd like to first give credit to our Lord Jesus Christ, through whom all things worthy are possible. Next, I must give credit to the most wonderful lady in my life, my long suffering wife. Many, many hours of sacrificing her time "single-parenting" have directly contributed to any success I might have had in this effort. As advisors and teachers go, I have had more than my fair share of good ones: Dave LaGraffe, Larry Burggraf, Jim Petrosky, and an especially understanding John McClory. Without Yaraslov Losovyj's patient instruction, I am certain AFIT would have exceeded their budget on student research within one month due to equipment replacement, alone. The company of supportive fellow students (and friends), Chris, Walt, Ty and Tom have been as key to my academic success as any. The technical expertise of David Wisbey, Ihor Ketsman and Jie Xiao all did their part in teaching me the techniques that were vital to my research. Finally, there is the "quantum" that is Peter Dowben. Symmetry selection rules dictate that "going for coffee in Lincoln's finer establishments" must yield the only allowable state that is Professor Peter Dowben—eminent physicist, outstanding teacher, with a bit of the plumber all rolled into a man of great character.

In closing, I'd like to attribute any success I might have experienced in this long endeavor to all of the above's determined efforts to keep an (often) hard-headed student on azimuth. Any failings in this regard are mine alone.

Table of Contents

List of Figures

xiii

xiv

List of Tables

**ELECTRONIC STRUCTURE OF
LITHIUM TETRABORATE**

1. Introduction

1.1. Overview

In this chapter, I will present essential background information regarding
$Li_2B_4O_7$. The current experimental research gaps with this material will also be
identified. This chapter will conclude with research goals and objectives to address an
overall research problem statement.

1.2. Background

With the fabrication of semiconducting boron carbide, a material suitable for the
fabrication of solid state neutron detectors [3-9], there has been a resurgence in research
focused on the development of boron based semiconductors for neutron detection. In
addition to the boron carbides [3-9], possible boron based semiconductors for solid state
neutron detectors include boron nitrides [10, 11], boron phosphides [12, 13], and the
lithium borates [14, 15].

Although lithium tetraborate ($Li_2B_4O_7$) has a much larger (6.3 to 10.1 eV) band
gap [16-19] than the boron carbides, boron nitrides, or boron phosphides, this class of
material has distinct advantages. The lithium borates are typically both translucent (when
undoped) and can be isotopically enriched to a high degree. $Li_2B_4O_7$ can be isotopically

1

enriched to 95 at% [6]Li and 97.3 at% [10]B from the natural 7.4 at% [6]Li and 19 at% [10]B [15]. Although not quite as high a cross section as [157]Gd, [10]B and [6]Li still have appreciable neutron capture cross sections. All three of these isotopes have neutron capture cross sections at least two orders of magnitude greater within the epithermal and below energy ranges when compared to that of most isotopes. This is depicted in Figure 1.1, below.
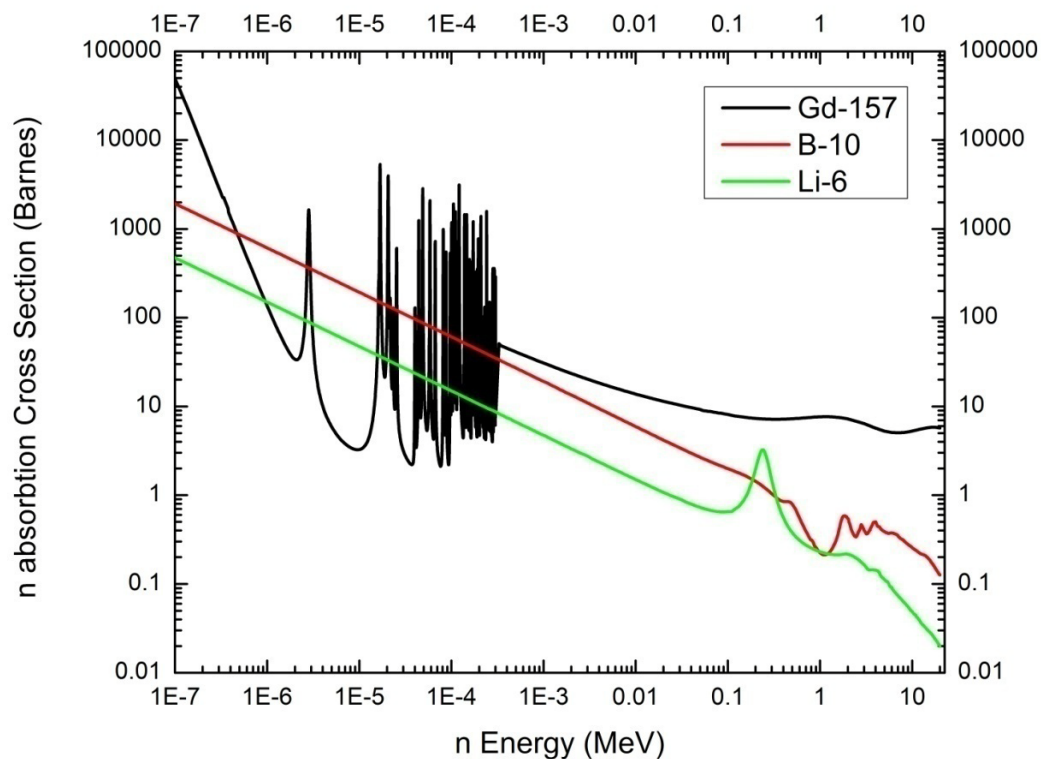
Figure 1.1. A comparison of total neutron absorption cross section of [157]Gd, [10]B and [6]Li for different neutron kinetic energies. (The data is courtesy of the Korea Atomic Energy Research Institute [1].)

Second, it has already been demonstrated in previous work that this material can be doped [2, 20, 21]. This is vital to mitigate the large, 6.2 to 10.1 eV, band gap [16-19]

and high resistivity, on the order of 10^{10} Ω·cm [14], of undoped lithium tertaborate. Without doping, this material may require a large voltage increasing the cost for a solid state detector application.

As a solid, crystalline material, lithium tetraborate has had a history of varied uses. Lithium tetraborate has potential applications not only in the areas of dosimetry scintillators, and scintillation detectors [14, 22]; but also has potential uses in the fields of acousto-electronics, and optics [14, 23-25]. It is a material of interest with respect to neutron opacity and detection [14, 15, 22, 24-26], and the details of its electronic structure are relevant to its applications [16-18, 27].

Despite its extensive and varied use, relatively little is known or held in common agreement outside its crystal characteristics. Lithium tetraborate belongs to the tetragonal space group I4$_1$cd, and possess 104 atoms per unit cell. This thirteen atom molecule, one of eight as part of the conventional unit cell, is displayed in Figure 1.2.
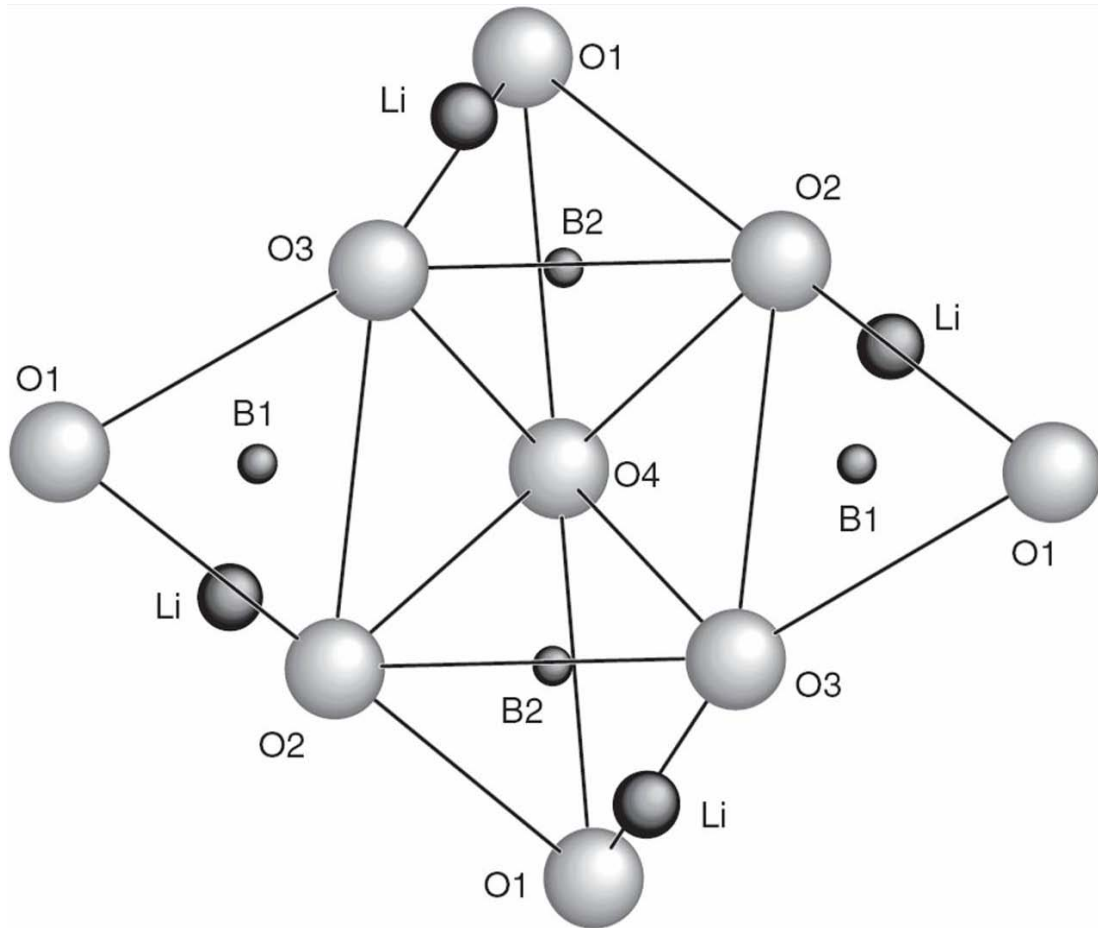
Figure 1.2: Basic structural unit of the $Li_2B_4O_7$ crystalline lattice [2]

The main crystal motif of lithium tetraborate is boron-oxygen complexes (B_4O_9). These consist of two planar trigonal BO_3 and two tetrahedral BO_4 groups with the lithium atoms localized at the interstices within the channels along the "c" (or Z axis) as depicted in Figure 1.2 [25, 27, 28]. As will be displayed in Chapter 4 (Figure 4.1) lattice parameters that characterize the unit cell have been determined to be $a = 9.477$ Å and $c = 10.286$ Å [25]. As indicated by Figure 1.2, Figure 4.1 and the large lattice parameters, the interstitially located Li atoms will have relatively little influence on each other, which will assist in the determination of the observed resonance to be discussed in Chapter 7.

Recent experimental work has focused on the valence band along with some of the core energy levels, but these values vary widely, covering a range of values differing by 2 or more eV; with some suggesting a valence band width of 15 eV. The experimental picture of the band structure is far from complete [27, 28]. The effective band gap has been theoretically determined as 7.5 eV [19], but this value is also suspect because lithium tetraborate is a correlated system. As a correlated system, lithium tetraborate possesses Coulombic repulsion or correlation energy that will lead to a band gap larger than can be accurately calculated. With the exception of the limited effort of Kuznetsov, et al. [27] in mapping the valence band states via XPS, several of the most recent lithium tetraborate research efforts have still not addressed lithium tetraborate electronic configuration completely [2, 14, 15, 19, 20, 22-33]. In fact, reliable information regarding effective band gaps, valence and conduction bands, effective masses of charge carriers, material stability, surface phenomena and whether or not contacts can be made with this material were still lacking as of the start of this research.

All of this electronic structure information is essential to making future optimal neutron detecting devices. Without an understanding of the surface conditions, one might unwittingly use a more chemically active crystal surface allowing for undesirable chemical reactions between constituents to occur, which could ultimately lead to a degradation of device performance. Without an understanding of the nature of charge carriers, particularly effective mass, it is difficult to establish a foundation from which to start designing an efficient solid state device. Knowledge of the electronic structure, doping characteristics and interface chemistry is important for any semiconductor modeling programs that might be utilized to find projected optimal doping

configurations. Key goals would also include the experimental determination of the band gap, and the density of states of the valence and conduction band edges. This information would be essential to correctly assess model calculations and undertake better predictions of any possible materials modifications. Finally, if it is impossible to make acceptable ohmic contacts with this material, its incorporation into a highly efficient neutron detector is suspect.

General theoretical modeling efforts [18] of lithium tetraborate have been previously published, but with very significant limitations. Since lithium tetraborate is a strongly correlated electron semiconductor, the methods for accurately calculating the detailed band structure, to include the band gap, do not currently exist, or are excessively computationally expensive, and the electronic configuration must be determined experimentally [34]. Even one of the most robust, theoretical models available, a GW calculation (further details of which will be addressed in Chapter 3), has not yet been accomplished. Even if such a theoretical model would be implemented, it would require confirmation by experiment; since the ground state correlation energy has not as yet been established. The present research provides the experimentally based information needed.

The goals of this research are two-fold. First, it is to develop an understanding of the band structure sufficient to model device energy band offsets, non-equilibrium charge distributions, and electron and hole masses. The second goal is to assess the different surfaces of lithium tetraborate for potential use in a future device. The former goal is an example of leap-frogging ahead of current device technologies by using a "materials by design approach" to efficiently engage in "devices by design".

6

1.3. Problem Statement

As stated above, there currently does not exist a clear experimental mapping of lithium tetraborate's electronic band structure. To that end, this research is inquiring, "To what degree can the lithium tetraborate crystal's electronic band structure be experimentally determined?"

1.4. Research Goal and Objectives

The goal for this research is to resolve the electronic band structure of lithium tetraborate. Experimental techniques were chosen that would accurately band map both surface and bulk features from shallow core energy levels up through E_{vacuum} for different crystal surfaces of lithium tetraborate; specifically, $Li_2B_4O_7(110)$ and $Li_2B_4O_7(100)$. Consequently, the research objectives are to characterize the valence and conduction bands along four high points of symmetry.

1.5. References

1. J. H. Chang, "Table of Nuclides: neutron cross sections of ^{157}Gd, ^{10}B, ^{6}Li," http://atom.kaeri.re.kr/, (2009).

2. V. M. Holovey, V. I. Sidey, V. I. Lyamayev, and P. P. Puga, "Influence of reducing annealing on the luminescent properties of $Li_2B_4O_7$:Cu single crystals," Journal of Luminescence, **126,** 408-412 (2007).

3. A. N. Caruso, R. B. Billa, S. Balaz, J. I. Brand, and P. A. Dowben, "The heteroisomeric diode," Journal of Physics: Condensed Matter **16,** 139-146 (2004).

4. B. W. Robertson, S. Adenwalla, A. Harken, P. Welsch, J. I. Brand, P. A. Dowben, and J. P. Claassen, "A class of boron-rich solid-state neutron detectors," Appl. Phys. Lett. **80,** 3644-3646 (2002).

5. B. W. Robertson, S. Adenwalla, A. Harken, P. Welsch, J. I. Brand, J. P. Claassen, N. M. Boag, and P. A. Dowben, "Semiconducting boron-rich neutron detectors," in I. S. Anderson and B. Guérard, eds. (SPIE, 2002), pp. 226-233.

7

6. S. Adenwalla, R. Billa, J. I. Brand, E. Day, M. J. Diaz, A. Harken, A. McMullen-Gunn, R. Padmanabhan, and B. W. Robertson, "Semiconducting boron-rich neutron detectors," in F. P. Doty, H. B. Barber, and H. Roehrig, eds. (SPIE, 2004), pp. 70-74.

7. K. Osberg, N. Schemm, S. Balkir, J. I. Brand, M. S. Hallbeck, P. A. Dowben, and M. W. Hoffman, "A Handheld Neutron-Detection Sensor System Utilizing a New Class of Boron Carbide Diode," IEEE Sensors J. **6,** 1531 (2006).

8. A. N. Caruso, P. A. Dowben, S. Balkir, N. Schemm, K. Osberg, R. W. Fairchild, O. B. Flores, S. Balaz, A. D. Harken, B. W. Robertson, and J. I. Brand, "The all boron carbide diode neutron detector: Comparison with theory," Mat. Sci. Engin. B **135,** 129 (2006).

9. E. Day, M. J. Diaz, and S. Adenwalla, "Effect of bias on neutron detection in thin semiconducting boron carbide films," J. Phys. D **39,** 2920-2924 (2006).

10. D. S. McGregor, T. C. Unruha, and W. J. McNeila, "Thermal neutron detection with pyrolytic boron nitride," Nucl. Instrum. Methods Phys. Res. A **591,** 530 (2008).

11. J. Uher, S. Pospisil, V. Linhart, and M. Schieber, "Efficiency of composite boron nitride neutron detectors in comparison with helium-3 detectors," Appl. Phys. Lett. **90,** 124101 (2007).

12. Y. Kumashiro, "Semiconductor of boron phosphide," J. Mater. Res. **5,** 2933 (1990).

13. Y. Kumashiro, T. Yokoyama, A. Sato, and Y. Ando, "Thermoelectric Properties of Boron and Boron Phosphide CVD Wafers," J. Solid State Chem. **133,** 314 (1997).

14. Sangeeta, K. Chennakesavulu, D. G. Desai, S. C. Sabharwal, M. Alex, and M. D. Ghodgaonkar, "Neutron flux measurements with a $Li_2B_4O_7$ crystal," Nuclear Instruments and Methods in Physics Research Section A: Accelerators, Spectrometers, Detectors and Associated Equipment, **571,** 699-703 (2007).

15. Y. V. Burak, V. T. Adamiv, I. M. Teslyuk, and V. M. Shevel, "Optical absorption of isotopically enriched $Li_2B_4O_7$ single crystals irradiated by thermal neutrons," Rad. Meas. **38,** 681-684 (2004).

16. D. Wooten, I. Ketsman, J. Xiao, Y. B. Losovyj, J. Petrosky, J. McClory, Y. V. Burak, V. T. Adamiv, R. Hengehold, and P. A. Dowben, "Electronic Structure of $Li_2B_4O_7$(110) and $Li_2B_4O_7$(100)," (2009).

8

17. D. Wooten, I. Ketsman, J. Xiao, Y. B. Losovyj, J. Petrosky, J. McClory, Y. Burak, V. Adamiv, and P. A. Dowben, "Differences in the Surface Charging at the (100) and (110) Surfaces of $Li_2B_4O_7$ in *Nuclear Radiation Detection Materials — 2009*," in *Nuclear Radiation Detection Materials — 2009,* D. L. Perry, A. Burger, L. Franks, K. Yasuda, and M. Fiederle, eds. (MRS, 2009), pp. 1164-L04-04.

18. M. M. Islam, V. V. Maslyuk, T. Bredow, and C. Minot, "Structural and Electronic Properties of $Li_2B_4O_7$," The Journal of Physical Chemistry B **109,** 13597-13604 (2005).

19. S. Kar and K. S. Bartwal, "Growth Optimization of $Li_2B_4O_7$ Crystals and Their Characterization," Cryst. Growth Des. **7,** 2522-2525 (2007).

20. V. T. Adamiv, Y. V. Burak, I. V. Kityk, J. Kasperczyk, R. Smok, and M. Czerwinski, "Nonlinear optical properties of $Li_2B_4O_7$ single crystals doped with potassium and silver," Optical Materials, **8,** 207-213 (1997).

21. D. Podgórska, S. M. Kaczmarek, W. Drozdowski, M. Berkowski, and A. Worsztynowicz, "Growth and Optical Properties of $Li_2B_4O_7$ Single Crystals Pure and Doped with Yb, Co and Mn Ions for Nonlinear Applications," Acta Physica Polonica A **107,** 507 (2005).

22. Y. V. Burak, B. V. Padlyak, and V. M. Shevel, "Radiation-induced centers in the $Li_2B_4O_7$ single crystals," Nuclear Instruments and Methods in Physics Research Section B: Beam Interactions with Materials and Atoms, **191,** 633-637 (2002).

23. A. Gurga, T. Juliano, Y. Gogotsi, S. N. Dub, N. V. Stus, D. A. Stratiichuk, and V. V. Lisnyak, "The mechanical properties of lithium tetraborate (100), (011) and (112) faces," Materials Letters, **61,** 770-773 (2007).

24. K. Uchida, K. Noda, T. Tanifuji, S. Nasu, V. Kirihara, and A. Kikuchi, "Optical absorption spectra of neutron-irradiated Li_2O," Physica Status Solidi (a) **58,** 557-566 (1980).

25. Y. V. Burak, B. V. Padlyak, and V. M. Shevel, "Neutron-Induced Defects in the Lithium Tetraborate Single Crystals," Radiation Effects & Defects in Solids **157,** 1101-1109 (2002).

26. A. O. Matkovskii, D. Y. Sugak, Y. V. Burak, G. I. Malovichko, and V. G. Grachov, "Radiation defect formation in lithium tetraborate (LTB) single crystals," Radiation Effects and Defects in Solids **132,** 371 (1994).

27. A. Y. Kuznetsov, A. V. Kruzhalov, I. N. Ogorodnikov, A. B. Sobolev, and L. I. Isaenko, "Electronic structure of lithium tetraborate $Li_2B_4O_7$ crystals. Cluster calculations and x-ray photoelectron spectroscopy," Physics of the Solid State **41,** 48 (1999).

9

28. V. T. Adamiv, Y. V. Burak, and I. M. Teslyuk, "Growth and properties of new nonlinear $LiKB_4O_7$ single crystals," Journal of Crystal Growth, **289,** 157-160 (2006).

29. P. A. Dowben, "Discussion regarding $Li_2B_4O_7$ Electronic Configuration," (May 21, 2008).

30. D. A. Keszler, "Synthesis, crystal chemistry, and optical properties of metal borates," Current Opinion in Solid State and Materials Science, **4,** 155-162 (1999).

31. N. I. Leonyuk, "Structural aspects in crystal growth of anhydrous borates," Journal of Crystal Growth, **174,** 301-307 (1997).

32. Y. Ono, M. Nakaya, T. Sugawara, N. Watanabe, H. Siraishi, R. Komatsu, and T. Kajitani, "Structural study of $LiKB_4O_7$ and $LiRbB_4O_7$: New nonlinear optical crystals," Journal of Crystal Growth, **229,** 472-476 (2001).

33. A. N. Shekhovtsov, A. V. Tolmachev, M. F. Dubovik, T. I. Korshikova, V. N. Baumer, B. V. Grinyov, and E. F. Dolzhenkova, "Growth, structure, and luminescence properties of LaB_3O_6 single crystals," Nuclear Instruments and Methods in Physics Research Section A: Accelerators, Spectrometers, Detectors and Associated Equipment, **456,** 280-283 (2001).

34. I. N. Yakovkin and P. A. Dowben, "The Problem of the Band Gap in LDA Calculations," Surface Review and Letters **14,** 481 (2007).

2. Motivation

2.1. Overview

In this chapter, I will present an overall motivation that might appeal to the Department of Defense and Department of Energy to conduct further research on $Li_2B_4O_7$. A hypothetical device that could incorporate $Li_2B_4O_7$ will also be presented, which will demonstrate this motivation. This chapter will conclude by outlining the remainder of the dissertation material.

2.2. The Larger Picture

Portable inspections require that security forces be outfitted with a neutron detection capability that is man-portable, reliable, sensitive, able to operate at or above room temperature, easy to operate and long-lived. Current approaches available include neutron scintillation detectors, [3]He detectors, solid-state conversion layer detectors, and neutron-absorbing semiconductor solid-state detectors. However, the current state of neutron detection is limited; especially in sensitivity and portability.

To understand this, one must consider the energy difference between the neutrons produced during a fission event compared to those at thermal energy, for which most neutron detectors are most efficient [1]. Typical fissile materials emit neutrons of kinetic energies of about 1.5 MeV and higher. For this reason, neutron detectors based on [3]He or Cd need a thick moderator layer in order to slow the neutrons down to about 30 meV or less. In this type of detector there is a reduction in the overall efficiency as well as an increase in size when the moderator is added to the detection material. Further, these devices need a large chamber for the [3]He gas; or, when considering CdZnTe, a large

11

high-voltage power source [2]. Worse yet, the dwindling supply of ^{3}He [3] may put the fabrication of low cost ^{3}He detectors at risk.

To alleviate these shortcomings, novel materials and device architectures are needed.   Gadolinium based oxides are one such material with one of the highest neutron absorption cross sections measured [4]. A solid state neutron detector utilizing gadolinium is certainly not new [5, 6]. Gd_2O_3 and Gd doped HfO_2 are just two recent examples of promising gadolinium compounds currently being explored [7-13]. Several potential device architectures incorporating ^{157}Gd in combination with ^{10}B also have merit. Two of the more promising incorporate either a p-n junction or a p-i-n tri-layer diode with a Gd-doped semiconductor on one side and single-crystal semiconducting lithium tetraborate layer on the other side of the heterojunction [2].

As an oxide, lithium tetraborate would be much more compatible at the interface with almost any Gd oxide because of the oxide-oxide interface potential. Chemical stability in particular is critical for realistic device incorporation; which makes lithium tetraborate a very valuable possible material in combination with rare earth oxides [2] particularly in a heterojunction device geometry. Complications of interface chemistry are important, because any potential companion material with a Gd oxide that did not incorporate oxygen as one of its constituents would cause an inherently more unstable interface. A chemically active interface site would reduce the number of charge carriers produced from decay due to neutron absorption and thus reduce the overall efficiency of the device. Further, over time, a device that incorporated a chemically active interface would eventually lead to degradation in device performance.

12

After considering this material's advantages from a neutron detection perspective, it might be worthwhile to consider a theoretical device that would incorporate lithium tetraborate into a simple heterojunction capable of detecting the decay of a boron or lithium nuclei that absorbed a neutron. Consequently, the next section will explore such a configuration.

2.3. A Hypothetical Device

The National Nuclear Security Administration's desire to "detect nuclear and radiological materials" [14] certainly provides a reasonable motivation for development of a more efficient neutron detection capability; perhaps one that could explore the possibility of incorporating lithium tetraborate. Picture a lithium tetraborate crystal forming one half of a semiconductor with some Gd oxide semiconductor forming the other half. The as-of-yet unspecified Gd oxide would be chosen such that it is both chemically stable with the lithium tetraborate, and matches the lattice of the lithium borate closely to minimize surface strain. This would allow a sufficient layer of the Gd oxide to be grown on the lithium tetraborate. The choice of dopants for both is still to be determined. At this point, it can only be said that one must be n type while the other will be p type in order for rectification to occur. The choice of crystal direction for lithium tetraborate and Gd oxide would have to be chosen so as to obtain the best crystal directions to optimize device performance. (Incidentally, the overall purpose of this research is to assist in answering that very question for the former material.) Good Ohmic contacts are then created on the side of the lithium tetraborate as well as the Gd

13

oxide via graduated, degenerative doping to complete the hypothetical device. Figure 2.1 depicts such a hypothetical device.
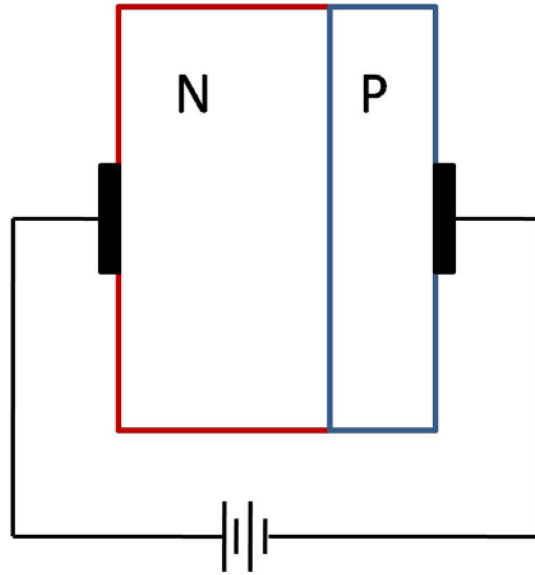
Figure 2.1. General overhead schematic of hypothetical solid state semiconducting device capable of neutron detection. Although it is portrayed in reverse bias to maximize the depletion region, it is not specified which constituent (lithium tetraborate or gadolinium oxide) is n or p type.

Assuming that the neutron enters the active volume and interacts with one of the isotopes of interest, one of two events occurs. An (n,γ) reaction will occur if the neutron is absorbed by the gadolinium, as in:

$$^{157}Gd + n \xrightarrow{yields} \,^{158}Gd + \gamma + X\text{-}rays + IC\ e^- + ACK\ e^- \qquad (1)$$
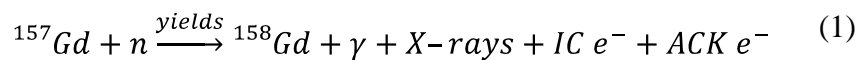
Or, if the neutron is captured by the lithium or boron constituents, one can expect an (n,α) reaction:

$$^{6}Li + n \rightarrow \,^{3}H^+ + \,^{4}He^{2+} + 4.5 MeV; \qquad (2)$$

and, either a 94% chance of

14

$${}^{10}B + n \xrightarrow{yields} {}^{7}Li(0.84Mev) + {}^{4}He(1.47Mev) + \gamma(0.48Mev); \quad (3)$$

or, a 6% chance that

$${}^{10}B + n \xrightarrow{yields} {}^{7}Li(1.02Mev) + {}^{4}He(1.78Mev). \qquad (4)$$
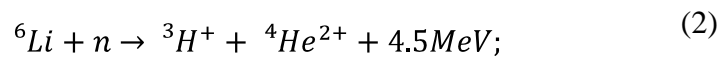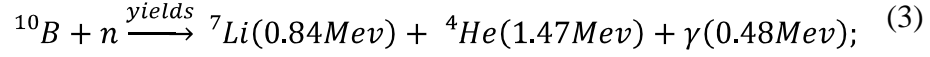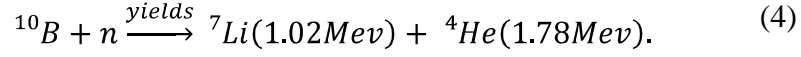
One can take advantage of the differences in pulse height spectra for the different isotopes or use the time domain pulse height to estimate the number of charge carriers produced; thus estimating the intensity of the source. This particular concept without the lithium tetraborate layer, along with subsequent modeling has been recently demonstrated. Data is shown in Figures 2.2 and 2.3 for a device built with n type Gd doped HfO_2 grown on p type silicon and irradiated with thermal neutrons [15].

15
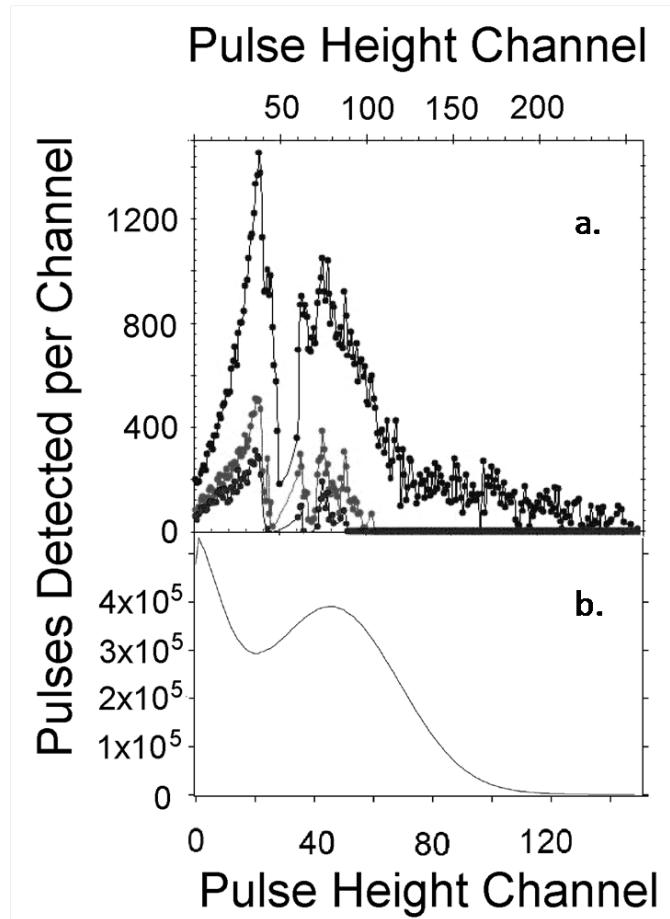
Figure 2.2. (a) Pulse height spectra of 10% Gd doped HfO$_2$ on Si(100), taken at the OSURR reactor for power levels 450, 250 and 125 kW. (b) Pulse height spectra were also taken using 15% Gd doped HfO$_2$ on n-type Si(100) with thermalized neutrons from a PuBe with a flux of 600 neutrons cm^{-2} s^{-1}incident on the diode. Figure courtesy of Schultz et al. [15]
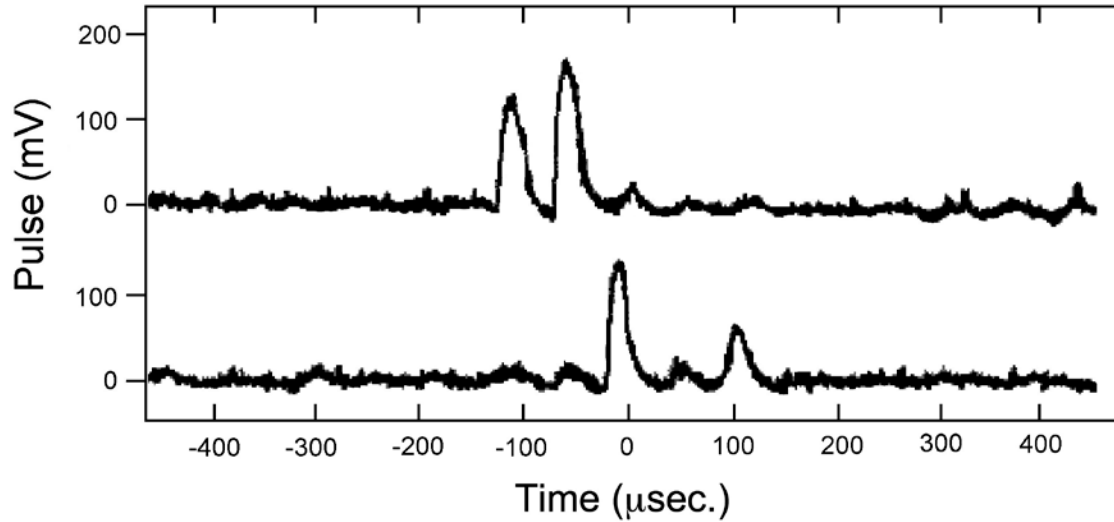
Figure 2.3. A sampling of time domain pulse trains using 15% Gd doped HfO$_2$ on n-type Si(100) samples with thermalized neutrons from a PuBe source with a flux of 2x10^4 neutrons cm^{-2} s^{-1}. The pulse height gain is divided by 3 electronically. Figure courtesy of Schultz et al. [15]

The cross-section of ^{157}Gd is high, approximately 460,000 b. at 0.1 eV [16], but the production of conversion electrons only occurs in 14% of ^{158}Gd decays. The true advantage is found in the significant neutron cross-section of ^{157}Gd, even at much greater neutron kinetic energies, 400 meV, compared to that of ^{10}B or ^{6}Li. This significantly improves the range of neutron energy absorption over current neutron devices that have substantial neutron absorption only at neutron energies less than 30 meV [2].

Following the same concept as that proposed in an existing provisional patent [17], a reasonable estimate of the energy of the initial neutron can be made by layering a series of the same type of semiconductors described previously that are collimated and sandwiched between neutron transparent material. One could then estimate a clear direction of the neutron source by arraying three sets of these same series of collimated semiconductors in three orthogonal directions.

2.4. General Overview

It is not the focus of this research effort to address all aspects presented in this chapter; but, rather to address one part of the overall roadmap. The focus of this research is to provide reliable, experimentally-derived information pertaining to the electronic band structure of lithium tetraborate in order to better determine how the different crystal directions would be optimally employed in any future device as described above.

To support this effort, the next chapter will address the physics of photoemission and will be followed by a presentation of the experimental set-up used to obtain this information. Following the experimental chapter, a series of chapters will summarize the results obtained in this research. The first of these chapters is titled "The Surface Core Level Shift for Lithium at the Surface of Lithium Borate", and presents the details of this phenomenon. The three subsequent results chapters, "Lithium Tetraborate (110) and (100) Experimental Band Gap", "The Occupied States of Lithium Tetraborate (110) and (100)", and "The Unoccupied States of Lithium Tetraborate (110) and (100)" cover the important aspects of the details of the electronic band structure and the surface characteristics for these two crystal orientations. The final results chapter, "$Li_2B_4O_7$ Hysteretic, Pyroelectric and Piezoelectric Attributes", will compare several interesting qualities about the two surfaces from the perspective of which surface will make a higher quality interface. This research will conclude with this author's opinion of the most relevant future research that will support further the design of neutron detectors incorporating lithium tetraborate as described in this chapter.

2.5. References

1. G. Knoll, "Fast Neutron Detection and Spectroscopy," in *Radiation Detection and Measurement,* (John Wiley & Sons, Inc., 2000), pp. 537.

2. P. Dowben, "DNDO Project Description" (2008).

3. R. L. Kouzes, "The ^{3}He Supply Problem - Pacific Northwest National Laboratory," PNNL18388 (2009).

4. J. Parrington, H. Knox, S. Breneman, E. Baum, and F. Feiner, *Nuclides and Isotopes* (General Electric Co. and KAPL, Inc., 1996).

5. T. Aoyama, Y. Oka, K. Honda, and C. Mori, "A neutron detector using silicon PIN photodiodes for personal neutron dosimetry," Nuclear instruments & methods in physics research.Section A, Accelerators, spectrometers, detectors and associated equipment **314,** 590 (1992).

6. A. Mireshghi, "High efficiency neutron sensitive amorphous silicon pixel detectors," Nuclear Science, IEEE Transactions on **41,** 915-921 (1994).

7. Y. B. Losovyj, I. Ketsman, A. Sokolov, K. D. Belashchenko, P. A. Dowben, J. Tang, and Z. Wang, "The electronic structure change with Gd doping of HfO_2 on silicon," Appl. Phys. Lett. **91,** 132908-3 (2007).

8. Y. Losovyj and P. A. Dowben, "Changes in electronic structure through a disorder transition in gadolinium adlayers on W(112)," J. Alloy. Compd. **401,** 155-159 (2005).

9. Y. Losovyj, I. Ketsman, E. Morikawa, Z. Wang, J. Tang, and P. Dowben, "Optimization of the 3m TGM beamline, at CAMD, for constant initial state spectroscopy," Nuclear Instruments and Methods in Physics Research Section A: Accelerators, Spectrometers, Detectors and Associated Equipment, **582,** 264-266 (2007).

10. D. LaGraffe, "Electronic and Magnetic Properties of Rare Earth Ferromagnets in Constrained Systems: An Experimental Case Study of Gadolinium and Terbium Ultrathin Films," (1990).

11. I. Ketsman, Y. B. Losovyj, A. Sokolov, J. Tang, Z. Wang, K. D. Belashchenko, and P. A. Dowben, "The *n*-type Gd-doped HfO_2 to silicon heterojunction diode," Applied Physics A-Materials Science & Processing **89,** 489 (2007).

12. I. Ketsman, Y. B. Losovyj, A. Sokolov, J. Tang, Z. Wang, M. L. Natta, J. I. Brand, and P. A. Dowben, "Gd-doping of HfO_2," Applied Surface Science **254,** 4308-4312 (2008).

13. D. Wooten, Y. B. Losovyj, J. Petrosky, J. McClory, J. Tang, W. Wang, and P. A. Dowben, "Surface charging of n-type Gd_2O_3 and HfO_2 thin films in *Rare-Earth Doping of Advanced Materials for Photonic Applications*," (2008), pp. D07.

14. U. S. Department of Energy National Nuclear Security Aministration, "Nuclear Nonproliferation," http://nnsa.energy.gov/nuclear_nonproliferation/index.htm.

15. D. Schultz, B. Blasy, J. C. Santana, J. C. Petrosky, J. McClory, D. LaGraffe, A. J. Brand, J. Tang, J. Tang, W. Wang, N. Schemm, S. Balkir, M. Bauer, I. Ketsman, R. W. Fairchild, Ya. B. Losovyj, and P. A. Dowben, "The K-shell Auger Electron Spectrum of Gadolinium Obtained Using Neutron Capture in a Solid State Device." J. Physics D, **43**, 7, 075502, (2010).

16. J. H. Chang, "Table of Nuclides: neutron cross sections of ^{157}Gd, ^{10}B, ^{6}Li," http://atom.kaeri.re.kr/, (2009).

17. A. Carusso, P. A. Dowben, J. McClory, and J. Petrosky, "Gd-doped EuO Solid-state Neutron Detector," (2009).

3. General Theory

3.1. Overview

This chapter presents the general theory central to band structure, as applied to lithium tetraborate ($Li_2B_4O_7$), a general discussion on photoemission, and the pertinent theoretical aspects for the major experimental techniques utilized during this research. In order to discuss the techniques necessary to map the electronic structure of lithium tetraborate, a brief summary of band structure will be useful. Both angle-resolved photoemission spectroscopy (ARPES) and angle-resolved inverse photoemission spectroscopy (IPES) will be discussed in more detail since these methods were the critical means used to characterize the valence and conduction bands, respectively. Light polarization dependent photoemission will also be covered briefly because of its ancillary use in the proposed research. Finally, this chapter will conclude with a brief discussion on current theoretical models and their shortcomings with regard to modeling lithium tetraborate.

3.2. Band Structure

Valence electrons, atomic and molecular bonds, solids

Almost all of the properties of importance for the elements can be determined by the electrons occupying the highest energy orbitals. These electrons are known as valence electrons. Those electrons occupying filled shells closer to the nucleus are known as core electrons and--with rare exception--have little involvement with molecular bonds. The valence electrons of interest for lithium tetraborate are one in the $2s^1$, three in $2s^22p^1$,

and six in the $2s^2 2p^4$ for Li, B and O, respectively. At a molecular level, the presence of these electrons within s and p atomic orbitals translates into orbital hybridization and molecular bonds.

Moving up in system complexity, from a simple molecule to a solid, the number of electrons per atom (or unit cell) remains conserved. However, in solids there are vast numbers of interacting electrons, i.e. fermions, that must not occupy the same state. The fundamental difference between the molecule and the solid is that instead of splitting into a single bonding and antibonding state, the atomic levels will split into bands of states distributed between the filled and unfilled bands, potentially separated by an insulating band gap [1]. In a crystalline system, wave vector dependence is established, which provides the bandwidth. For a wide band gap semiconductor like lithium tetraborate, the occupied bonding bands are known as valence bands and are completely filled whereas the unoccupied bands become the conduction bands. The conduction bands remain practically empty at temperatures up to room temperature, apart from additions due to thermal or optical excitation. Further, there is a large energy gap between the valence and conduction band in which there are no available states. Of course the latter presumes a perfect crystal with no surface states, defects, or other such phenomena that would theoretically provide a non-zero density of states in the forbidden region.

The Tight Binding Approximation model and the origin of hybridization

Lithium tetraborate forms a solid crystal with insulator-like qualities. Given this, the tight-binding approximation (TBA) model [2] is the logical first choice to qualitatively describe the intrinsic band structure prevalent within the crystal. This particular approximation is able to correct for the atomic-like orbitals from Li, B and O

22

atoms, but not in a manner as to render the atomic description completely irrelevant. A feature to be expected from this solid is the presence of hybrid bonds. To understand this feature in the context of the tight binding approximation model, one is referred to Ashcroft and Mermin's general formulation of the TBA [2]. A summary of the salient points of the TBA follows for a monatomic lattice which can also be applied for a non-monatomic lattice with a simple substitution.

The TBA starts with the assumption that within the vicinity of each lattice point the full crystal Hamiltonian, H, is approximated by the single atomic Hamiltonian, H_{at}, with its discrete, allowable energy states, E_n, located at the lattice point and that bound levels of the atomic Hamiltonian are well localized. Therefore the atomic state functions, ψ_n, are at approximately zero distance away from the lattice site:

$$H_{at}\psi_n = E_n\psi_n. \tag{5}$$

Expressing the crystal Hamiltonian as the atomic Hamiltonian plus a correction term, $\Delta U(\mathbf{r})$, the Hamiltonian becomes

$$H = H_{at} + \Delta U(\mathbf{r}). \tag{6}$$

Recalling that the TBA crystal wave function satisfies the Bloch condition,

$$\psi(\mathbf{r} + \mathbf{R}) = e^{i\mathbf{k}\cdot\mathbf{R}}\psi_n(\mathbf{r}); \tag{7}$$

with $\psi(\mathbf{r} + \mathbf{R}), \mathbf{R}, \mathbf{k},$ as the eigenstate at location, $\mathbf{r}$ + Bravais lattice vector, $\mathbf{R}$, and wave vector, $\mathbf{k}$; the crystal wave function is:

$$\psi(\mathbf{r}) = \sum_{\mathbf{R}} e^{i\mathbf{k}\cdot\mathbf{R}} \sum_{n} b_n\psi_n(\mathbf{r} - \mathbf{R}), \tag{8}$$

with b_n as the expansion coefficient to satisfy a particular eigenstate. This equation leads to a secular equation that will determine the energy levels $\varepsilon(\boldsymbol{k})$ and expansion coefficients (b_m, b_n):

$$(\varepsilon(\boldsymbol{k}) - E_m)b_m = \qquad (9)$$

$$-(\varepsilon(\boldsymbol{k}) - E_m)\sum_n\left(\sum_{R\neq 0}\int \psi_m^*(\boldsymbol{r})\psi_n(\boldsymbol{r}-\boldsymbol{R})e^{i\boldsymbol{k}\cdot\boldsymbol{R}}d\boldsymbol{r}\right)b_n$$

$$+\sum_n\left(\int \psi_m^*(\boldsymbol{r})\varDelta U(\boldsymbol{r})\psi_n(\boldsymbol{r})d\boldsymbol{r}\right)b_n$$

$$+\sum_n\left(\sum_{R\neq 0}\int \psi_m^*(\boldsymbol{r})\varDelta U(\boldsymbol{r})\psi_n(\boldsymbol{r}-\boldsymbol{R})e^{i\boldsymbol{k}\cdot\boldsymbol{R}}d\boldsymbol{r}\right)b_n$$

All corrections necessary to the atomic potential are captured by the periodic crystal potential, $\varDelta U(\boldsymbol{r})$.

The right hand side of the equation is small by nature. Therefore, $(\varepsilon(\boldsymbol{k}) - E_m)b_m$ is always small. Consequently, unless $\varepsilon(\boldsymbol{k}) \sim E_m$, b_m will be small. We can further say that since this is the TBA, individual wave functions are atomic-like by nature, with little overlap; and, therefore, $\varepsilon(\boldsymbol{k})$ must be close to an atomic energy level. To be close to the atomic energy level, dispersion and $\varepsilon(\boldsymbol{k})$ variations must be generally small. Therefore, all b_m except those associated with that level or close to that level in energy must be small. This will produce the qualitative "s" and "p" bands that are anticipated. If there is enough variation of $\varepsilon(\boldsymbol{k})$ with regards to $\boldsymbol{k}$ to become close to other atomic orbital energy levels—p approaching an s for example—the summation over n terms on the right hand side of Equation (9) must also account for the degenerate electronic atomic states. This is the origin of hybridized bands.

24

A linear combination of atomic orbitals obtained from Equation (9) of, e.g. two p orbitals, is simply another p orbital with a different orientation [3]; with the caveat that symmetry restrict them from being completely identical of course. A pertinent example of this would be the lithium tetraborate B-O bond. However, a linear combination of a p and s orbital is a different matter. This situation corresponds to an asymmetric probability distribution of electronic charge that leans in the direction of the axis of the p orbital; and is labeled an "sp^3 hybrid". An appropriate example would be the Li-O bond. The indication of "3" in sp^3 indicates a three times more likely probability of finding the electron within the p state within the sp hybrid rather than that of an s state.

The tight binding approximation holds for a molecular crystal as well [2], however, the state equation must be amended as:

$$\psi(r) = \sum_R e^{ik \cdot R} \left(a\varphi(r - R) + b\varphi(r - d - R) \right). \qquad (10)$$

Here, d is the separation of the two basis atoms; a and b are the coefficients of the different basis atoms and φ is the Wannier function playing the role of the atomic wave function. Now the approximate molecular wave functions levels are tied to the tight binding approximation for the entire crystal. The qualitative discussion regarding the hybridization still holds, however.

Finally, this model generally works well, and will provide results that are close to the actual energy states, but this approach does not get the exchange and correlation parameters correct. Indeed, the adjustments needed to get the correct potential in the Hamiltonian almost ensure that the band gap cannot be estimated correctly using the tight binding approximation. With regard to the strongly correlated lithium tetraborate crystal

25

system, the reality is that strong hybridization occurs throughout the crystal with electrons affecting each other everywhere, due to the Coulombic repulsion. Hence, there is a compelling need for experimental data to provide the ground truth regarding band structure. Further, this same information can be used to verify any theoretical models looking at this system.

3.3. Photoemission Spectroscopy (PES)

Photoemission spectroscopy allows a system's orbital energies to be measured directly and must start with a discussion of the central phenomenon behind PES, the photoelectric effect. This effect was first identified in 1887 by Hertz [4] and later adequately explained by Einstein [5]. Photoemission is caused by the annihilation of an incident photon which excites an electron from a bound state to a continuum state. The bound state can be associated with an individual atom, molecule, or solid. In the interaction the photon provides sufficient energy to the electron to overcome the work function of the material and the binding energy. A diagram of the energy states with an arbitrary density of states is shown in Figure 3.1.
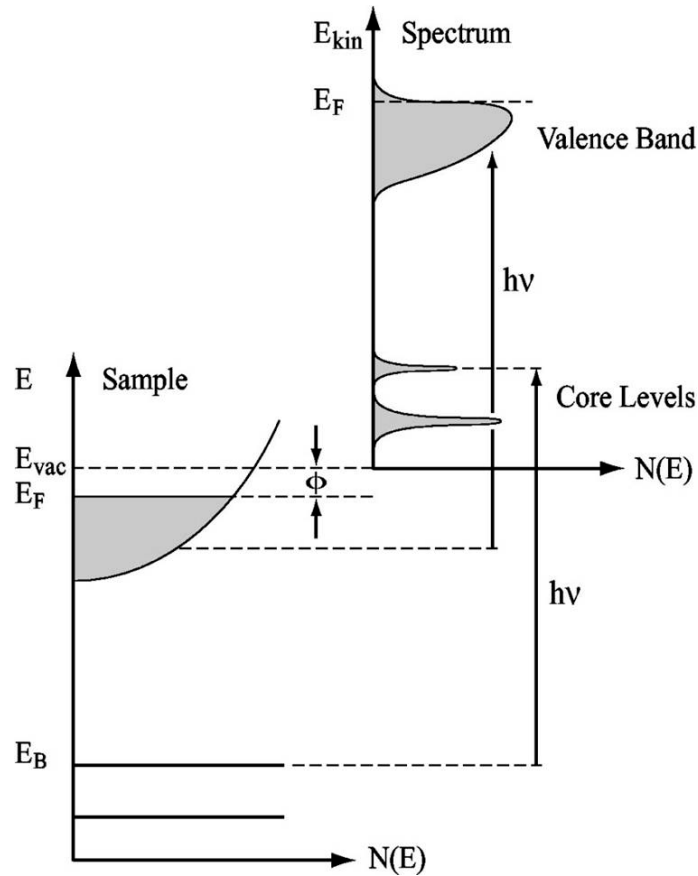
Figure 3.1. PES Energy Schematic. The electron energy distribution produced by incoming photons and measured as a function of the kinetic energy E_{kin} of the photoelectrons(right) is more conveniently expressed in terms of the binding energy E_B (left) when one refers to the density of states inside the solid ($E_B=0$ at E_F). Adapted from Hüfner [6].

The one- step versus the three- step model

The two generally currently accepted models of photoemission spectroscopy are presented. They are known as the "one-step model" and the "three-step model". The more rigorous of the two is the former. In the one-step model, photon absorption, electron removal and electron detection are all treated as a single coherent process. In this model the Hamiltonian describes all of the crystal bulk, surface, evanescent, and surface resonant states [7]. However, due to its complexity this model can be unwieldy

27

and unnecessary for the qualitative discussion of photoemission spectroscopy necessary here.

Another less rigorous model available to qualitatively address PES was developed by Berglund, Spicer and others into what is now commonly referred to as the "three-step model" [8-10]. This model is phenomenological by nature, but has proven to be successful [8-10]. For pedagogical purposes of qualitatively explaining how to obtain a photocurrent from photons impinging upon a surface, it is the better choice, and hence the model adopted in this research.

This model has limitations that are found in the underlying assumptions of the three-step model. The first assumption is that the photoemission event is sequential in nature. Next, it is assumed the energy distribution is the sum of the primary distribution of unscattered electrons, $N_{primary}(E, \hbar\omega)$, plus the distribution of background secondary electrons; with the former a convolution of three independent functions. These are the transmission function, T, escape function, D, and distribution of excited electrons, $N_{internal}$[11]:

$$N(E, \hbar\omega) = N_{primary}(E, \hbar\omega) + N_{sec}(E, \hbar\omega). \qquad (11)$$

The three step model is broken down into three independent steps accomplished in sequence: optical excitation of the electron in the solid; photoelectron transport to the surface; and photoelectron escape to vacuum. The first of the three steps follows.

Optical excitation of the electron in the solid

The model begins with a quantum mechanical treatment of a particle within a radiation field. In this case, the system is a photon incident upon an electron (within a solid). This yields the following time-dependent Hamiltonian [12]:

28

$$H' = \frac{1}{2m}(P - qA)^2 + V, \tag{12}$$

where *m, P, q, A and V* are the electron mass, electron momentum operator, charge, vector potential operator, and scalar potential, respectfully;

or, rewritten, the perturbing Hamiltonian is

$$H_o + H' = \frac{P \cdot P}{2m} - \frac{q}{2mc}\left(P \cdot A + A \cdot P - \frac{q}{mc}A \cdot A\right) + V. \tag{13}$$

At this point, the Hamiltonian is split into two parts,

$$H = H_0 + H', \tag{14}$$

where

$$H_0 = \frac{P \cdot P}{2m} + V; \tag{15}$$

and H' is the perturbing Hamiltonian. With the commutation relation,

$$[P, A] = P \cdot A - A \cdot P = -i\hbar\nabla \cdot A \tag{16}$$

where $\hbar$ is Dirac's Constant; the Hamiltonian becomes

$$H' = -\frac{q}{2mc}\left(2A \cdot P - i\hbar\nabla \cdot A - \frac{q}{mc}A \cdot A\right). \tag{17}$$

In order to simplify the equation, a gauge is chosen. This is allowed because the fields themselves are renormalizable [13] and the gauge of the universe, outside of vacuum fluctuations, is somewhat arbitrary. Here, the Coulomb gauge is chosen as;

$$\nabla \cdot A = 0. \tag{18}$$

In a physical sense this is equivalent to maintain a constant value for A relative to the atomic dimensions. This is a direct result of the dipole approximation, which will be discussed later. Although this is a common approximation, $\nabla \cdot A$ might become more

29

important at the surface, where electromagnetic fields may have a strong spatial dependence which leads to asymmetric line shapes for bulk direct-transition peaks [14].

Further, the $|A|^2$ terms can be ignored, which comes from two photon processes and are generally negligible with respect to the linear terms in conventional photoemission [7, 15]. This approximation remains valid as long as the flux of photons is relatively low [16].

Consequently, the perturbing Hamiltonian is now simplified to

$$H' = -\frac{q}{mc}(A \cdot P). \tag{19}$$

The radiation is assumed to be a plane wave, given that it is far from the source production. One can also assume a monochromatic and linearly polarized source since the synchrotron is producing the radiation. This leads to the following representation of A as a reasonable approximation of the vector potential [15, 17]:

$$A(x, t) = A_0 \hat{\varepsilon} \cos\left(\frac{\omega}{c}\hat{n} \cdot x - \omega t\right). \tag{20}$$

where A_0 is a complex constant, $\hat{\varepsilon}$ is the light polarization unit vector, $\hat{n}$ is the propagation direction, x is the contribution along this Cartesian coordinate direction at a specified time, t; and ω is the angular frequency of the monochromatic radiation.

Fermi determined a method of calculating the transition rate (probability of transition per unit time) due to a perturbation from one energy eigenstate of a quantum system into a continuum of energy eigenstates, using Dirac's time dependent perturbation theory [18]. The time-independent- transition probability per unit time is known as Fermi's "Golden Rule No. 2" [19, 20]:

$$R = \frac{2\pi}{\hbar} |\langle \varphi_f | H' | \varphi_i \rangle|^2 \delta(E_f - E_i - \varphi - h\upsilon) \qquad (21)$$

$$\propto |M(\mathbf{k_f}, \mathbf{k_i})_{fi}|^2 \delta(E_f - E_i - \varphi - h\upsilon)$$

where R is defined as the probability of transition of a bound atomic electron existing at a specified eigenstate (φ_i) to a continuum eigenstate (φ_f) via the time-dependent perturbation Hamiltonian operator (H'). The Kronecker delta function $\delta(E_f - E_i - \varphi - h\upsilon)$, expresses the requirement that the initial and final states of the system must have the same energy in order to have a non-zero probability of transition. The term $|M(\mathbf{k_f}, \mathbf{k_i})_{fi}|^2$ is the square of the transition matrix element. It should be pointed out that the development of Equation (21) presupposes that the function must vary slowly enough to enable the determination of time intervals which satisfy the stated condition, but remain small enough for the perturbation treatment of H' to be valid [12, 20].

The final assumption involves incorporating the electric dipole approximation [21]. Within the multipole expansion there exist an infinite number of terms. To use the dipole approximation of the full exponential expansion, only the leading term is kept. As long as the radiation wavelength is considerably greater than the dimensions of the atom, this approximation is valid. In the case of this particular research, the longest bond length of interest in lithium tetraborate is approximately ten Ångstroms [22]. To be able to use this approximation confidently, a minimum radiation wavelength of 200 Å needs to be maintained. This corresponds to photons of energy less than 500 eV. The highest energy photon to be used in this research corresponds to an energy of 190 eV, and easily meets this requirement.

Combining the above terms along with the assumptions already discussed, yields an internal energy distribution of photoexcited electrons, $N_{internal}$ [6]:

$$N_{internal} \propto \sum_{f,i} |M(\mathbf{k_f}, \mathbf{k_i})_{fi}|^2 \delta\big(E_f(\mathbf{k_f}) - E_i(\mathbf{k_i}) - hv\big) \; \delta\big(E \quad (22)$$

$$- E_f(\mathbf{k_f}) - \varphi\big)$$

where E is the final kinetic energy, hv is the photon energy, $E_f(\mathbf{k_f}), E_i(\mathbf{k_i})$ are the energies of the final and initial bands, respectively.

Transport of electron to surface

After being optically excited, the electron must travel to the surface and escape to be measured. The dominant loss mechanism that will impact an electron is the plasmon-electron interaction. The ability of the photoelectron to travel to the surface is dependent on its mean free path which is proportional to the probability that the photoelectron will not encounter a scattering event; and therefore retain its energy and momentum. To summarize Hüfner's presentation of the topic [6], the inelastic electron mean path, $\lambda_e(E, \mathbf{k})$, is

$$\lambda_e(E, \mathbf{k}) = \frac{\tau}{\hbar} \frac{dE}{d\mathbf{k}}. \qquad (23)$$

In Equation 23, $\frac{dE}{d\mathbf{k}}$ is the final state group velocity and the assumed isotropic scattering frequency, $\frac{1}{lifetime} = 1/\tau$, is dependent only upon the energy, E. According to Berglund and Spicer [8], the fraction of photoelectrons created within one mean free path of the surface is

$$T(E, \mathbf{k}) \cong \frac{\alpha\lambda_e}{(1 + \alpha\lambda_e)}; \qquad (24)$$

32

where α is the optical absorption coefficient of the light. Since lithium tetraborate is a wide band gap insulator, the mean free path can be expected to be very large. This should enhance the ability to map the bulk band structure since there is a greater chance the electron will escape from the surface to be captured by the analyzer.

Photoelectron escape to vacuum

Continuing Hüfner's model [6], the photoelectrons able to escape must have sufficient energy to overcome the surface potential barrier:

$$\frac{\hbar^2 {k_\perp}^2}{2m} \geq E_v - E_0; \tag{25}$$

where $k_\perp$ is the perpendicular, i.e. along the surface normal, component of the wave vector of the photoelectron, E_v is the energy of vacuum level and E_0 is the energy at the bottom of the valence band.

The parallel component of the transmission of the electron through the surface is conserved:

$$K_\parallel = k_\parallel + G_\parallel = \frac{\mathbf{P}_\parallel}{\hbar}; \tag{26}$$

where $K_\parallel$ is the wave vector component parallel to the surface for the photo-excited electron within the crystal, $k_\parallel$ is the parallel component of the wave vector of the electron initial state, $G_\parallel$ is the appropriate parallel component of the reciprocal lattice, and $\mathbf{P}_\parallel$ is the momentum of the photoelectron in vacuum.

Using Snell's law one can determine the minimum value of $K_\perp$ to just escape the crystal surface assuming a "perfect surface",

$$K_{\perp min} = \sqrt{2m(E_v - E_0)/\hbar^2}; \tag{27}$$

33

and the kinetic energy outside the crystal would be,

$$E_e = \frac{\hbar^2}{2m(K_\parallel{}^2 + (P_\perp{}^2/\hbar^2)^2)} = E_f(\mathbf{k}) - E_v. \tag{28}$$

Stepping away from the free electron model used thus far, and recalling that a wave function is actually a Bloch wave that contains plane wave contributions with various reciprocal lattice vectors, one can understand why a photoelectron can leave the crystal in more directions than one. The plane wave components, with the same values of $\mathbf{k}_\parallel + \mathbf{G}_\parallel$ for a particular final state of energy exit the crystal in the same direction and must be added coherently,

$$\frac{P_\perp{}^2}{2m} = E_f(\mathbf{k}) - E_v - \frac{\hbar^2(\mathbf{k}_\parallel + \mathbf{G}_\parallel)^2}{2m}. \tag{29}$$

Putting the pieces together, the expected angle-resolved photoelectron energy spectrum for a particular photon energy under the three-step model is [6]:

$$N(E, \mathbf{K}_\parallel, \hbar\omega) = N_{primary}(E, \mathbf{K}_\parallel, \hbar\omega) + N_{sec}(E, \mathbf{K}_\parallel, \hbar\omega) \propto \tag{30}$$

$$\sum_{f,i} \left| M(\mathbf{k}_f, \mathbf{k}_i)_{fi} \right|^2 T(E_f, \mathbf{k}_f) \left| D(E_f, \mathbf{K}_\parallel) \right|^2 \cdot \delta(E_f(\mathbf{k}_f) - E_i(\mathbf{k}_i) - h\nu) \cdot$$

$$\delta(E - E_f(\mathbf{k}_f) - \varphi) \cdot \delta(\mathbf{k}_i + G - K)\delta(\mathbf{K}_\parallel - \mathbf{P}_\parallel/\hbar) + N_{sec}(E, \mathbf{K}_\parallel, \hbar\omega)$$

The last expression in $N_{primary}$ — $\delta(\mathbf{K}_\parallel - \mathbf{P}_\parallel/\hbar)$ — ensures that the parallel (to the surface) component of momentum is conserved both inside and outside the crystal. A final word regarding both the escape and transmission functions. Both are smooth functions of energy; which will distort but not create any novel features to an energy distribution function [11, 15].

Equation (30) provides an approximation of the photoemission spectra by convolution of the initial state density of states with the final state density of states. It is worth noting that since the perturbing Hamiltonian matrix elements may be varied, a more sophisticated approach is often required. However, this derivation provides the basic concepts of a theoretical photocurrent. It identifies the joint density of states with the photoelectron energy distribution curves. This provides the basic concept of mapping electronic band structures of solids via photoemission spectroscopy. The same can be said with regards to inverse photoemission with one caveat that will be covered in a subsequent section.

3.4. Angle-Resolved Photoemission Spectroscopy (ARPES)

ARPES is one photoemission, spectroscopic technique that has taken advantage of Einstein's insight on the photoelectric effect and has matured into one of the most powerful methods for probing the electronic structure of materials [23]. In essence, ARPES incorporates the intensity and energy functional dependence of the collection angle with respect to some fixed axes. After a prediction by Mott that the technique could be used to experimentally map the occupied band structure, Smith, Traum and DiSalvo demonstrated success [24] in 1974. This technique has made it feasible to map the complete Fermi surface of well-ordered materials [25, 26]. Figure 3.2 depicts the basics of ARPES schematically.
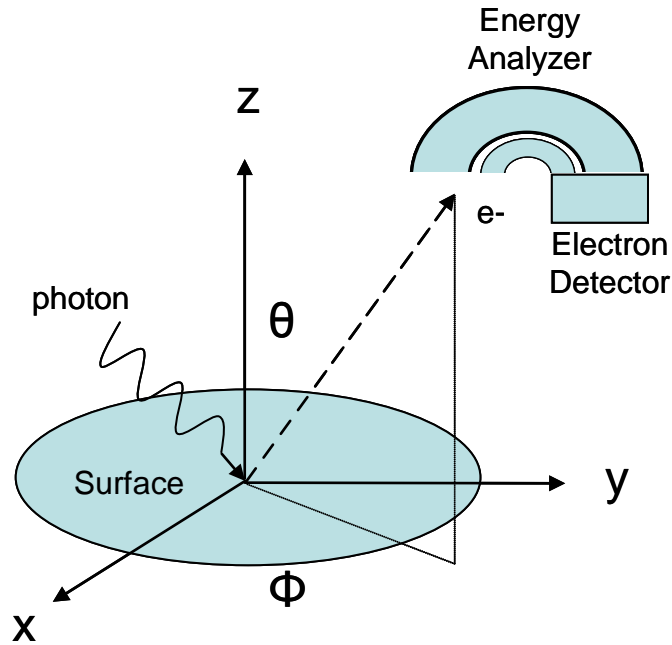
Figure 3.2. Schematic of angle resolved photoemission spectroscopy

ARPES is also one of the few experimental tools currently available that can measure the energy dispersion and symmetry of bulk bands. Unfortunately, it is not a simple process to obtain this data from three-dimensional energy bands using this technique. In addition to the factors previously discussed for photoemission in general, one now has to contend with the angular dependence of a two-dimensional spectrum recorded by the detector of a three-dimensional sample [27].

To successfully apply this technique, it is presumed that a beam of monochromatized radiation is targeting a properly aligned, well ordered crystal. The smaller the spot (illumination) size, the better the effective $k_\parallel$ vector resolution. The emitted photoelectrons with kinetic energy, E_e, will then be collected by an electron

energy analyzer characterized by a finite acceptance angle and pass energy. One can then simply determine the modulus of the photoelectron momentum, $|\boldsymbol{P}|$:

$$|\boldsymbol{P}| = \sqrt{2mE_e}. \tag{31}$$

Momentum is conserved, with the electron's momentum component parallel to the surface within the crystal plus that of the crystal momentum equal to that of the photoemitted electron's parallel momentum component. However, the surface discontinuity does not allow the perpendicular momentum component with respect to the surface to be determined experimentally without further constraints. At the surface the electron experiences a potential energy step that decreases the component of the kinetic energy perpendicular to the surface as the electron emerges from the solid. Also, the dispersion of the electron inside the crystal is not free electron-like because of the periodic array of ion cores. Further clarification is needed to obtain useful equations that incorporate these necessary constraints.

To obtain working equations for this particular photoemission technique, one is referred to Plummer and Eberhardt's development for three-dimensional systems [27]. The authors start with the kinetic energy, E_e, of an emitted photoelectron:

$$E_e = \frac{\hbar^2}{2m}\left(\left|\boldsymbol{k}_{\parallel}\right|^2 + |\boldsymbol{k}_{\perp}|^2\right), \tag{32}$$

where $\hbar\boldsymbol{k}_{\parallel}$ and $\hbar\boldsymbol{k}_{\perp}$ are the components of momentum in the vacuum, parallel and perpendicular to the surface. Following a process similar to Hüfner, as discussed earlier, they arrive at the two main equations useful to researchers interested in this technique [6, 27]:

$$|\boldsymbol{k}_{\parallel}| = \sqrt{\frac{2m}{\hbar^2} E_e} \sin\theta. \tag{33}$$

and,

$$|\boldsymbol{k}_{\perp}| = \sqrt{\frac{2m}{\hbar^2}(E_e \cos^2\theta + U_0)}. \tag{34}$$

where θ is the collection angle depicted in Figure 3.3; and U_0 represents the inner potential and is the sum of the work function and the Fermi energy.

Using Eberhardt and Plummer's example with Ni whose bulk and surface Brillouin zones along high points of symmetry are depicted in Figure 3.3 one can see the utility of Equations (33) and (34) in mapping bands [28]. Through this final state technique, one is able to make reasonable assertions regarding overall, parallel and perpendicular components of the electrons' energy and momentum states as they exist within the crystal.
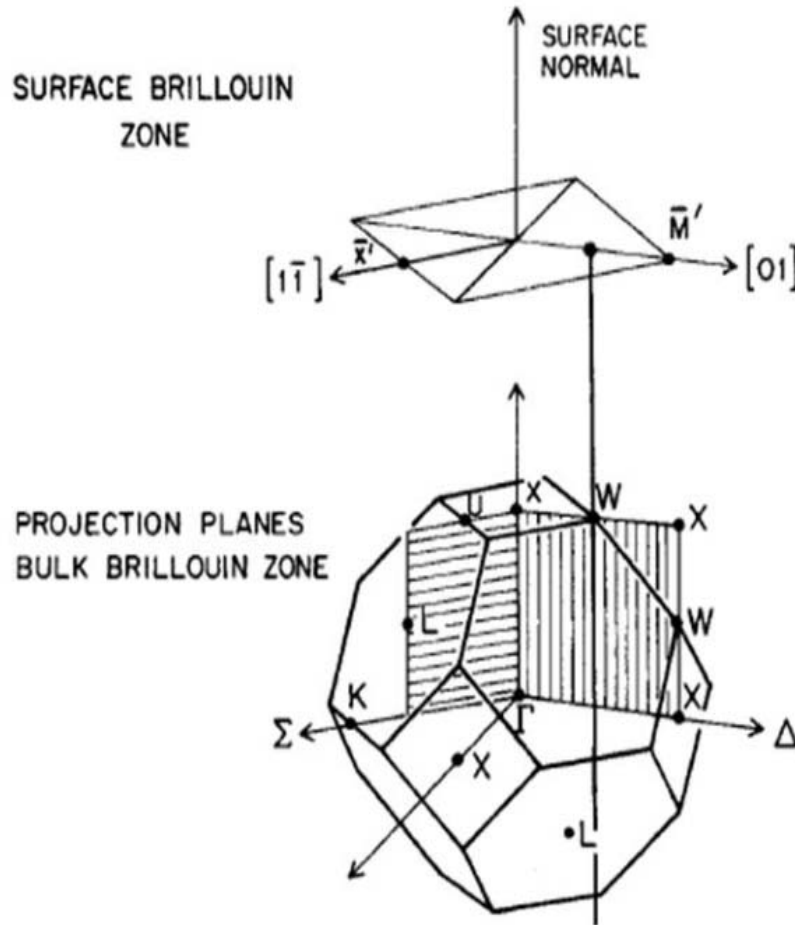
Figure 3.3. Face centered cubic depiction of surface Brillouin zone (top) and bulk Brillouin zone (bottom) for Ni. Note the solid line representing a rod connecting all points in bulk zone with one point in surface zone with the same value of $k_\parallel$. Adapted from Plummer and Eberhardt [27], Ashcroft and Mermin [2] and Hüfner [6].

Given the system as depicted in Figure 3.3, one also sees the Surface Brillouin

Zone (SBZ) and how it can be projected from the bulk BZ. Figure 3.4, depicts yet

another aspect of this powerful technique. This time contours of a constant energy inside

the crystal for $k_\parallel$ in (110) and (100) mirror planes are presented.

www.manaraa.com
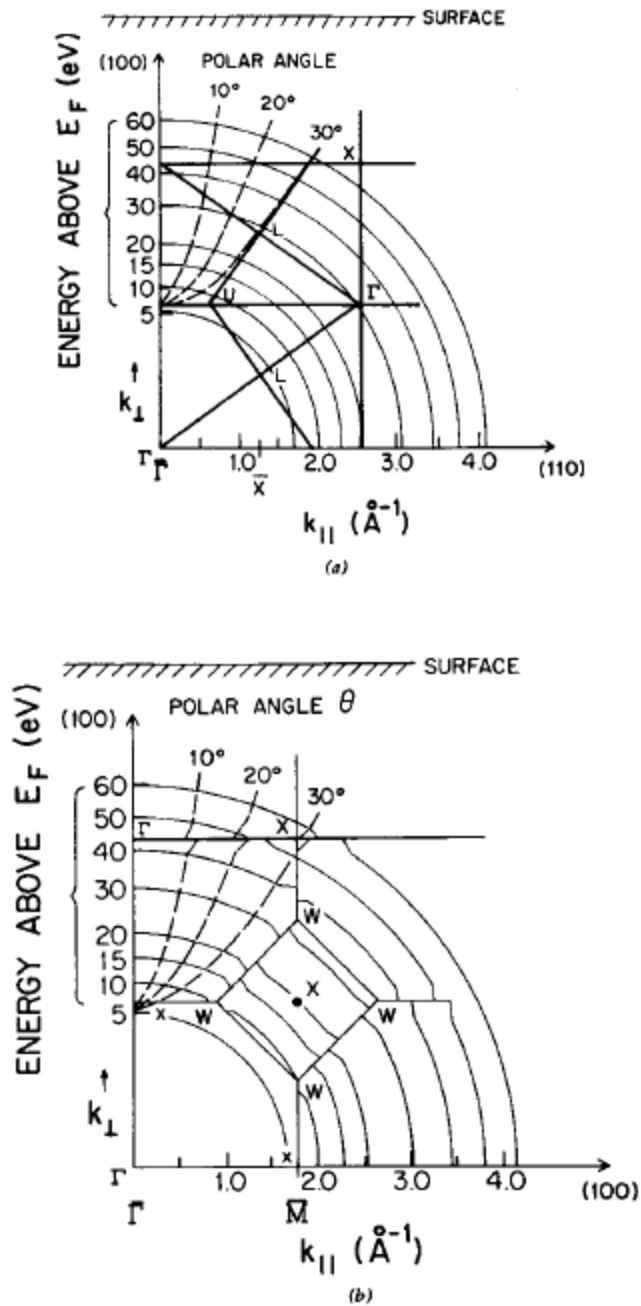
Figure 3.4: Cuts through the extended Brillouin zone of a face-centered cubic crystal (Ni). Vertical axis is $k_\perp$ relative to a (100) surface. The horizontal axis is $k_\parallel$, the momentum parallel to the surface. Courtesy of Plummer and Eberhardt [27].

Another way of stating this is:

40

$$k^2 = \left|k_\parallel\right|^2 + |k_\perp|^2 = \frac{2m}{\hbar^2}(E_e + U_0 - q\phi). \tag{35}$$

Consequently, one can obtain the direct position transitions—the dashed lines depicted in Figure 3.4—as a function of energy for a fixed collector angle if $\left|k_\parallel\right|, |k_\perp|, U_0$ and ϕ are known. This technique has been proven, and is in reasonable agreement with theory. The drop in intensity within the gap, which accounts for the gaps at zone boundaries, is graphically represented by a discontinuity along the dashed line in Figure 3.4.

Plummer and Eberhardt also present a more accurate method to obtain the initial and final state band structure at high symmetry points independent of the free-electron final state model [27]. If the researcher were to fix the detector along a known direction of the Surface Brillouin Zone (SBZ), the $k_\perp$ range of values depicted in Figure 3.3 will be a repeating scheme of symmetry points in k space since one is observing photoemission of a periodic lattice. The authors provide an example of this as shown in Figure 3.4 by fixing the detector at a value $k_\parallel = \bar{M}$ in the [01] direction of the (01) SBZ. The result of this is $k_\perp$ periodic repeating of X and W. Collected data is then converted to E versus $k_\perp$. This works qualitatively if the researcher assumes a free-electron band structure.

These types of techniques were used to map the band structure of lithium tetraborate as described in what follows in this dissertation. To explore the surface band structure, ARPES was used to obtain the different values of the parallel wave vector component, $k_\parallel$; while energy dependent photoemission was used to vary E_e in an effort to find the perpendicular wave vector components, $k_\perp$.

41

3.5. Inverse Photoemission Spectroscopy

X-ray absorption spectroscopy (XAS) and its variants and inverse photoemission spectroscopy (IPES) are the two major empty-state spectroscopic techniques available to the experimentalist [29]. Both approaches examine the unoccupied states above the Fermi level; albeit with subtle differences. Angle-resolved IPES was the technique of choice of this research, because of the need to obtain the wave vector dependence, and thus more valuable than other empty state techniques like Bremsstrahlung Isochromat Spectroscopy or X-ray Absorption Spectroscopy. By obtaining wave vector dependence, the dispersion relation can be ascertained; which would also provide insight to effective masses for charge carriers in the conduction band. Further, one would be able to experimentally verify the character of theoretical BZs .

IPES utilizes a focused beam of electrons of a known energy, E_{kin}, incident on a sample. Upon entering the crystal, the excited incident electrons will decay radiatively or non-radiatively to states at a lower energy. The radiative decay can be detected. Further, if the incident electron energy, E_{kin} is ranged while keeping the detected photon energy constant, the measured photon counting rate will resemble the unoccupied density of states. Of particular interest to the researcher for this empty-state spectroscopy is the k-resolved capability, also known as k-resolved inverse photoemission spectroscopy (KRIPES). Because only electrons at a specified energy are involved, it is possible to specify the momentum—or k vector—of the incident electron [30]. Figure 3.5 depicts an overall schematic of IPES.

42
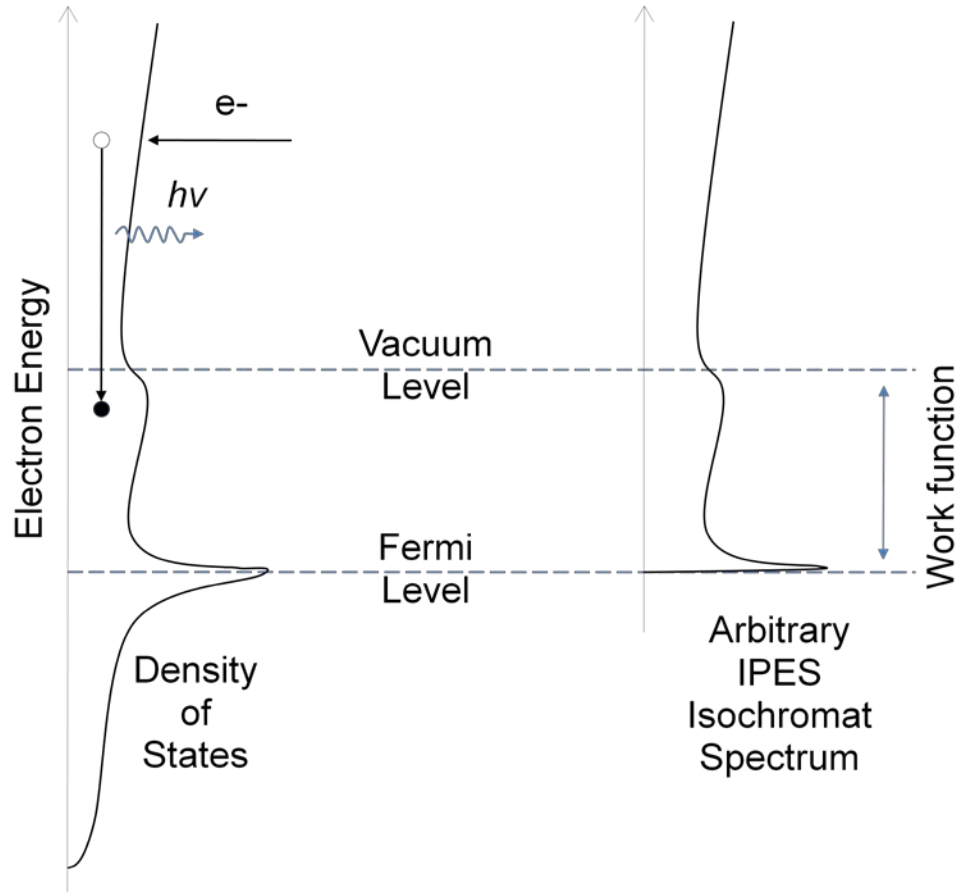
Figure 3.5. Phenomenology of UV IPES (Isochromat mode)

IPES is based on the same conservation of energy and momentum principles already discussed for ARPES. It has a proven track record of being able to experimentally map the unoccupied bands. Examples of wave vector- dependent band structure research using IPES include: CO layers on Ni(110), In layers on Si(111), Cu(100), unoccupied electronic states of Ni, and strained Gd (0001), as well as more complex systems such as $La_{0.65}Sr_{0.35}MnO_3$ (100) and crystalline polymers [29].

This technique is complementary to ARPES and allows mapping of the empty states from the Fermi level up through the vacuum level in lithium tetraborate. It is

43

noteworthy, however, to point out one important difference that impacted this research effort— the cross sectional magnitude from a standard IPES architecture is only 10^{-3} to 10^{-5} (X-ray to UV energies, respectively) of that from a standard PES experimental set-up [29]. This leads to greater data acquisition times to acquire data of much less energy resolution.

To understand the cause of such a small cross sectional magnitudes compared to that of IPES using this technique one is referred to Johnson and Davenport's consideration of the subject [31], which follows in summary.

The authors start with the same interaction Hamiltonian as discussed in the PES section (after throwing out second-order processes, the $|A|^2$ terms, and choosing a gauge such that the scalar potential is zero):

$$H' = \frac{q}{2mc}(A \cdot P + P \cdot A) \tag{36}$$

The key difference [31], is that unlike PES, where A could be treated classically, the vector potential must be quantized and replaced by the more correct field operator, or we would obtain a result that is clearly not physical [32]. Therefore,

$$A(x, t) = V_p^{-.5} \sum_q \sum_\alpha \frac{2\pi c\hbar}{\omega} (a_{q,\alpha}(t)\hat{\epsilon}^\alpha e^{iq \cdot x} \tag{37}$$

$$+ a_{q,\alpha}^\dagger(t)\hat{\epsilon}^\alpha e^{-iq \cdot x}).$$

Here $\hat{\epsilon}^\alpha$ is the linear polarization vector that depends on the photon propagation direction, q, $a_{q,\alpha}$ and $a_{q,\alpha}^\dagger$ are the destruction and creation operators, respectively, that operate upon a photon in the state q, α.

44

The authors obtain the transition rate using first-order perturbation theory and divide it by the incident electron flux. An assumption is made that the continuum electron state is normalized to obtain a working IPES cross section [31]:

$$\frac{d\sigma}{d\Omega_{IPES}} = \frac{\alpha}{2\pi}\frac{\omega}{mc^2}\frac{1}{\hbar k}|\langle b|\hat{\epsilon}\cdot \boldsymbol{k}|\boldsymbol{k}\rangle|^2; \tag{38}$$

where $d\Omega$ is the solid angle of emission, α —in this case— is the fine structure constant; $\langle b|$ denotes the bra of an electron in a bound state plus photon with wave vector, $\boldsymbol{q}$; and $|\boldsymbol{k}\rangle$ is the ket of the electron with no photons in a continuum state. Using similar assumptions, one can estimate the PES cross section:

$$\frac{d\sigma}{d\Omega_{PES}} = \frac{\alpha}{2\pi}\frac{k}{m}\frac{1}{\hbar\omega}|\langle \boldsymbol{k}|\hat{\epsilon}\cdot \boldsymbol{k}|b\rangle|^2; \tag{39}$$

which are compared via the following ratio:

$$R = \frac{d\sigma}{d\Omega_{IPES}}\bigg/\frac{d\sigma}{d\Omega_{PES}} = \frac{\omega^2}{c^2 k^2} = \frac{q^2}{k^2} = \left(\frac{\lambda_{electron}}{\lambda_{photon}}\right)^2. \tag{40}$$

Therefore, one can see that at energies characteristic of the UV range, for instance 10 eV, the inverse photoemission cross section is smaller by $\approx 10^{-5}$ from the photoemission cross section. However at higher energies the IPES cross sections can differ by only $\approx 10^{-3}$ from the PES cross section. Hence the anticipated IPES signal is considerably lower than that of an equivalent PES signal.

Despite the inherently low IPES signal, this technique has been successfully used throughout this research; the details of the experimental set-up will be provided in Chapter 4.

3.6. Light Polarization Dependent Photoemission

In order to resolve states when a mix of bands exists, one useful tool available to the researcher is light polarization dependent photoemission spectroscopy. The potential to use such a tool for mix symmetry situations during lithium tetraborate electron configuration mapping was certainly apparent. The basic theory behind this technique is depicted in Figure 3.6.
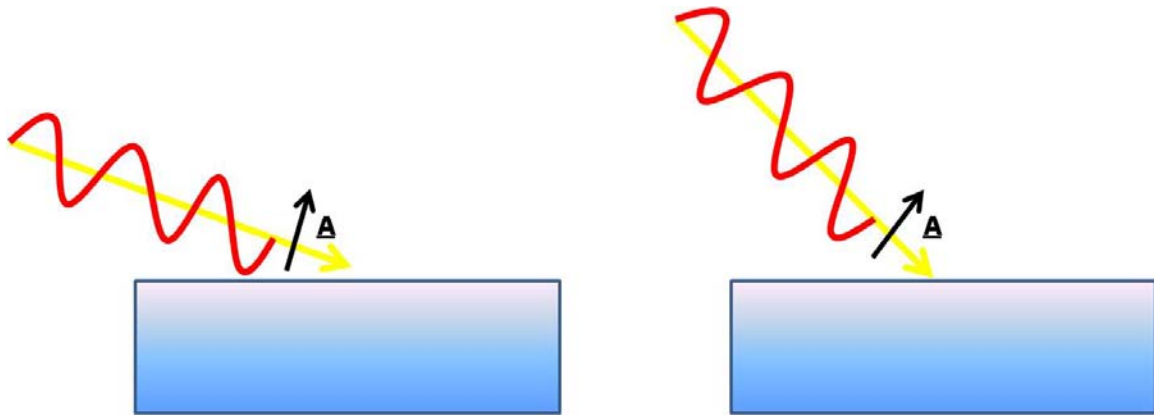
Figure 3.6. (a) Schematic of P-light depicts incident light at 70° with respect to sample normal compared to (b) S+P light, where light is 45° with respect to sample normal. $\underline{\textbf{A}}$ denotes the direction of the vector potential.

With the experimental capability of knowing exactly where $\underline{\textbf{A}}$ is aligned with regards to the incident photons via the synchrotron produced plane polarized light source, one can take advantage of simply changing angles of the sample to change polarization and to understand the nature of the orbitals present within the sample. Before providing a meaningful example of this technique it would be worthwhile to summarize a few salient points with regards to selection rules and symmetry in general.

Symmetry based selection rules

Provided that one has a well ordered sample, symmetry and selection rules are available to assist in further resolving the electron configuration. In order to use the symmetry selection rules effectively, one must know the group representation of each orbital, the orientation of the light vector potential, and the reflection angles (for PES) or the incidence angles (for IPES) of the electrons.

By reducing $\langle \varphi_f | A \cdot P | \varphi_i \rangle$ via the electric dipole approximation to a simple vector operator as was discussed earlier, the spherically-based selection rules [15] discussed by Bernath for a multi-electron atom of J, M_L, L, S basis [33] are available:

$$\Delta J = \pm 1,0, but\ J' = 0 \nleftrightarrow J'' = 0;\ \Delta M_L = \pm 1,0; \qquad (41)$$

$$\Delta L = \pm 1,0;\ \Delta S = 0.$$

These selection rules apply, but are not the only selection rules that apply to photoemission from a crystalline solid. Symmetry is now also a conserved quantum number as is $\boldsymbol{k}_\parallel$.

For example, when using light polarization dependent PES an enhancement of a spectral feature because the orientation of the electric field component is more along the surface than its predecessor, with all other variables remaining the same, could indicate the nature of the hybridized valence state. As a specific example (to be discussed in detail in Chapters 6-8) one could conclude that a particular valence band state had considerable O p_x or p_y contribution as opposed to O p_z.

An equivalent perspective using group theory

Another perspective on this system is gained by considering that for a crystal Hamiltonian, H, there exist symmetry operators, S, that leave H invariant. Since S commutes with H, and $S\psi$ is an eigenfunction of H [15],

$$H(S\psi) = E(S\psi). \tag{42}$$

Now, since these form a group irreducible representation, group theory provides a ready mechanism for the researcher to explore what are allowed and forbidden transitions. In his extensive book on the topic of group theory, D. Bishop points out that the initial state, perturbing Hamiltonian and final state must all share the same symmetry, or the overlap integral for the given wavefunction will be zero [34]. In other words, to see a physically allowed transition displayed as a peak in a spectrum, one must have a nonzero value for that particular matrix element. Consequently, if one knows the symmetry of lithium tetraborate for the particular crystal direction, one is able to tie spectral results to certain locations and rule out others.

An example using lithium tetraborate

It is worthwhile to illustrate this via an example using lithium tetraborate. A particular character table of use for this research is displayed in Table 3.1. (For a complete list of character tables used for this research along with a thorough discussion of their use, Bishop, along with many others, reviews and summarizes the details [35].) To summarize Bishop's salient points, pertinent to this research, character tables are in essence the non-equivalent irreducible representations of a point group. A character is actually the trace, the sum of diagonal elements of an operator as represented by a matrix, which is a part of a representation of any point group [36]. This is convenient because

48

with the knowledge of the trace for a class of symmetry operations, we do not have to explicitly state every matrix that exists. For this research, character tables were used as a tool to assist in determining allowed or not allowed transitions. A PES example that utilized Table 3.1 (below) follows to illustrate their utility.

Table 3.2. Group representation elements, associated basis functions and character table of the C_{2v} point group [29, 35]

C_{2v}	E	C_2	$\sigma_v(xz)$	$\sigma_v(yz)$	*Irreducible representations basis functions*
A_1	1	1	1	1	$z; x^2, y^2, z^2; z^3; z(x^2-y^2)$
A_2	1	1	-1	-1	$R_z; xy; xyz$
B_1	1	-1	1	-1	$x, R_y; xz; xz^2, x(x^2-3y^2)$
B_2	1	-1	-1	1	$y; R_x; ; yz^2, y(3x^2-y^2)$

Realizing that the surface (in momentum space) of the tetragonal lithium tetraborate will resemble that of either Figure 3.7a or b for the $Li_2B_4O_7(110)$ and (100) and that one has hybridization of s and p type atomic orbitals to choose from for the molecular orbitals; one can start to draw conclusions about the nature of the molecular bonds present by using the polarization dependent technique discussed earlier.

49
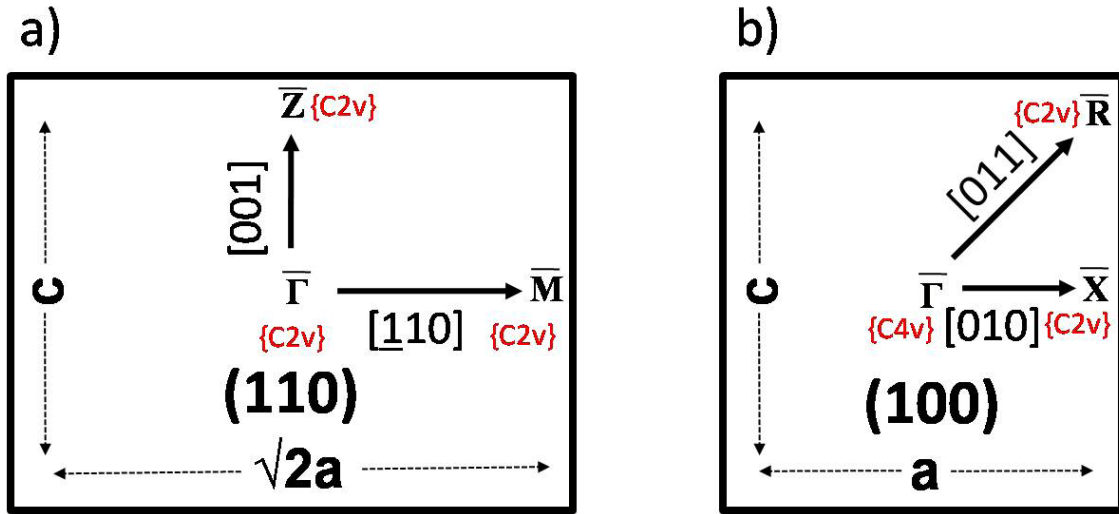
Figure 3.7. (a) Surface Brillouin Zones (SBZ) for $Li_2B_4O_7$(110) and (b) (100) crystal surface, depicting the point group symmetry {} at locations within SBZ.

For instance, if **E** was aligned along $\overline{\Gamma} - \overline{M}$, where C_{2v} symmetry is prevalent, and we saw an enhancement going from p to s+p light, we can use Table 1, row 4 to say that the orbitals present depict a p_y character. (One doesn't really know which orientation as of yet, a more accurate statement would be that this orbital possessed $p_y\pm$ p_x character.) If one measured an enhancement to p polarization-like spectra, one would look to the first row in Table 3.1 and state that this orbital possesses an s or p_z like nature. The usefulness of symmetry selection rules is realizing $\boldsymbol{A} \cdot \boldsymbol{P}$ really has limited, non-zero choices; which we take advantage of by using this technique.

Symmetry is useful, albeit with consideration of its limitations. As one moves away from a high symmetry point or direction, symmetry and selection rules play a more limited role. As the photon energy is increased, the wave vector also increases, leading to more orbital hybridization as discussed previously and a reduction in symmetry [29].

50

3.7. Theoretical Models

A theoretical model that closely resembles experiment is very useful in analysis. The theoretical modeling of lithium tetraborate band structure is certainly not an exception. To date, several attempts have been made, with Islam et al. being one of the most recent published occurrence [37]. However, each of these models has shortcomings which will be briefly addressed.

Local Density Approximation model

Many theoretical solid state models are based upon Density Functional Theory (DFT). In order to obtain a reasonable approximation of the theoretical ground state properties of a solid, DFT utilizing the Local Density Approximation (LDA) was used to analyze the ground state properties of lithium tetraborate [37]. However, the calculated band gap remains suspect since LDA does not accurately model strongly correlated systems such as lithium tetraborate. However, there are aspects of the modeling that are useful for validating the experimental results of this research.

Kohn and Sham first developed the LDA to approximate the exchange correlation energy functional in DFT [38]. LDA accomplishes this by using homogenous electron gas exchange correlation energy for an electron of a similar density to that of the inhomogeneous system of interest. This is based on Hohenberg and Kohn's work concerning the ground state of an electron in an external potential [39]. In this latter effort, the authors were able to prove that there exists a universal density functional independent of an external potential, such that the correct ground-state energy associated with the external potential can be determined.

51

The mechanics of the procedure incorporates the LDA portion within a linear muffin-tin orbital method [40, 41] in the atomic sphere approximation. The Brillouin-zone integrations are performed using the tetrahedron method [42] on a regular mesh in the Brillouin zone of the tetragonal lattice.

However, DFT does not reproduce the electronic structure correctly. DFT incorrectly counts electrons which ultimately leads to inaccurately modeling the lithium tetraborate molecular system's electronic structure as determined experimentally via ARPES or IPES. DFT also does not adequately account for final state effects, configuration interactions, matrix element (symmetry selection rule) effects and temperature effects. More importantly for this research effort, by their very nature, DFT methods tend to underestimate the value for exchange energy, which is the kernel of exchange-correlation potential in DFT/LDA, leading to incorrectly calculating the band gap [43]. Because of these, this model always underestimates the band gap. In some cases the underestimate is as large as forty percent from experimental results [43]. Consequently, one can only obtain a qualitative understanding of the lithium tetraborate band structure using the LDA model, as compared to the experimental results this research will obtain.

LDA + U Model

An improvement to the LDA was proposed by Anisimov et al. with their development of the LDA+U model [44, 45]. This model incorporated an unrestricted Hartree-Fock treatment of an electron configuration with a screened Coulomb energy (U) and an exchange energy (J). The LDA+U model results in the energy functional becoming both orbital and density dependent. This model has the potential of providing

52

results closer to experiment. However, it would be difficult to obtain a reasonable estimate of U; especially when U is often chosen on the basis of a fit to experimental results, which until this research did not exist.

GW Model

GW is the approximation suggested and developed by Hedin [46]. It provides an estimate of the self-energy operator by using the electronic system Green's function, G, within the screened Coulomb field, W.   Incidentally, the GW derived band structure of Si has compared very well with experimental results [47].   However, because of its complexity, it can be computer intensive. Arguably, GW should give one the closest estimate to experiment; however, without experimental results, it is difficult to obtain a solution that will converge to the correct solution, as defined by that derived from experiment.

3.8. References

1. W. Harrison, "Energy Bands," in *Electronic Structure and the Properties of Solids: The Physics of the Chemical Bond,* (Dover Publications, Inc., 1989), pp. 32.

2. N. W. Ashcroft and N. D. Mermin, *Solid State Physics* (Thomas Learning, 1976).

3. W. Harrison, "Bond Orbitals," in *Electronic Structure and the Properties of Solids: The Physics of the Chemical Bond,* (Dover Publications, Inc., 1989), pp. 64.

4. H. Hertz, "(Translation) Influence of ultraviolet light on the electric discharge," Annalen der Physik **33,** 983 (1887).
5. A. B. Arons and M. B. Peppard, "Einstein's Proposal of the Photon Concept---a Translation of the Annalen der Physik Paper of 1905," American Journal of Physics **33,** 367-374 (1965).

6. S. Hüfner, "Introduction and Basic Principles," in *Photoelectron Spectroscopy Principles and Applications,* (Springer-Verlag, 1995), pp. 4.

7. A. Damascelli, Z. Hussain, and Z. Shen, "Angle-resolved photoemission studies of the cuprate superconductors," Rev. Mod. Phys. **75,** 473-541 (2003).

8. C. N. Berglund and W. E. Spicer, "Photoemission Studies of Copper and Silver: Theory," Physics Review **136,** 1030 (1964).

9. H. Y. Fan, "Theory of Photoelectric Emission from Metals," Phys. Rev. **68,** 43-52 (1945).

10. P. J. Feibelman and D. E. Eastman, "Photoemission spectroscopy--Correspondence between quantum theory and experimental phenomenology," Phys. Rev. B **10,** 4932-4947 (1974).

11. M. Cardona and L. Ley, *Photoemission in Solids* (Springer-Verlag, 1978).

12. C. Cohen-Tannoudji, B. Diu, and F. Laloe, "Quantum Mechanics," (John Wiley & Sons, 1977), pp. 224.

13. J. Jackson, "Gauge Transformation, Lorenz Gauge, Coulomb Gauge," in *Classical Electrodynamics,* (John Wiley & Sons, Inc., 1999), pp. 240.

14. E. D. Hansen, T. Miller, and T. C. Chiang, "Surface photoemission in Ag(100)," Phys. Rev. B **55,** 1871-1875 (1997).

15. D. LaGraffe, "Electronic and Magnetic Properties of Rare Earth Ferromagnets in Constrained Systems: An Experimental Case Study of Gadolinium and Terbium Ultrathin Films," (1990).

16. W. Schattke, M. A. Van Hove, Garcia de Abajo, F. J., R. D. Muino, and N. Mannella, "Overview of Core and Valence Photoemission," in *Solid-State Photoemission and Related Methods Theory and Experiment,* W. Schattke and M. Van Hove, eds. (Wiley-VCH Verlag GmbH & Co.KGaA, 2003).

17. R. Fitzpatrick, "Lecture Notes: Quantum Mechanics," University of Texas (2006).

18. P. Dirac, "The Quantum Theory of the Emission and Absorption of Radiation," Proceedings of the Royal Society of London. Series A, Containing Papers of a Mathematical and Physical Character **114,** 243 (1927).

19. E. Fermi, "Nuclear Reactions," in *Nuclear Physics Course Notes Compiled by Ray Orear, A. H. Rosenfeld, and R. A. Schluter,* (University of Chicago Press, 1950), pp. 141.

20. R. Liboff, "Harmonic Perturbation," in *Introductory Quantum Mechanics,* (Addison Wesley, 2003), pp. 712.

21. J. Jackson, "Electric Dipole Fields and Radiation," in *Classical Electrodynamics,* (John Wiley & Sons, Inc., 1999), pp. 410.

22. Y. V. Burak, B. V. Padlyak, and V. M. Shevel, "Neutron-Induced Defects in the Lithium Tetraborate Single Crystals," Radiation Effects & Defects in Solids **157,** 1101-1109 (2002).

23. K. Robnagel, L. Kipp, and M. Skibowski, "Angle-resolved photoelectron spectroscopy: From photoemission imaging to spatial resolution," in *Solid-State Photoemission and Related Methods Theory and Experiment,* W. Schattke and M. Van Hove, eds. (Wiley-VCH Verlag GmbH & Co.KGaA, 2003).

24. N. V. Smith, M. M. Traum, and F. J. Di Salvo, "Mapping energy bands in layer compounds from the angular dependence of ultraviolet photoemission," Solid State Communications, **15,** 211-214 (1974).

25. P. Aebi, J. Osterwalder, P. Schwaller, L. Schlapbach, M. Shimoda, T. Mochiku, and K. Kadowaki, "Complete Fermi Surface Mapping of $Bi_2Sr_2Cu_2O_{8+x}$ (001): Coexistence of Short Range Antiferromagnetic Correlations and Metallicity in the Same Phase," Physical Review Letters **72,** 2757 (1994).

26. A. Santoni, L. J. Terminello, F. J. Himpsel, and T. Takahashi, "Mapping the Fermi-surface of graphite with a display-type photoelectron spectrometer," Applied Physics A-Materials Science & Processing **52,** 299-301 (1991).

27. E. W. Plummer and W. Eberhardt, "Angle-Resolved Photoemission as a Tool for the Study of Surfaces," in *Advances in Chemical Physics,* I. Prigogine and S. A. Rice, eds. (John Wiley & Sons, Inc., 1982), pp. 533-656.

28. W. Eberhardt and E. Plummer, "Angle-resolved photoemission determination of the band structure and multielectron excitaitons in Ni," Phys. Rev. B **21,** 3245 (1980).

29. C. N. Borca, T. Komesu, and P. A. Dowben, "Comparing inverse photoemission and X-ray absorption spectroscopies," Journal of Electron Spectroscopy and Related Phenomena, **122,** 259-273 (2002).

30. N. V. Smith, "Inverse Photoemission," Rept. Prog. Phys. **51,** 1227-1294 (1988).

31. P. D. Johnson and J. W. Davenport, "Calculated inverse photoemission cross sections from adsorbed molecules," American Physical Society **31,** 7521 (1985).

32. J. Sakurai, *Advanced Quantum Mechanics* (Addison-Wesley, 1967).

33. P. F. Bernath, "Selection Rules," in *Spectra of Atoms and Molecules,* (Oxford University Press, 2005), pp. 134.

34. D. M. Bishop, "Vanishing Integrals," in *Group Theory and Chemistry,* (Dover Publications, 1993), pp. 158.

35. D. M. Bishop, "Character Tables," in *Group Theory and Chemistry,* (Dover Publications, 1993), pp. 279.

36. D. M. Bishop, "Irreducible representations and character tables," in *Group Theory and Chemistry,* (Dover Publications, 1993), pp. 117.

37. M. M. Islam, V. V. Maslyuk, T. Bredow, and C. Minot, "Structural and Electronic Properties of $Li_2B_4O_7$," J. Phys. Chem. B **109,** 13597-13604 (2005).

38. W. Kohn and L. J. Sham, "Self-Consistent Equations Including Exchange and Correlation Effects," Phys. Rev. **140,** A1133-A1138 (1965).

39. P. Hohenberg and W. Kohn, "Inhomogeneous Electron Gas," Phys. Rev. **136,** B864-B871 (1964).

40. M. Methfessel, "Elastic constants and phonon frequencies of Si calculated by a fast full-potential linear-muffin-tin-orbital method," Phys. Rev. B **38,** 1537 (1988).

41. T. Komesu, H. Jeong, J. Choi, C. Borca, P. Dowben, A. Petukhov, and B. Schultz, "Electronic structure of ErAs(100)," Phys. Rev. B **67,** 035104 (2003).

42. O. Jepson and O. K. Anderson, "The electronic structure of h.c.p. Ytterbium," Solid State Communications **9,** 1763-1767 (1971).

43. I. N. Yakovkin and P. A. Dowben, "The Problem of the Band Gap in LDA Calculations," Surface Review and Letters **14,** 481 (2007).

44. V. I. Anisimov, J. Zaanen, and O. K. Andersen, "Band theory and Mott insulators: Hubbard U instead of Stoner I," Phys. Rev. B **44,** 943-954 (1991).

45. V. I. Anisimov, I. V. Solovyev, M. A. Korotin, M. T. Czyzyk, and G. A. Sawatzky, "Denistiy-Functional Theory and NiO Photoemission Spectra," Phys. Rev. B **48,** 16929 (1993).

46. L. Hedin, "New Method for Calculating the One-Particle Green's Function with Application to the Electron-Gas Problem," Phys. Rev. **139,** A796-A823 (1965).

47. W. Ku and A. G. Eguiluz, "Band-Gap Problem in Semiconductors Revisited: Effects of Core States and Many-Body Self-Consistency," Phys. Rev. Lett. **89,** 126401 (2002).

4. Experiment

4.1. Overview

This chapter will provide details regarding the equipment and procedures used during this research. Sections pertaining to sample preparation and pre-characterization, photoemission spectroscopy (PES) and inverse photoemission spectroscopy (IPES) will follow sequentially.

4.2. $Li_2B_4O_7$ Sample Preparation, Repeatability and Pre-characterization

$Li_2B_4O_7$ crystal growth

$Li_2B_4O_7$ material prepared at the Department of Electronics, L'viv University, Ukraine using the standard Czochralski crystal growth method [1, 2] were the samples used for this research. $Li_2B_4O_7$ single crystal samples of either (100) or (110) orientation were prepared and mechanically cut along one of these two crystal directions.

To ensure results repeatability, two different samples for both orientations were used for this experiment. Additionally, over a period of three months each of the samples was exposed to multiple iterations of pumping from atmospheric to ultra high vacuum, temperature differences from 273 K to 723 K, sample mounting, and surface cleaning.

Figure 4.1 depicts the two different cuts of crystal present using a Cartesian-like three dimensional reference frame in real space.
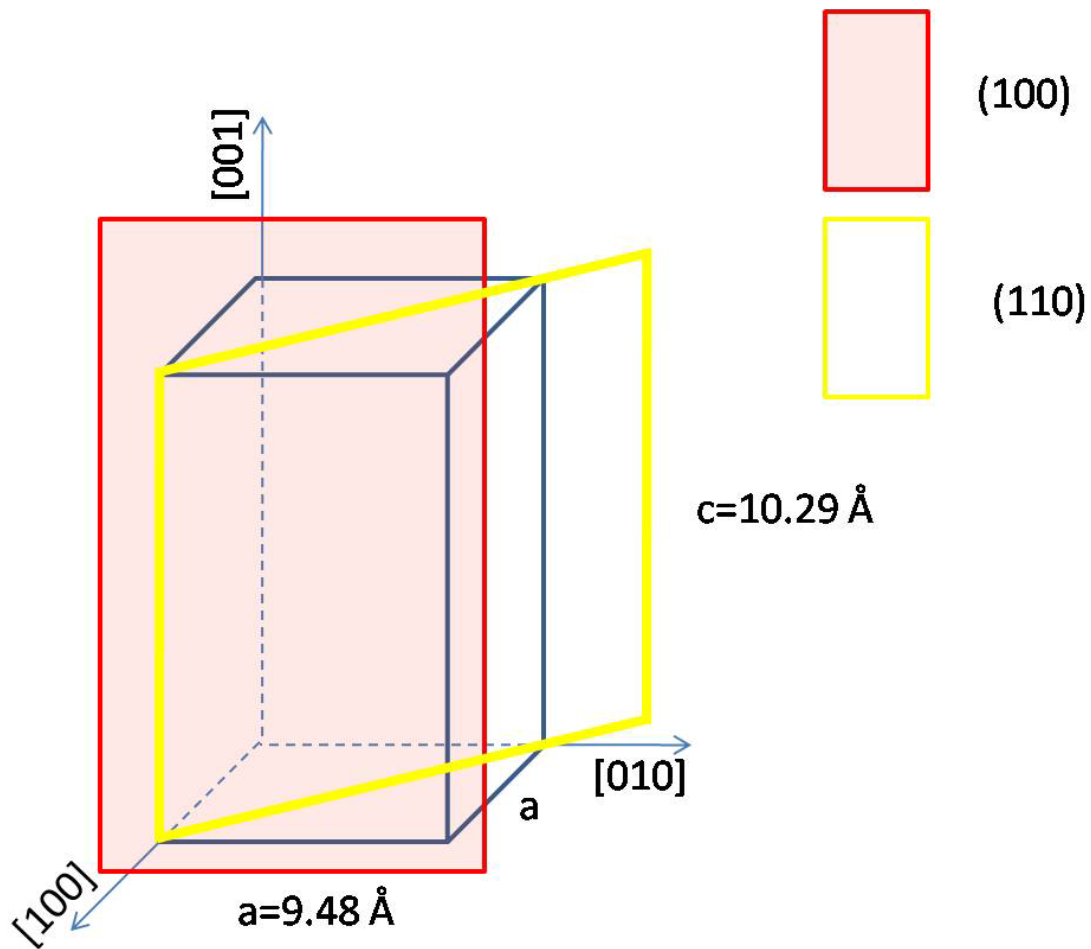
Figure 4.1. Schematic of two surfaces of Li$_2$B$_4$O$_7$(100) and (110) that were used during this research. The lattice spacing of this tetragonal crystal is also provided.

For clarity, Figure 4.2 depicts the same two crystal surfaces; this time with the atomic

constituents present in the surface plane.
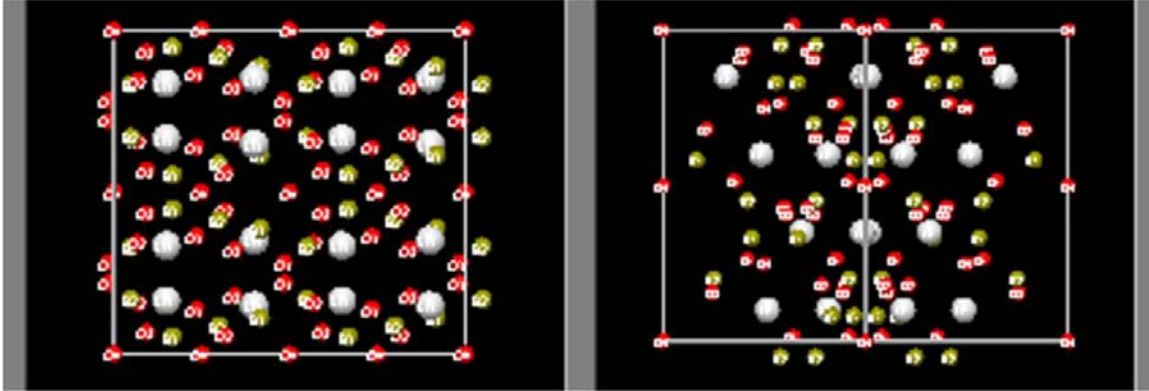
Figure 4.2. (a) 2d projection of $Li_2B_4O_7$(100) and (b) $Li_2B_4O_7$(110). Li, O and B species are represented by gray, red and green balls, respectively. Courtesy of International Centre for Diffraction Data [3]

An actual example of one of the crystals used for this research is displayed in

Figure 4.3.

Figure 4.3. $Li_2B_4O_7$ sample. A penny is also displayed as a size reference.

X-ray diffraction verification

Upon receipt of the samples, the crystal orientations were re-verified and found to

be oriented to better than ±0.5 degrees using x-ray diffraction (XRD) conducted on a

59

Rigaku D/Max-B Diffractometer at the Nebraska Center for Materials and Nanoscience. This instrument possesses a 2 kW Cu target x-ray tube which, after passing through a diffracted beam monochromator, provides radiation at the Cu Kα edge wavelength of 1.54 Å. The sample and detector were rotated with respect to the incident beam angles (θ) up through 45° and spectra were then collected. The XRD shows the orientation from the polycrystalline samples, an example of which is depicted in Figure 4.4.
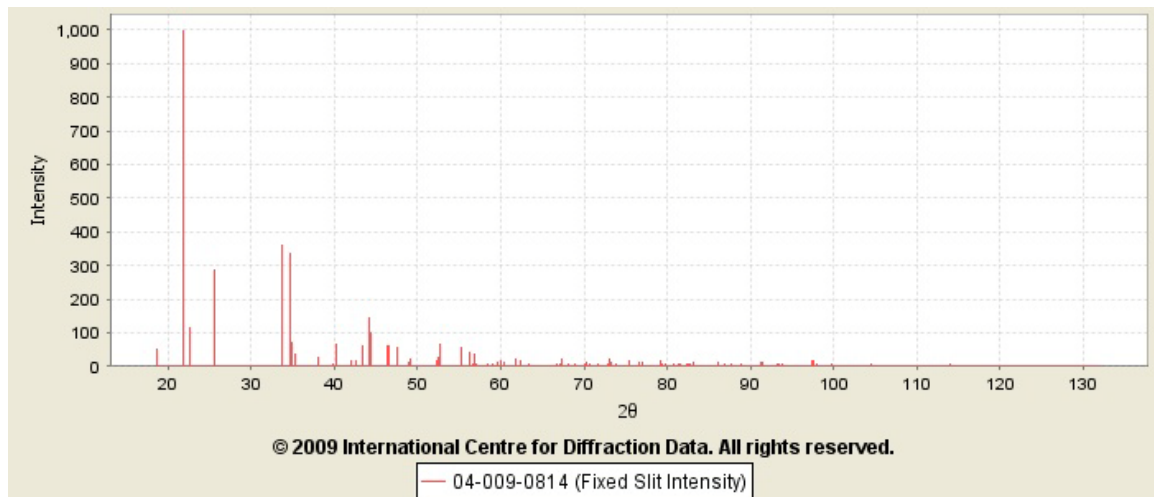
Figure 4.4. Actual spectra of single crystal $Li_2B_4O_7(110)$. Courtesy of International Centre for Diffraction Data [3]

This data set was analyzed against four standards provided by the International Centre for Diffraction Data [3] to ensure the crystal cuts were within tolerance of ±0.5 degrees as stated by the manufacturer, L'viv University, as either $Li_2B_4O_7(110)$ or (100). All the samples used for this research were acceptable according to the International Centre for Diffraction Data standards.

60

Surface preparation of the samples

Prior to mounting, 80% of the sample surface was covered with a layer of 1mm thick graphite paint from the edges towards the center, leaving the very center of the sample exposed for experimentation. This was done to mitigate the extreme charging effect encountered with this wideband gap material [4] when conducting photoemission work.

The surfaces of the samples were cleaned using ethanol prior to mounting. After ensuring samples were in electrical contact with the copper sample holder via tantalum wire spot welding, the sample holder plus sample was placed into the ultra high vacuum sample chamber via a manipulator arm. Figure 4.5 depicts a typical sample holder, upon which a sample was mounted.
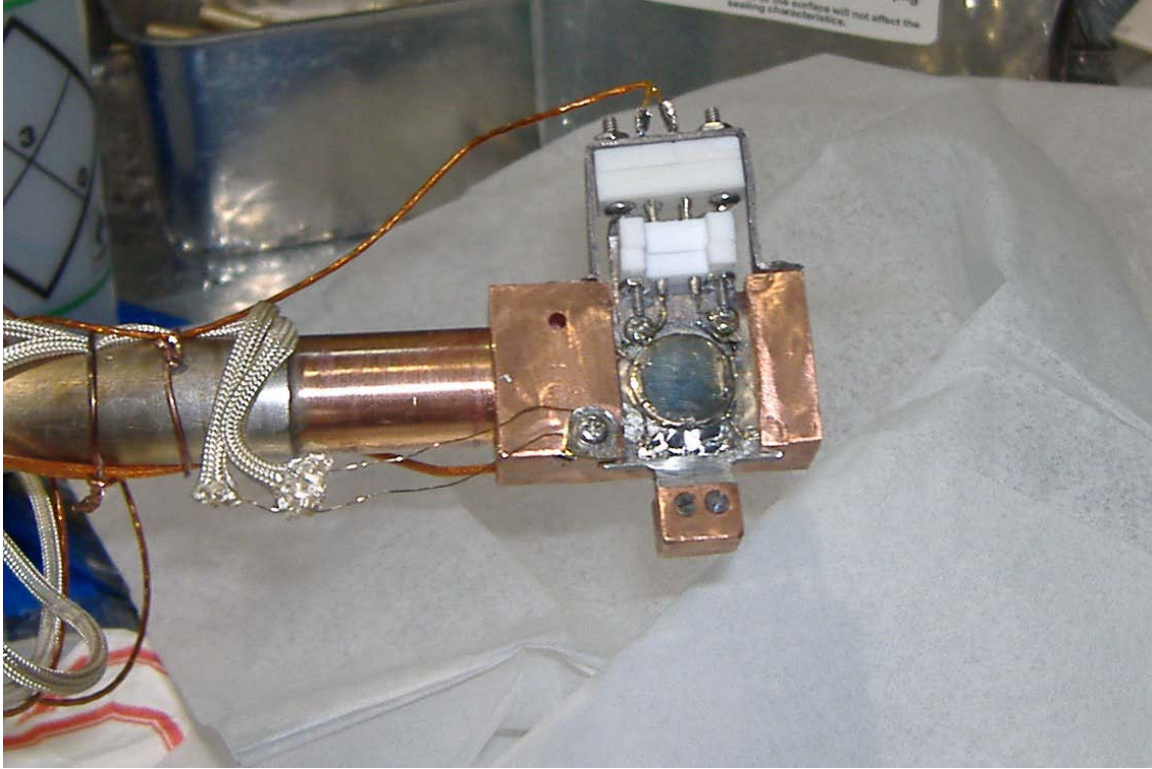
Figure 4.5. Cu sample holder at CAMD used for PES. Sample holders used for IPES at NCMN were similar.

Ultra High Vacuum (UHV) conditions

For both PES and IPES experiments, an UHV condition of a minimum of 10^{-9} torr was essential. For PES, a clean surface had to be maintained with little chance of photoemission occurring except within the desired sample and with a sufficient mean free path. The mean free path had to be large enough for the photoemitted electrons with the correct angle and energy to be collected by the analyzer. For IPES, the concerns were similar. In this case, the electrons from the electron gun must arrive at the clean surface to create the photons; and the photons must leave the chamber to be counted in the active

volume within the Geiger Müller detector. Such a system depicted schematically in
Figure 4.6 was capable of consistently reaching 10^{-10} torr.
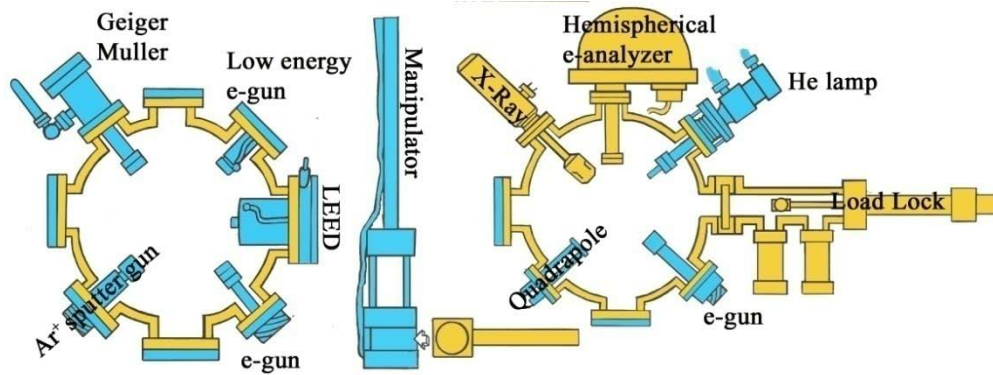
Figure 4.6. Schematic of UHV system used for IPES and ARPES at NCNM courtesy of D. Wisbey [5]

Due to the required UHV conditions, this research was conducted on site at the
Nebraska Center for Materials and NanoSciences (NCMN), University Nebraska
(Lincoln) campus as well as the Center for Microstructures and Devices (CAMD), Baton
Rouge, LA. Along with the features depicted in Figure 4.6 in a nonmagnetic, steel
sample chamber with an interior micro-magnetic shield, the UHV systems used a variety
of mechanical, turbo and ion pumps all necessary to maintain the necessary low pressure.

Final surface preparation

After placing the sample into the sample chamber all samples (PES or IPES) were
subjected to Ar+ sputtering, followed by consistent and gradual heating. The sputtering
was to remove any undesirable surface species prior to collecting spectra. The
systematic, gradual heating was conducted to ensure that any sputtering induced surface
cratering annealed and a smooth surface was available prior to collecting spectra.

Typically, the surface was subjected to sputtering for five minutes at $\pm\,45°$ with respect to the surface normal to ensure consistency. Systematic heating up to 625 K prior to a slow return to room temperature over the course of an hour was typical for the surface annealing.

4.3. PES Experimental Considerations

PES overview

To summarize the experimental set-up, linear polarized photons created within the synchrotron by packets of turning electrons travel through optics and a monochromator into a UHV system to irradiate the LTB sample. The photoemitted electrons at the correct acceptance angle and energy are captured by a hemispherical energy analyzer. They are multiplied via a channel electron multiplier at the end of the analyzer, and then counted. Figure 4.7 depicts the entire system with the exception of where the photons originate. A summary of the critical equipment for angle resolved, energy dependent and polarization dependent photoemission follows along with a discussion on the experimental procedures used for each.

64
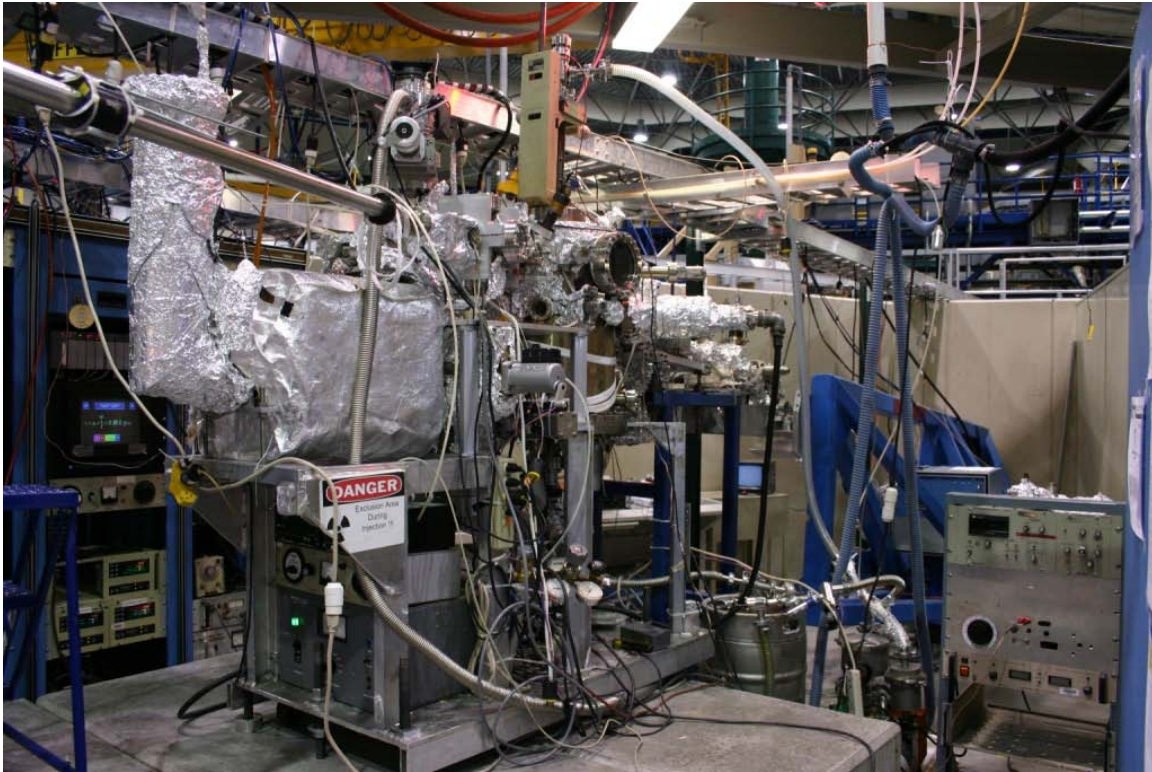
Figure 4.7. CAMD 3m TGM Beamline where all PES was conducted

Synchrotron and beamline

Photoemission spectra were obtained using synchrotron light that is dispersed by a three meter toroidal grating monochromator at the Center for Microstructures and Devices (CAMD). The choice of synchrotron radiation was chosen as the monochromatic source for three primary reasons. First synchrotron radiation provided a very high spectral brightness. Spectral brightness (or brilliance) is defined as the flux per unit area per radiation source per unit solid angle of the radiation cone per unit spectral bandwidth [6]. Focusing the beam to a smaller size necessarily improves the k-vector resolution, and the beamline has been designed for the best match between the source and

65

the electron energy analyzer placement. Apertures can help reduce beam size and divergence but only at the expense of flux. In order to maximize the detection efficiency, an overall quality factor must be and has been considered. Second this light source is linearly polarized. This attribute allows the researcher to identify the symmetry of the bands more easily because the orientation of the vector potential is known. Finally, the synchrotron radiation is tunable. In the particular case of the CAMD 3m/TGM beam line, the operational range is from 15 – 180 eV, which allows full mapping of the $Li_2B_4O_7$ band dispersion for the occupied valence bands from low energy quasi-core up through E_{Fermi} [7]. A schematic of the beamline is depicted below in Figure 4.8.
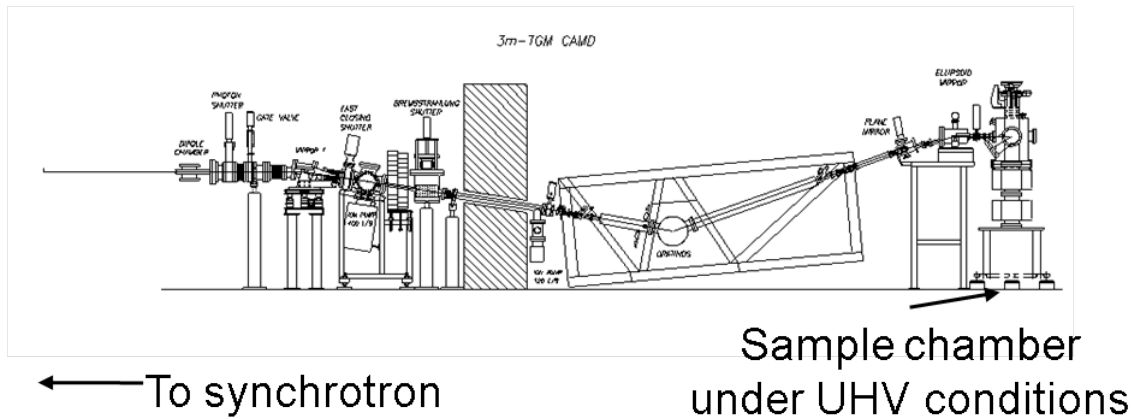
Figure 4.8. Cross section of the 3-meter Toroidal Grating Monochromator (3m/TGM), Port 6B beamline where $Li_2B_4O_7$ ARPES will be conducted. This beamline has an operational range of 15 - 180 eV with resolving power greater than 1000; i.e. 30 to 130 meV in the operational range of photon energies [7].

Hemispherical energy analyzer

For this research, the 3m TGM beamline configuration was equipped with a photoemission endstation with 50 mm hemispherical electron energy analyzer [7]. Figure 4.9 provides an example of an analyzer 10 times the size used for this research.
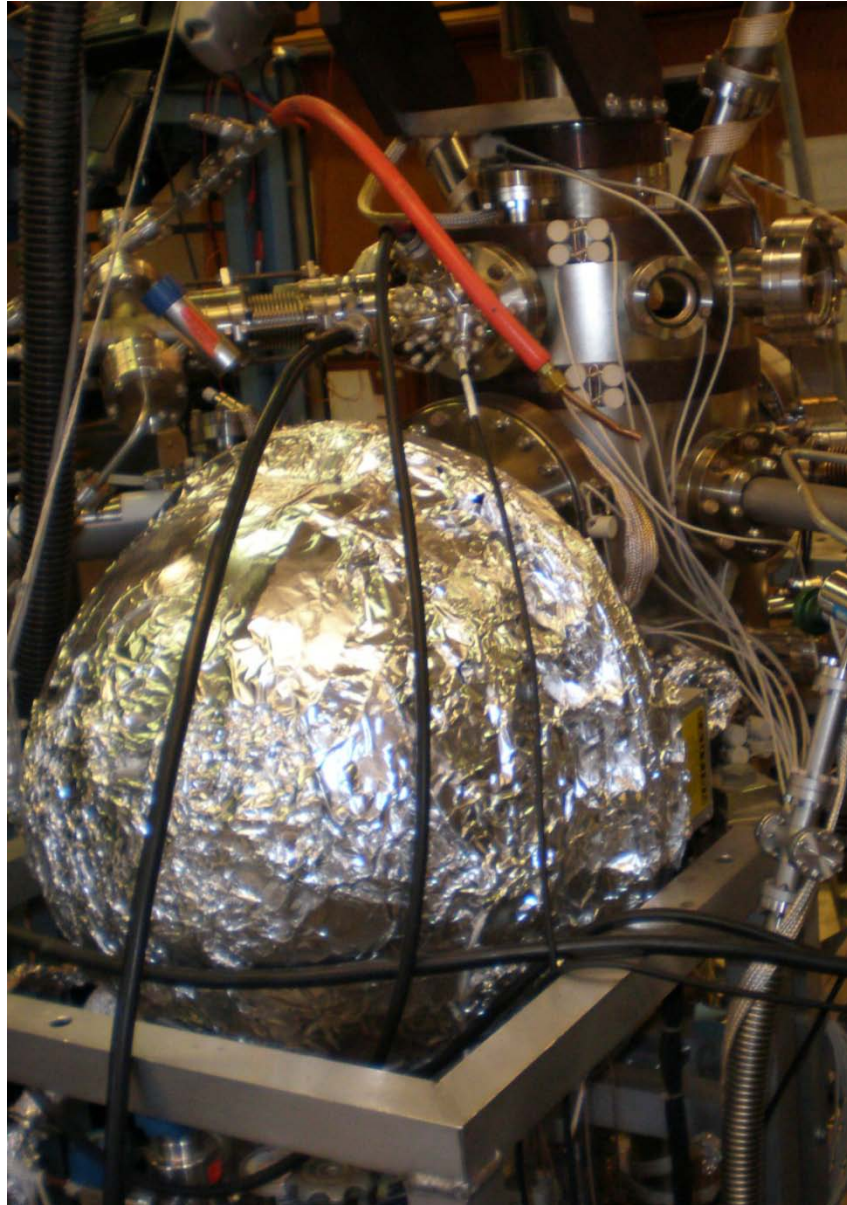
Figure 4.9. Typical hemispherical analyzer at the NCNM, University of Nebraska.

The hemispherical electron energy analyzer operates with a 1/r field between two concentric hemispheres. This field acts as a filter for the photoemitted electrons originating from the sample. Only electrons with a particular energy and correct angle are able to make it into the analyzer and pass completely through into the channel electron multiplier [8]. The analyzer possesses two key parameters that impact the energy resolution. They are the adjustable pass energy and the ratio of the slit size to the hemisphere separation. The angular acceptance of the analyzer is $\pm$ 1 degree, while the pass energy is typically set for 10 V. The combined resolution of the PES system to include all optics, electron energy analyzer (and monochromator) is approximately ±70 meV for photon energies up to 100 eV, with higher value photon energies above 100 eV, the combined resolution rises to approximately ±150 meV [7].

Data acquisition software

Sample data acquisition software was the 12th iteration of software written for this instrument and now operating under a current version of Visual Basic. This particular program created a scan with either the photon energy (constant initial state) or by emission kinetic energy based on the actual measurement of the multiplier counts of flux with the counts. All the raw and normalized data were manipulated in Origin 6.0, 7.5, or OriginPro 8.0 [9] into usable information as depicted in the subsequent procedural section.

ARPES procedure

After conducting sample preparation as described above, the sample was fixed at 45° with respect to the photon source. Most of the recorded angle resolved data was gathered at a temperature of 623$\pm$5 K. The analyzer was rotated in 0.5° steps from -3.0°

68

off normal to sample up through a minimum of 12.0°. At each 0.5°, step a minimum of

three intensity versus kinetic energy spectra were taken. These were then averaged to

provide the composite spectra. An example of one is provided below in Figure 4.10.
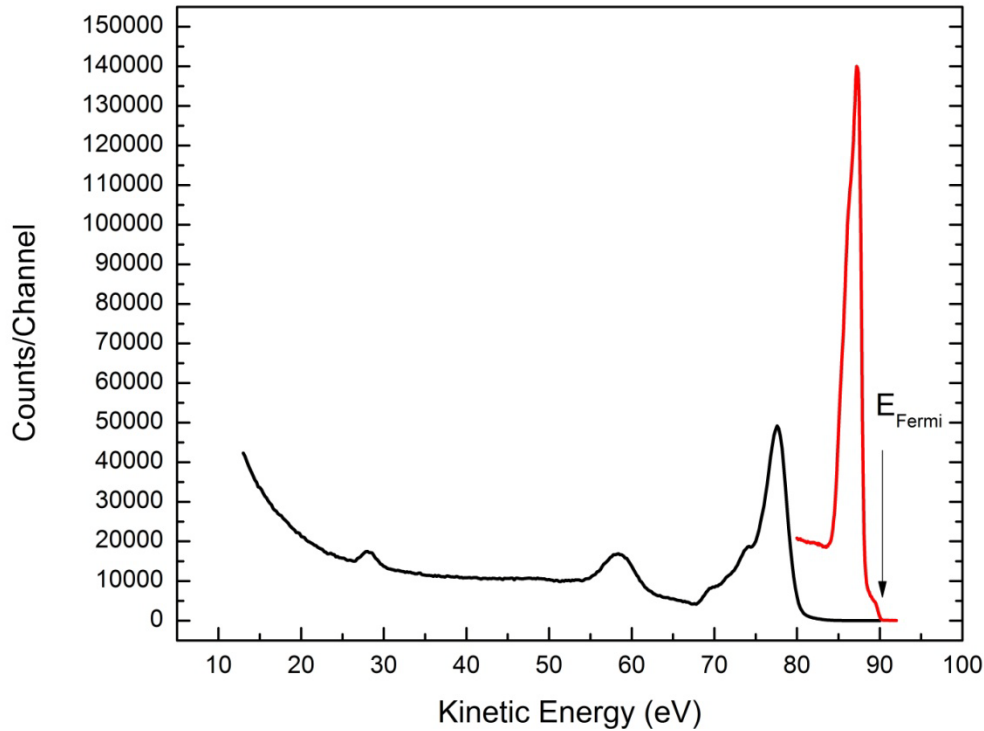
Figure 4.10. Sample raw spectra of intensity versus kinetic energy of Li$_2$B$_4$O$_7$(110) (black) and Cu (red) at 95 eV and T = 623±5K. Along with Ta, the latter metal was used to determine E$_{Fermi}$ as indicated.

Although the elevated temperature mitigated some of the charging effects

common to large band gap insulators, it was always necessary to adjust the raw spectra

using both Li 1s and O 2s core level energy levels to some degree. This effect was more

pronounced at lower temperatures as indicated in Figure 4.11.
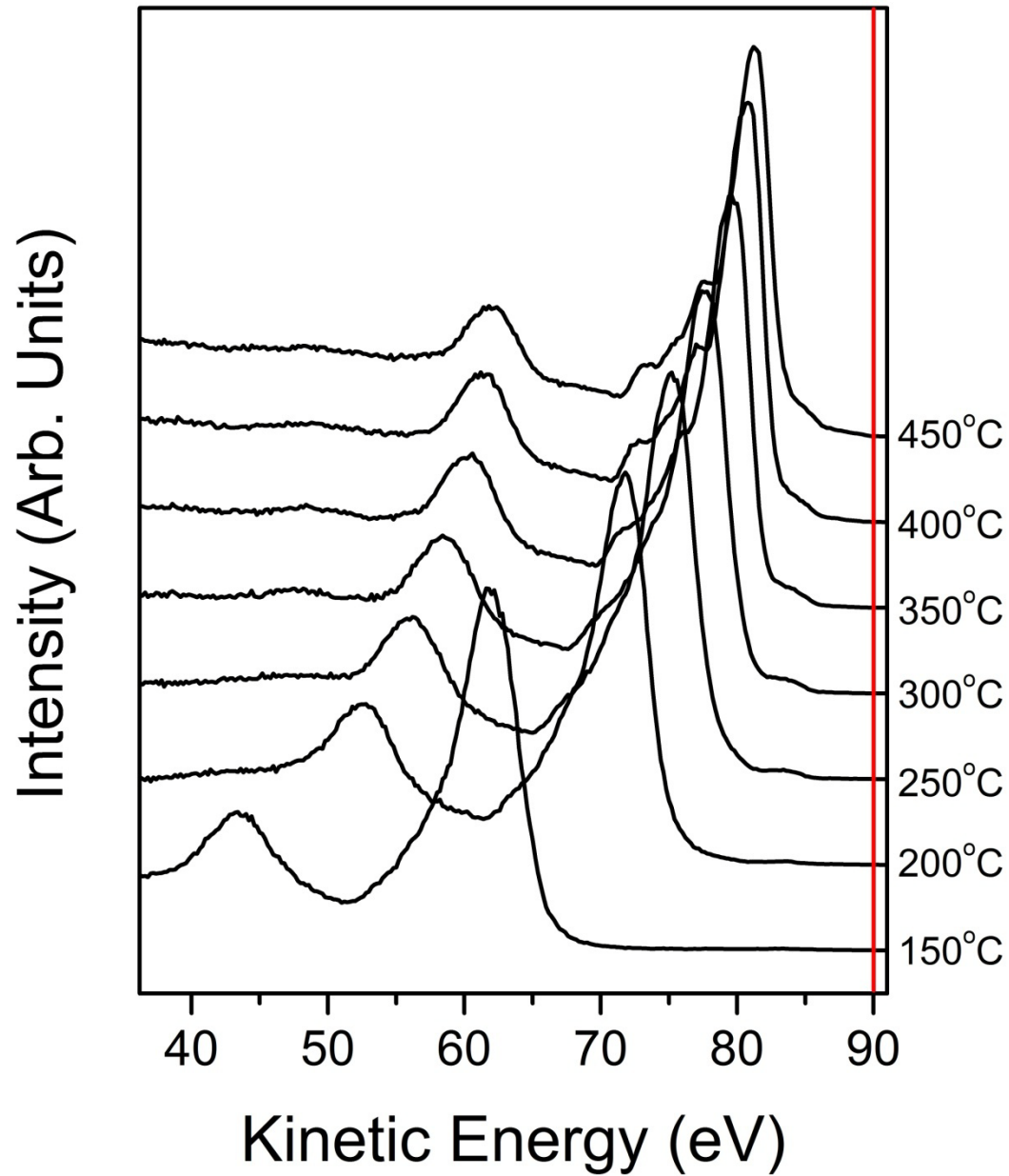
Figure 4.11. The photoemission spectra from $Li_2B_4O_7(110)$ surface taken with the in-plane $\underline{E}$ vector oriented along [1$\underline{1}$0] for a succession of temperatures (from bottom to top). The photoemission spectra were taken at a photon energy of 95 eV with electrons collected along the surface normal. E_{Fermi} is depicted with a red line.

Further, the different surfaces indicated different temperature dependencies as indicated

in Figure 4.12; the details of which will be addressed more thoroughly in Chapter 7.

What is important here is to demonstrate that both surfaces have photovoltaic charging

that must be considered; and that they have been considered and addressed.
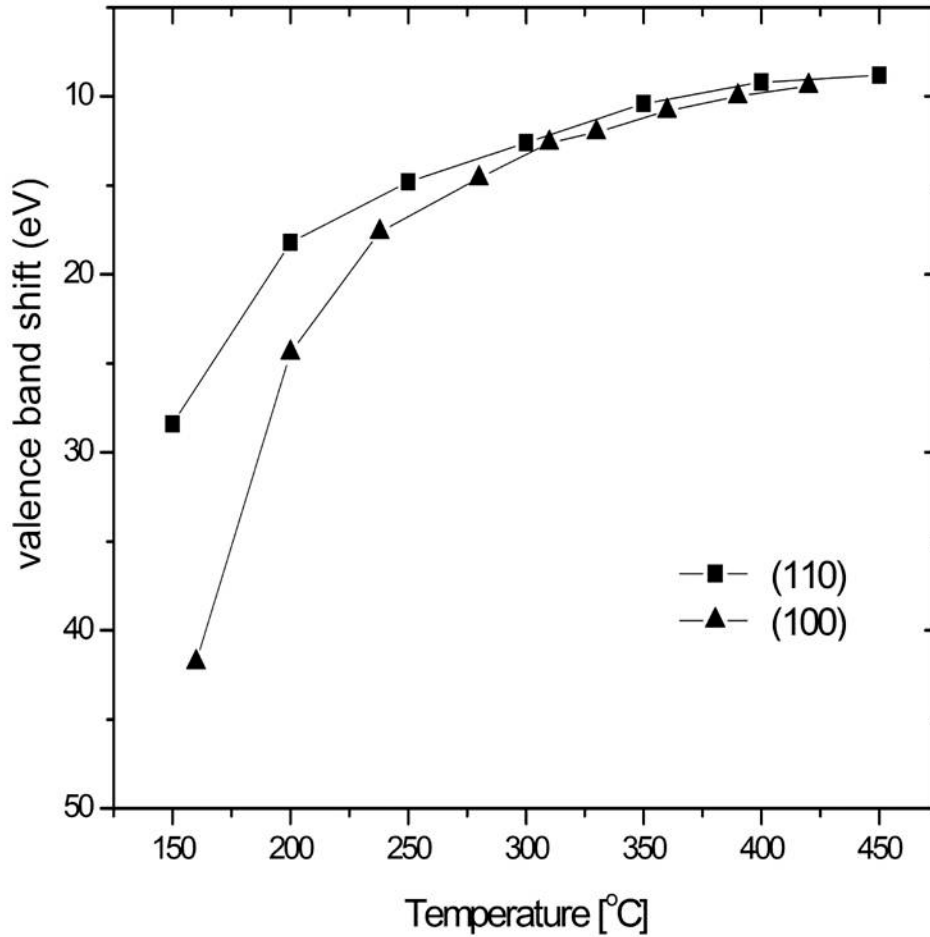
Figure 4.12. Position of the valence band maximum for both the (110) and (100) surfaces of Li$_2$B$_4$O$_7$, as a function of temperature. The data was obtained from photoemission spectra taken at a photon energy of 95 eV, with the photoelectrons collected normal to the surface.

It was not feasible to heat the samples high enough to ensure complete mitigation

of photovoltaic charging. However, the samples were heated sufficiently so the effect

was negligible. But to ensure even this negligible effect was properly accounted for in

the reference points (Li 1s and O 2s core energy levels), the core energy level

71

adjustments were checked against an absolute theoretical value based on an optimization

of a least squares fitting of real data to the following relationship:

$$y = Ae^{-BT} + y\ intersect \tag{43}$$

where A and B are fitting constants, y is the shift (in eV) away from E_{Fermi} of the largest

peak valence band density of states, T is the temperature and y is the absolute value of the

intersect for a given surface with no photovoltaic surface charging present. An example

of this is depicted pictorially for $Li_2B_4O_7(110)$ in Figure 4.13Figure 4.13.
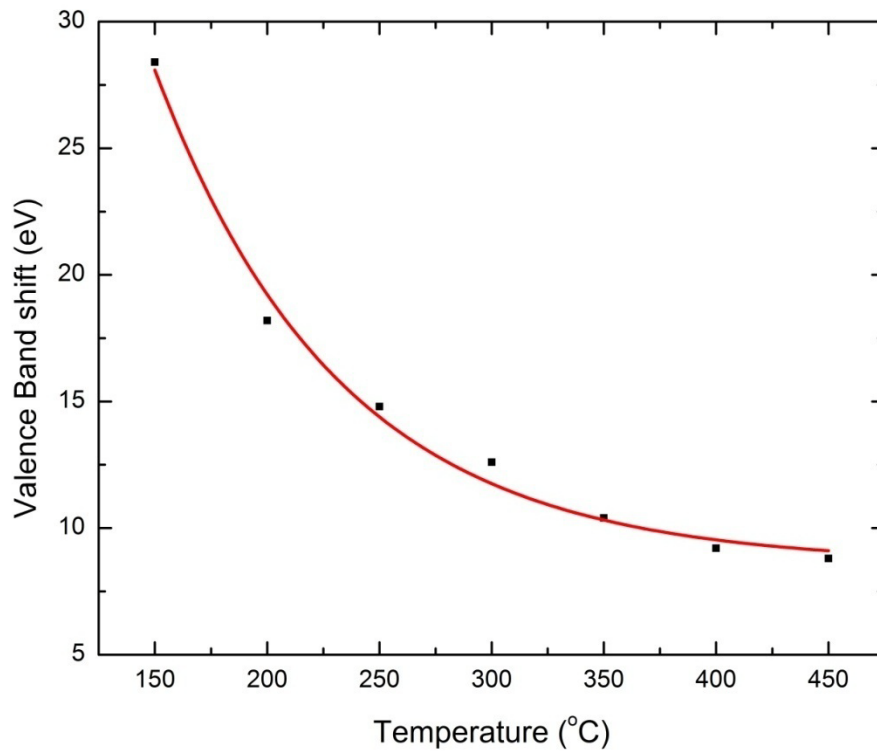
Figure 4.13. Least squares fit of valence band shift from E_{Fermi} versus temperature as measured from largest valence band peak for $Li_2B_4O_7(110)$

72

Once the reference points were deemed correct, all raw spectra were adjusted for charging. Shifting from kinetic energy to binding energy scale with E_{Fermi} as the designated zero reference point simply becomes:

$$E_{BE} = E_{KE} - E_{Fermi\,(KE\,value)} \tag{44}$$

where $E_{Fermi\,(KE\,value)}$ is the kinetic energy value of the experimentally determined E_{Fermi}. It should be noted that the real kinetic energy value of the electrons entering into the analyzer is actually greater than E_{KE} by the work function of the analyzer, which is not included for the above scale change.

After adjusting for binding energy scale, the background was adjusted to zero for each of the spectra by using values greater than E_{Fermi}. At this location, there should not be any primary electrons coming from an insulator during a photoemission process. This value is unilaterally subtracted for the spectra.

Next the spectra were adjusted to remove secondary electron influence, which follow a general relationship:

$$I_{secondaries} = Ae^{-B(KE)}. \tag{45}$$

Here, the fitting constants (A and B) were determined by fitting the above equation to known intensity values at select locations far from any primary features. KE represents the kinetic energy of the electrons that were counted. After determining the parametric fit, the same equation is used to subtract the secondary electrons for each spectra. Although close in value, it is worth pointing out that each spectrum had its own different parametric fit of this secondary electron tail due to the complexities of the unique photon environment, temperature, and angle; all of which resulted in slightly

different shift of peaks of interest. However, the maximum shift from this analysis was never more than 0.3 eV.

After scaling to zero background and adjusting for secondary electrons, the spectra are adjusted for the variation of intensities caused by the experimental conditions. Primarily due to the differing photon flux environments, individual absolute intensities varied greatly; particularly when comparing one data set taken immediately after electron injection into the ring to one taken just prior to re-injection. This photon producing ring current source undergoes exponential decay; with the photon flux varying greatly between the extremes, and must be considered. Since we were primarily concerned with relative intensities, we chose data away from any primary features as a location to normalize the spectra. Using Figure 4.10 as an example, we would use features left and right of the O 2s peak. We used the saddle point to the right of the peak (located at 67 eV) and also 5 eV to the left of the peak (for the Figure 4.10 example it would be at 53 eV) as an alternative location if there was any ambiguity. An average of three points within 0.3 eV was used as the normalization value for comparison. The highest value in our spectra at the reference point was kept, $I_{Ref\ high}$, and the remaining intensity values of each spectra were normalized by multiplying the original value by the simple ratio (R):

$$R = \frac{I_{spectra}}{I_{Ref\ high}}. \tag{46}$$

Here the $I_{spectra}$ is the value of the intensity for the individual spectra at the reference point. The intensities that follow in the analysis chapters (Chapters 5 through 9) are all relative intensities, unless stated otherwise, and should be treated as such. However,

74

since we were primarily after the peak locations and only interested in their relative intensities this procedure will suffice.

After conditioning the spectra as describe above, the peak locations for the valence band as well as the shallow quasi-core levels were determined by fitting the experimental spectra with Gaussians with a width at half peak maximum greater than the overall system resolution of 0.5 eV. The choice to use this line function to fit any observed spectral features follows logically. Initially, it might be reasonable to assume a Doniac-Sunjic line shape as might be applied to a core level, but given the incorporation of Heisenberg's uncertainty principle to the lifetime of the state and the quasi-particle effects on the band structure (electron-phonon coupling), the line shape becomes much more symmetric and close to a Gaussian line shape in the valence band region. Since $Li_2B_4O_7$ is an insulator, it would be expected that the symmetric line width contribution should also be due to differential charging [10]; but we have already adjusted for this effect as discussed earlier. Regardless, this lifetime effect, in addition to the overwhelming contribution due to phonon broadening given the operating temperature and UV energy range used for the sample, provides us confidence in choosing to incorporate a least squares fitting of spectral features using only a Gaussian line function [11] as displayed in Figure 4.14.

Additionally, an excellent signal-to-noise ratio is maintained throughout the PES portion of the research for a low Z insulator, with spectra count rates in excess of $2x10^4$/channel-second. (For the IPES measurements, the inherently lower counts were mitigated with much longer integration times as discussed later.)
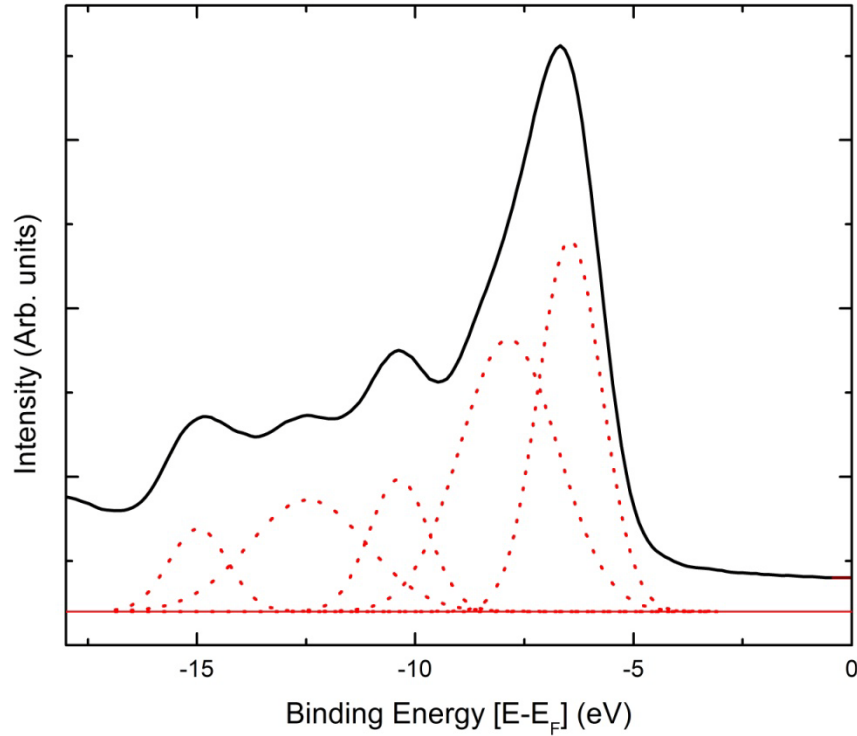
Figure 4.14. Example of peak fitting of valence band features for ARPES of $Li_2B_4O_7(100)$ with $\underline{E}$ oriented [010] at 0 degrees with respect to analyzer and sample normal. The deconvoluted features are depicted below the actual spectra in red.

Finally, the theoretical models predict considerably more states than the five shown. However, these additional features reside below the energy resolution of our spectra, the finite temperature effects and lifetime being dominant, and could not be experimentally resolved. These theoretical models assume zero Kelvin, infinite resolution and a ground state for calculation. In contrast to theory, we have chosen the more conservative approach of only fitting features if they can be observed. At a photon energy of 56 eV photon energy, all five key predicted features within the valence band were distinctly observed. At higher energies, this was not always the case.

76

Once the peak centers were identified, it was a relatively straightforward process to determine the parallel wave vector, $k_\parallel$, as discussed in Chapter 3 in order to obtain the desired surface map:

$$k_\parallel = \left(\frac{2m}{\hbar^2}\right)^{0.5} \sqrt{E_{KE}} sin\theta = 0.512\sqrt{E_{KE}} sin\theta \; [\text{Å}^{-1}]; \tag{47}$$

with the symbols as previously defined. The only exception here is that E_{KE} now must include the analyzer work function to obtain the true kinetic energy of the emitted photoelectrons. The work function was a simple table look-up and was approximately 4.3 eV for the example in Figure 4.14.

The band mapping strategy

The $Li_2B_4O_7$ samples were mapped along four of their non-equivalent high symmetry directions across the $Li_2B_4O_7(110)$ and $Li_2B_4O_7(100)$ surfaces as depicted in Figure 4.15.
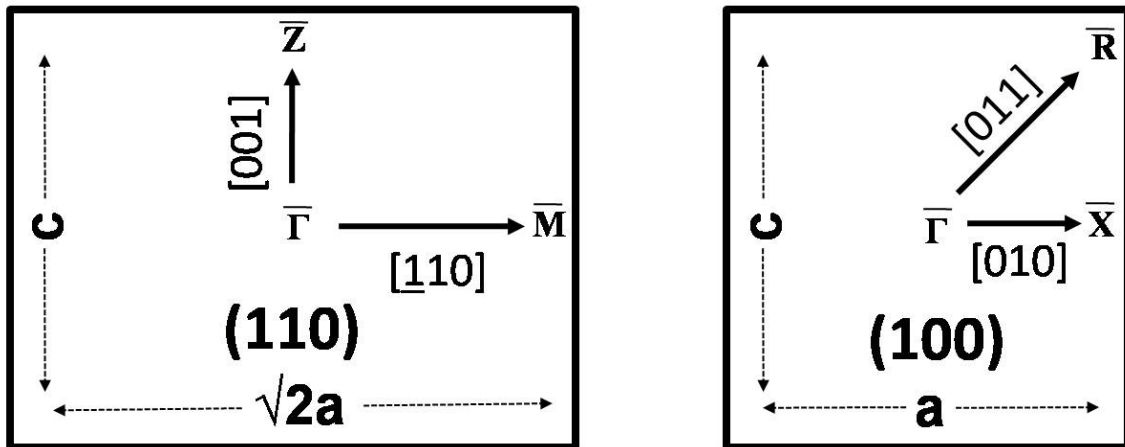
Figure 4.15. (a) $Li_2B_4O_7(110)$ and (b) $Li_2B_4O_7(100)$ crystal faces indicate the crystal directions in both real and momentum space that will be mapped for each along with the lattice spacing.

After mapping along [$\underline{1}$10] and [001] for (110) and [010] and [011] for (100) from -3° through +12° for photon energies of 56 eV and 70 eV using the high energy grating, the same was done using the low energy grating for 35 eV and 45 eV photon energies. Mechanical difficulties allowed for one iteration of the angle resolved data at the lower energies only. For the higher energies, a minimum of three iterations were conducted to ensure repeatability. Consequently, the preponderance of the analysis to be discussed in Chapter 7 will be focused on the more reliable higher energy data. Since the analyzer could only be moved in a 360 degree plane, this required remounting to cover the four high symmetry directions desired. The comprehensive results of the procedure discussed in this section on surface band structure will be presented in Chapter 7.

Energy dependent photoemission procedure

The majority of what was discussed in the previous section was relevant for mapping of the bulk via energy dependent photoemission. Only the differences will be presented in this section.

In essence, mapping the bulk band structure was very similar to that of mapping the surface band structure, this time in the [110] and [100] directions. However, instead of varying the angle to move through surface Brillouin Zones (BZ), the photon energy is changed to provide different kinetic energy values for the same peak. This showed different perpendicular locations, in momentum space, through the bulk BZs. An example of a typical series of measurements is provided in Figure 4.16.
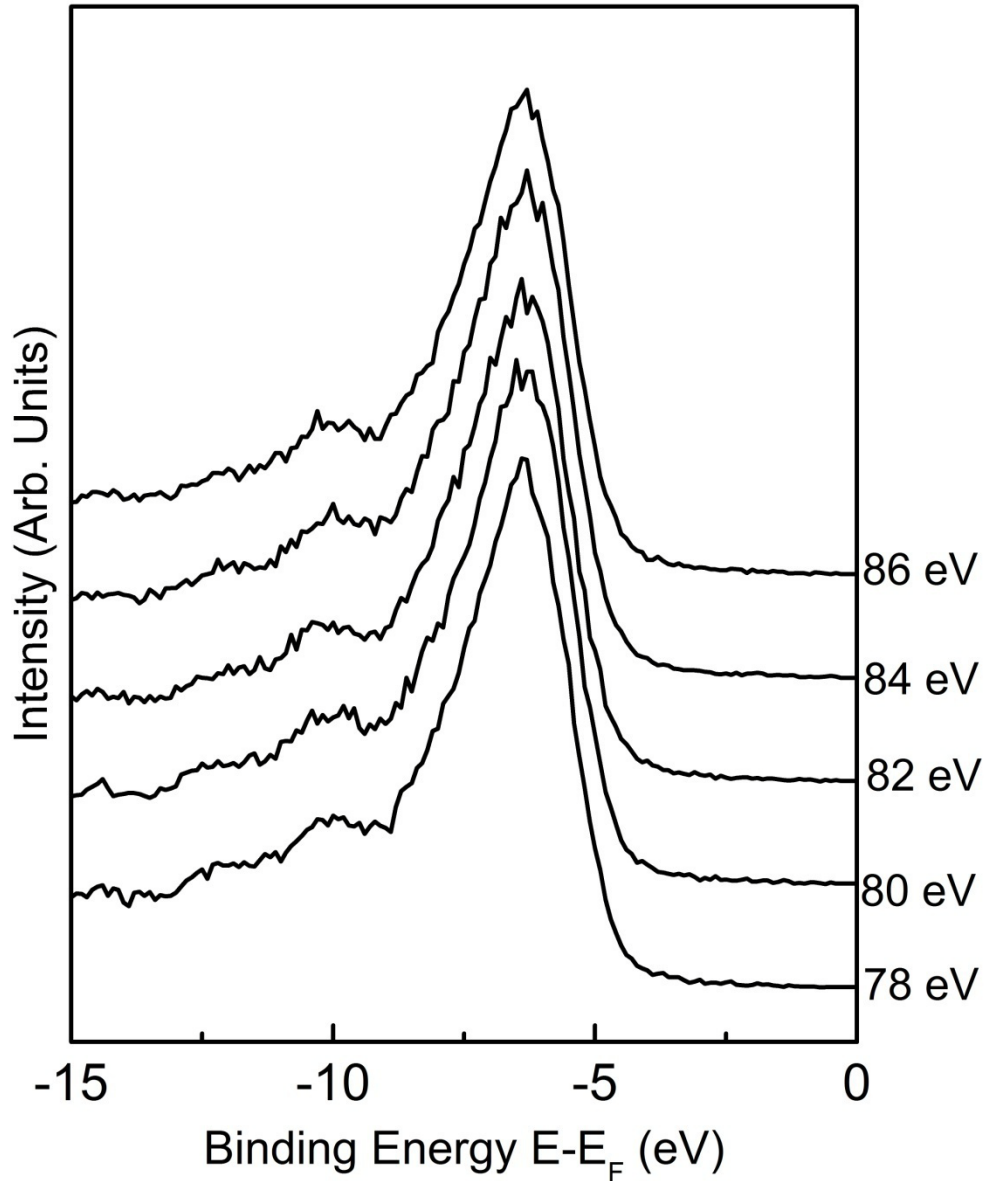
Figure 4.16. Example of relative intensity versus binding energy of energy dependent photoemission results for solid $Li_2B_4O_7$(100) oriented [010]. Analyzer is normal to sample; synchrotron light source varies from 78-86eV in steps of 2 eV and is 45° with respect to sample. Temperature = 350 ± 5°C.

As discussed in Chapter 3, and summarized below, the relevant equation that

allowed us to determine the perpendicular wave vector component was:

$$k_{\perp} = \left(\frac{2m}{\hbar^2}\right)^{0.5} \sqrt{E_{KE} + U_o} cos\theta = 0.512\sqrt{E_{KE} + U_o} \left[\mathring{A}^{-1}\right]; \qquad (48)$$

where the symbol definitions are as before. Here, $cos\theta$ always equals 1, because the sample was always normal to the analyzer and the inner potential, U_o, is initially assumed as zero. The details of the latter will be discussed further in Chapter 7.

Finally, by the nature of its thin cut, mounting became possible only in the direction of the crystal cut. Consequently, $Li_2B_4O_7(110)$ and $Li_2B_4O_7(100)$ only allowed two directions to be mapped, [110] and [100], respectively.

Light polarization dependent photoemission procedure

Figure 4.17 below provides a diagram of this photoemission technique.
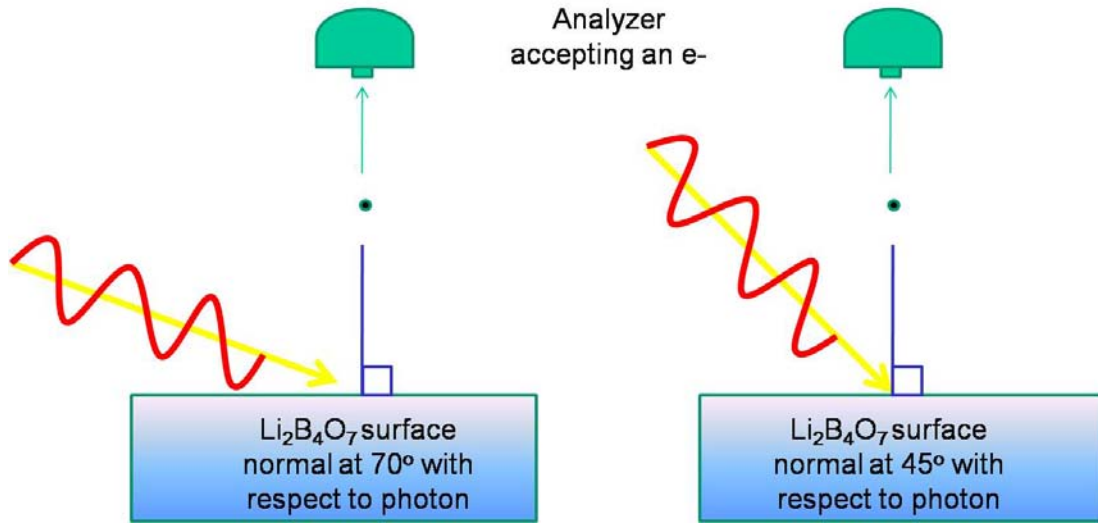
Figure 4.17: Schematic of light polarization dependent photoemission procedure used

In this technique, the angle of the sample was varied with respect to the photon source from 45° (S+P) to 70° (P) and then the analyzer was adjusted so that photoelectrons were always normal to the sample surface. Additionally, the measurements were conducted

80

with a minimum of two different photon energy values for all four orientations as discussed in Chapter 7. An example of the different spectra for this technique is presented in Figure 4.18.
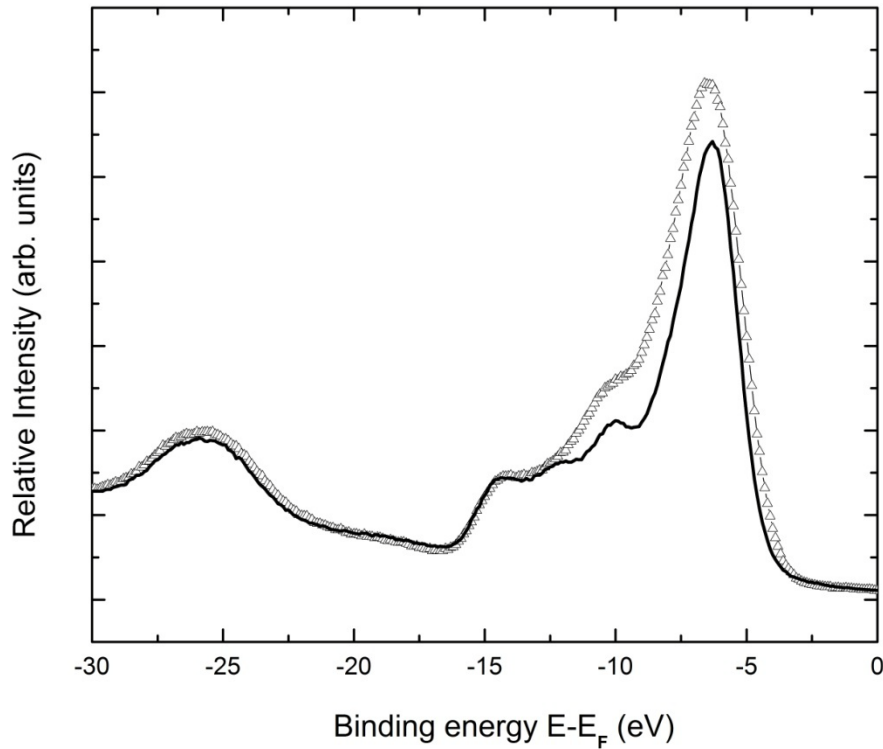
Figure 4.18. Example of experimental light polarization dependent photoemission spectra for $Li_2B_4O_7(100)$ The photon energy is 70 eV with the photoelectrons collected along the surface normal; the orientation of light incidence angle was either 70 degrees {-Δ-Δ-Δ-} or 45 degrees {——} with respect to surface normal. <u>E</u> is oriented along [010]. Aspects of this have been previously published [4].

The discussion of the results obtained from this technique will be presented in Chapter 7.

4.4. IPES Experimental Considerations

IPES overview

Under the same ultra-high vacuum conditions as PES, electrons of a set mean energy and rate were fired from a low energy electron gun into a $Li_2B_4O_7$ sample at a set temperature. As discussed in detail in Chapter 3, all the bands below the Fermi level were occupied. This forced the free electrons that transition to bound electrons to only occupy the empty states above the Fermi level. As the electrons transitioned from a free to a bound state, a photon equal to the energy difference was emitted and traveled through the window of the Geiger Muller detector into the active region of the detector. The charge pairs created were then amplified and recorded as a current pulse. A summary of the critical equipment for inverse photoemission—not addressed previously— follows along with a discussion of the experimental procedures used.

Electron gun and power supply

The Kimball Physics Inc. ELG-2A/EGPS-1022B Electron Gun and Power Supply System was the electron gun system that was used in this study. It had an energy range from 5 eV to 2000 eV, but the lower end of this capability was of greater interest for this research. This gun delivered up to a 1 μA Gaussian shaped spread of 10 eV ±0.4 eV electrons into an approximately 1 mm diameter spot with up to a 2 cm working distance. The gun is depicted schematically in Figure 4.19.
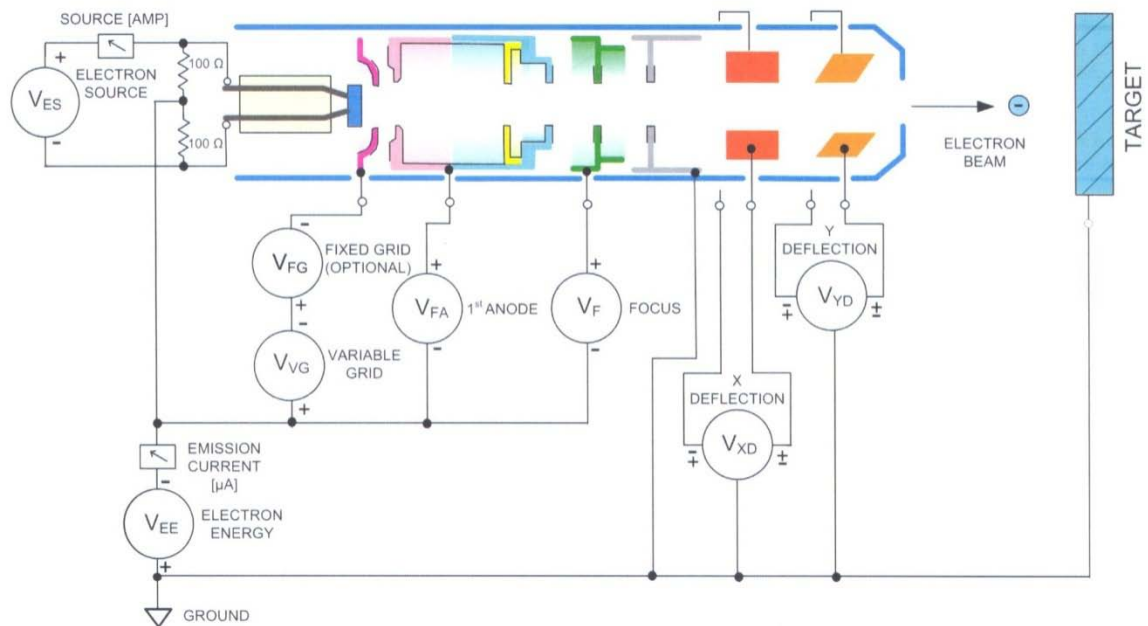
Figure 4.19. Schematic representation of Kimball electron gun used for IPES experiment. Courtesy of Kimball Physics Inc. [12].

The power supply system of the same system is depicted below in Figure 4.20.

Figure 4.20. EFPS-1022B Power Supply depicting typical energy, and emission for IPES experiment.

83

Electron guns of this type operate because they possess a cathode that thermionically emits electrons when a voltage is applied. Electron emission is both a function of the cathode temperature as well as the electric field difference between the cathode and anode. At relatively low temperatures, with high voltage differences between cathode and anode, electron current density can best be described by the Richardson-Dunshman equation:

$$J = AT^2 e^{-\varphi/kT} \tag{49}$$

where J is emission current density, A is the Richardson's Constant for the cathode material ($A = 37$ amps/cm^2/K^2), T is the cathode temperature, φ is the work function of the cathode material in eV, and k is the Boltzman constant [12].

Geiger-Müller counter

The Geiger-Müller (GM) counter present in the IPES system and used for this research was manufactured at UNL. It is based on similar principles to that of a band pass filter, and is depicted schematically in Figure 4.21.
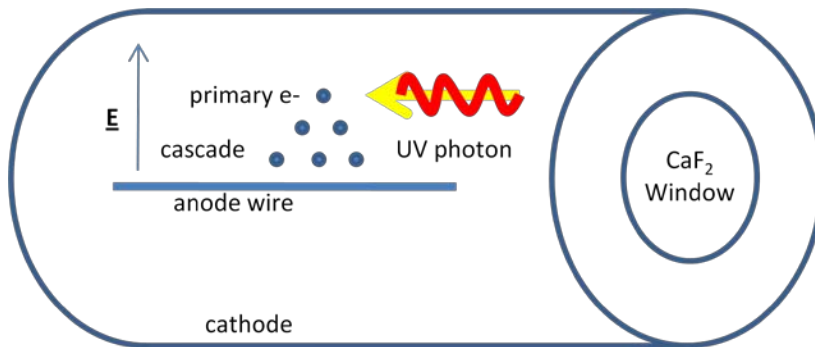
Figure 4.21. Schematic of Geiger-Müller counter used for IPES experiment.

The low pass filter was decided by the window choice. For the purposes of this research, an entrance window of CaF_2 (hv = 10.1 ± 0.2 eV) was the choice used because it allowed the full empty state range to be measured. The choice of window allowed all photons from 0 to 10.1 ± 0.2 eV to enter the chamber. With the introduction of a photon of sufficient energy into the active volume originating from the sample, the I_2 molecules within the Iodine-Helium gas mixture were then ionized. For maximum efficiency the mixture of gasses was 0.17 torr and between 12 to 18 torr for I_2 and He, respectively. The ionization event occurs typically at energies at a minimum of 9.2 eV. In other words, this gas mixture acted as a high pass filter that allowed only photons of the minimum energy. The negative electrons accelerated towards the center anode wire in the center of the GM tube; while the negatively charged walls attract the positive iodine ions. This triggered a cascade effect with the He atoms amplifying the signal; which produced the recorded current pulse. The average resolution of the IPES system including GM counter and electron for this energy range was approximately 400 meV full width at half maximum as has been established experimentally in previous research [13, 14].

Software

In addition to the Origin versions 6.5, 7.0 and OriginPro 8.0 software [9] already discussed; a National Instruments LabVIEW version 8.5 program controlled the energy of the EGPS-1022B for the IPES system. The latter provided a raw spectrum of data that was manipulated further with the Origin software. The potential differences and feedback for the electron gun were manually set by the EGPS-1022B.

IPES procedure

Although IPES systems share many of the same techniques for preparing the samples, there are some significant differences compared to that of PES. Where different, the procedural differences will be discussed in this section.

In conducting the surface mapping, the energy was swept from 5 to 20 eV to ensure the full empty state range was mapped—from E_{Fermi} level up past E_{vacuum}. An example of the raw spectra is provided below in Figure 4.22.
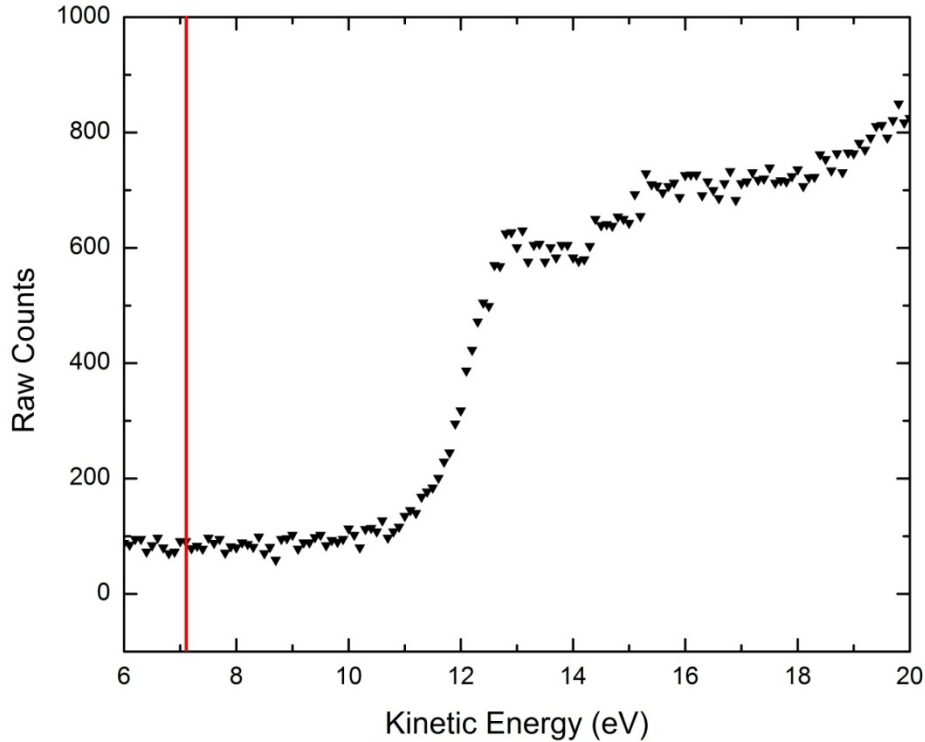
Figure 4.22. Example of raw data gathered from $Li_2B_4O_7(110)$ using the IPES system. This spectra is oriented [$\underline{1}$10] with sample normal at 0° with respect to incident electrons. Note that E_{Fermi} is depicted by the red line.

86

E_{Fermi} was determined as 7.2eV using an Au standard for the same system. The electron

gun's energy steps were 0.1 eV, with a total system resolution of ±0.4eV. Using a

Labview program to obtain the initial spectra, a minimum of one hundred and twenty

iterations for each energy step were conducted. This ensured a statistically meaningful

result due to the considerably lower IPES cross section as discussed previously in

Chapter 3. The spectra were obtained as displayed above. All further manipulations of

the raw spectra were done using a version of Origin as discussed previously.

Next the raw data had to be normalized against the variable sample current, an

example of which is displayed below in Figure 4.23.
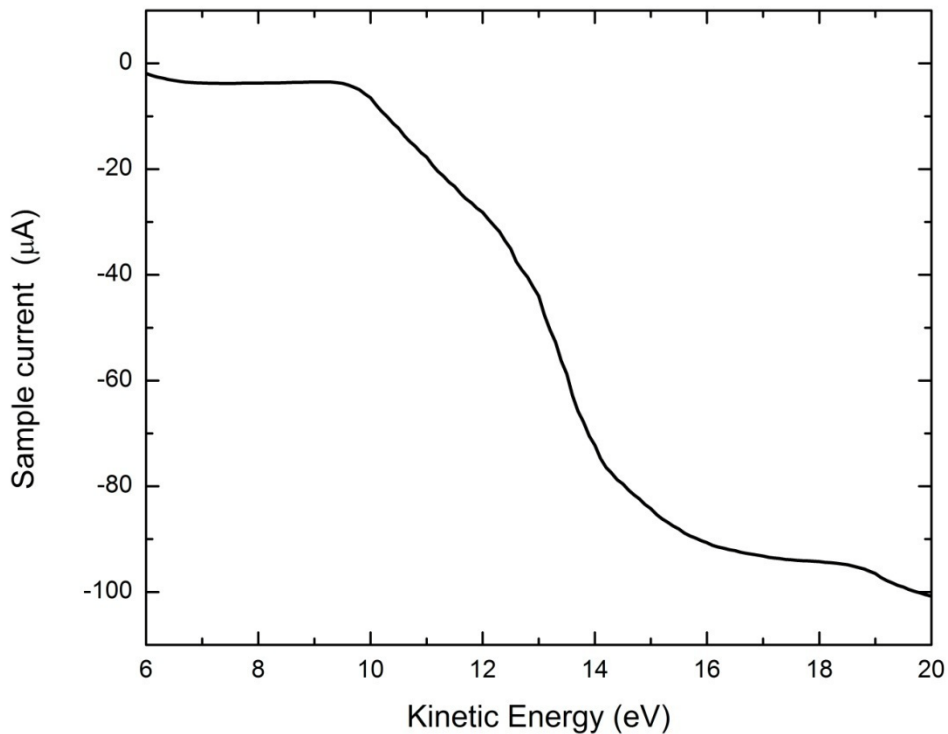
Figure 4.23. Example of nonlinear sample current versus energy spectra due to the electron gun from $Li_2B_4O_7(110)$ using the IPES system. This current spectra is from a sample oriented [110] with sample normal at 0° with respect to incident electrons. The negative current is due to the nature of the charge carrier.

After normalizing for current, the background was determined using an average of points to the left of where E_{Fermi} was located. This choice was made because it was not expected that any contributions in this region would be due to any actual inverse PES events. All the spectra were then subsequently scaled.

Similarly to PES, a point was selected from which to normalize the spectra. To avoid a location where a non zero density of states could exist within the empty states, this choice was typically within the continuum range. The spectra were normalized to the value of that found for the sample at 0° to provide relative intensities.

Finally, a conduction band adjustment due to charging was made due to the changing dipole direction with angle change. Typically, the lower angles required more conduction band adjustments. As depicted in Figure 4.24, a linear fitting function was applied to the middle third of the conduction band edge onset for each spectrum to determine the relative amount of shift required.

88

Equation	y = a + b*x		
Weight	No Weighting		
Residual Sum of Squares	255.42857		
Adj. R-Square	0.96663		
		Value	Standard Error
B	Intercept	-1548.42857	128.34843
	Slope	178.57143	13.50737
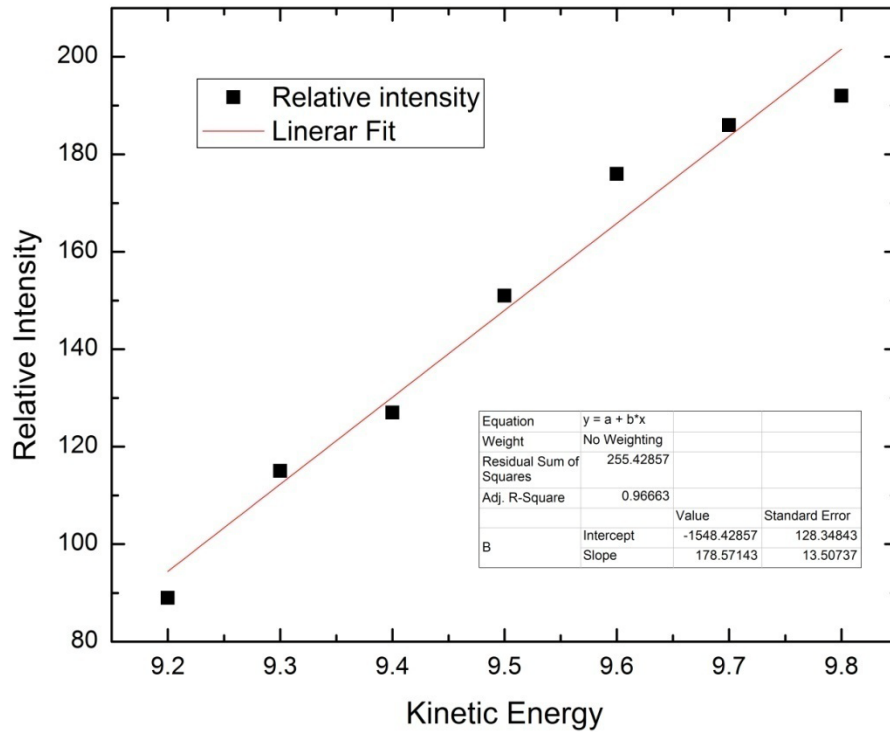
Figure 4.24. Example of fitting to determine adjustment due to charging. Data points are from middle third of conduction band edge from $Li_2B_4O_7(100)$ using the IPES system. This current spectra is from a sample oriented [010] with sample normal at 18° with respect to incident electrons.

These were adjusted against the higher angle spectra where little shift was noted. A

graph of stacked spectra was obtained for each sample for each surface direction of

interest as depicted in Figure 4.25.

89
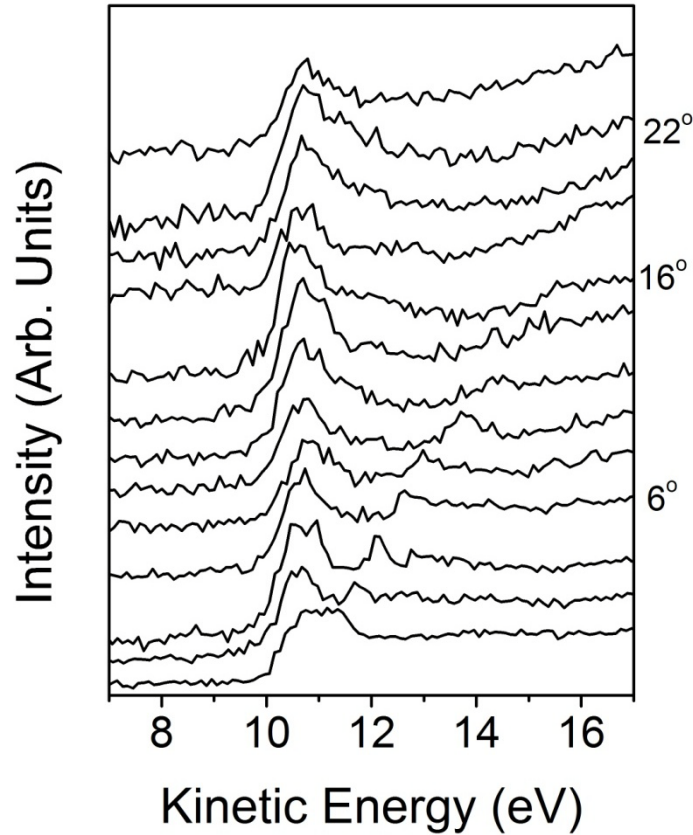
Figure 4.25. Example of conduction band adjusted stacked spectra for Li$_2$B$_4$O$_7$(110) using the IPES system. This current spectra is from a sample oriented [$\underline{1}$10] with sample normal ranging from 0° to normal at 24° in increments of 2° with respect to incident electrons.

The peak fitting using Gaussian line functions was similar as discussed for PES, as was

the determination of surface component to the wave vector. The results of both will be

displayed and discussed in detail in Chapter 7.

4.5. References

1. D. Piwowarska, S. Kaczmarek, and M. Berkoski, "Growth and characterization of pure and Co2+ doped Li$_2$B$_4$O$_7$ single crystals," Cryst. Res. Technol. **42,** 1329 (2007).

2. S. Kar and K. S. Bartwal, "Growth Optimization of Li$_2$B$_4$O$_7$ Crystals and Their Characterization," Cryst. Growth Des. **7,** 2522-2525 (2007).

90

3. The International Centre for Diffraction Data, "Database 01-084-2191," http://www.icdd.com/.

4. D. Wooten, I. Ketsman, J. Xiao, Y. B. Losovyj, J. Petrosky, J. McClory, Y. Burak, V. Adamiv, and P. A. Dowben, "Differences in the Surface Charging at the (100) and (110) Surfaces of $Li_2B_4O_7$ in *Nuclear Radiation Detection Materials — 2009*," in *Nuclear Radiation Detection Materials — 2009,* D. L. Perry, A. Burger, L. Franks, K. Yasuda, and M. Fiederle, eds. (MRS, 2009), pp. 1164-L04-04.

5. D. Wisbey, "UHV Schematic," (2008).

6. K. Kim, "Synchrotron Radiation," in *X-Ray Data Booklet,* Lawrence Berkley National Laboratory, ed. (Lawrence Berkley National Laboratory, 2001).

7. Y. Losovyj, I. Ketsman, E. Morikawa, Z. Wang, J. Tang, and P. Dowben, "Optimization of the 3m TGM beamline, at CAMD, for constant initial state spectroscopy," Nucl. Instrum. Methods Phys. Res. **A 582,** 264 (2007).

8. C. R. Brundel and A. D. Baker, *Electron Spectroscopy, Theory, Techniques, and Application*s (Academic Press, 1977).

9. OriginLab Data Analysis and Graphing Software, "OriginPro 8 Student Version," **8.0,** (2008).

10. S. Hüfner, "Introduction and Basic Principles," in *Photoelectron Spectroscopy Principles and Applications,* (Springer-Verlag, 1995), pp. 4.

11. D. Spanjaard, C. Guillot, M. -. Desjonquères, G. Tréglia, and J. Lecante, "Surface core level spectroscopy of transition metals: A new tool for the determination of their surface structure," Surf. Sci. Repts**. 5,** 1-85 (1985).

12. Kimball Physics, "ELG-2/EGPS-1022 Electron Gun and Powwer Supply System," (2007).

13. C. N. Borca, T. Komesu, and P. A. Dowben, "Comparing inverse photoemission and X-ray absorption spectroscopies," Journal of Electron Spectroscopy and Related Phenomena**, 122,** 259-273 (2002).

14. J. Xiao and P. A. Dowben, "The role of the interface on the electronic strucutre of adsorbed metal (II) (Co, Ni, Cu) phthalocyanines," J. Materials Chem**. 19,** 2172 (2009).

5. The Li Surface Core Level Shift in $Li_2B_4O_7$

5.1. Overview

In this chapter, I provide analysis of the surface core level shift for lithium at the surface of $Li_2B_4O_7(110)$ in an effort to establish a reference point for the data presented in the subsequent chapters. This data also indicates that there is a surface electronic structure at the (110) surface, which is consistent with work described later in this dissertation.

As presented in Chapter 4, there was a large photovoltaic charging problem with this particular oxide. This phenomenon can best be explained in the following manner: through the photoemission process, described in Chapter 3, an electron is freed from the neutral lithium tetraborate sample, leaving behind a charged sample. This charge is not typically very mobile within an insulator and thus photoemission will create a positive charge in the surface and near surface region of the sample where the photoemission dominates. Since these positive charges cannot easily move, this will create a Coulombic potential, or space charge, that will impact the photoelectrons moving towards the electron energy analyzer. This ultimately causes the primary spectra to be shifted deeper in binding energy away from E_{Fermi}.

By increasing the temperature, the thermal energy helps to mitigate this effect by increasing the number of charge carriers and their mobility so as to diminish the positive surface charges; or, more correctly, to provide thermal energy for electrons from deeper in the sample to move toward the few empty orbitals near the surface of the sample. This will mitigate the photovoltaic charging effect and provide spectra that are closer to the

ground state reality. This is in contrast with a typical metal where a sea of mobile electrons can easily replenish those leaving the sample. Consequently, one would not expect a charging adjustment necessary for a metallic sample. Both of these features are demonstrated by the spectra at different temperatures for $Li_2B_4O_7(110)$ and amorphous Cu in Figure 5.1.
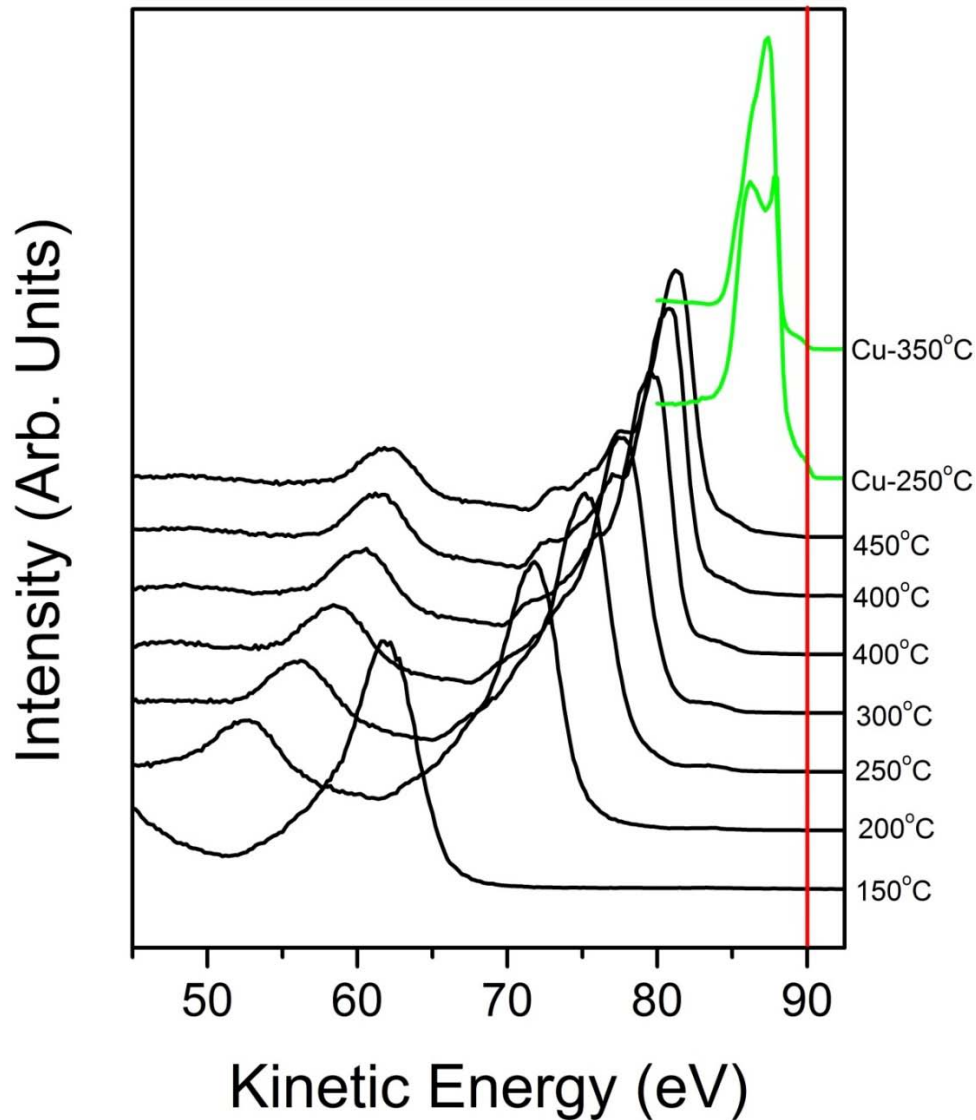
Figure 5.1. Photovoltaic charging effect on amorphous Cu (green) and $Li_2B_4O_7(110)$ (black) for various temperatures. E_{Fermi} is depicted by the red line.

In the Figure 5.1 example, E_{Fermi} is indicated by a red line and was experimentally determined via amorphous Cu or Ta. One can also see here the temperature dependent Fermi-Dirac distribution function step; the $\frac{1}{e}$ (roughly $\frac{1}{3}$) of the Fermi-cut-off function. E_{Fermi}, also known as the chemical potential, is denoted by a red line. Partially filled valence bands are characteristic of metals; in this case Cu $4s_1$ and a physical location where one can identify E_{Fermi}, which has been done here. Although the density of states changes for the Cu example with the increase in temperature, E_{Fermi} remains the same, as expected, for this metal.

Unfortunately, this effect could not be completely negated in the lithium tetraborate sample by simply increasing the temperature without destroying the crystal integrity. Consequently, a good reference point was needed from which all spectra could be adjusted for this effect.

Although O 2s was the nearest shallow core energy level to the valence band, this was used as one of two primary reference points. But due to its very closeness to the valence band, and because this is an oxygen core, there are complications possible from surface defects and states; and was therefore less desirable in this case as a reference point. Consequently, the next deeper energy level, Li 1s, was selected. As a much deeper energy level, the valence band contribution would be negligible. Following the sequence discussed in Chapter 4 to theoretically determine distance from E_{Fermi}, an absolute, theoretical limit for charging was determined.

Through a literature review, it was also found that there existed previously published values for the binding energies to include that of Li 1s within lithium tetraborate [1]. Implicitly trusting this source without verification was considered too

94

risky. What will be presented in this chapter justifies that concern. A different value for the Li 1s bulk core level will be presented along with what was determined as the most reasonable culprit for this difference, that is, not properly accounting for an observable surface to core level shift for lithium at the surface of lithium tetraborate.

5.2. Surface-To-Bulk Core Level Shift Background

The study of surface-to-bulk core level shifts has a long and rich history [2, 3] and from the outset has been given considerable theoretical support [4-8]. Application of the technique to alkali-metal-containing compounds, in particular dielectric compounds should yield very large surface-to-bulk core level binding energy shifts. Surface-to-bulk core level shifts have been observed for oxides [9], but with only a few examples that have incorporated the alkali metals, particularly lithium [10, 11]. With alkali metals, the concept of multiple valences cannot apply so that any observation of a surface-to-bulk core level shift would suggest the presence of a surface electronic structure far different from the bulk.

For the oxides like the lithium borates, surface termination should lead to a very different oxygen coordination of the alkali metal. Yet there are few, if any, reports of a surface-to-bulk core level shift for lithium in such oxide compounds [10], or even for the tungsten and molybdenum bronzes, the latter being quasi-one dimensional materials based on lithium or alkali metal chains [11].

5.3. Why Choose $Li_2B_4O_7(110)$ and Not $Li_2B_4O_7(100)$?

Obviously both polar and non-polar surfaces can exist at various possible oxide compound surfaces, but polar surfaces tend to be less stable and more susceptible to

95

surface reconstructions. The various possible oxide surface terminations should exhibit

surface-to-bulk core level shifts, although the extent of the surface-to-bulk core level shift

may vary widely. Surface reconstructions, as well as major surface lattice relaxations can

complicate the observed surface-to-bulk core level shift [2]. We have chosen to

demonstrate the existence of a Li 1s surface-to-bulk core level shift for lithium

tetraborate, $Li_2B_4O_7(110)$. The (110) surface termination is shown to have a largely

non-polar surface termination as discussed later in this chapter and in Chapter 7 [12, 13].

The bulk core value should be the same, regardless.

5.4. Differentiating the Surface from Bulk

Most of the specific experimental procedures, along with the adjustments

necessary for charging have already been addressed in detail in the section on angle

resolved photoemission spectroscopy within Chapter 4. Consequently only the highlights

and exceptions will be covered in here.

In order to differentiate between surface and bulk components of the Li 1s core,

the photoelectron emission angle was varied, as has become the standard [2] and

historical [3] practice. In summary, the standard technique relevant here is to change the

angle off of normal [2], thereby electrons are collected that have a decreased effective

mean free path (λ) in the direction along that normal to the surface, as depicted in

Figure 5.2.
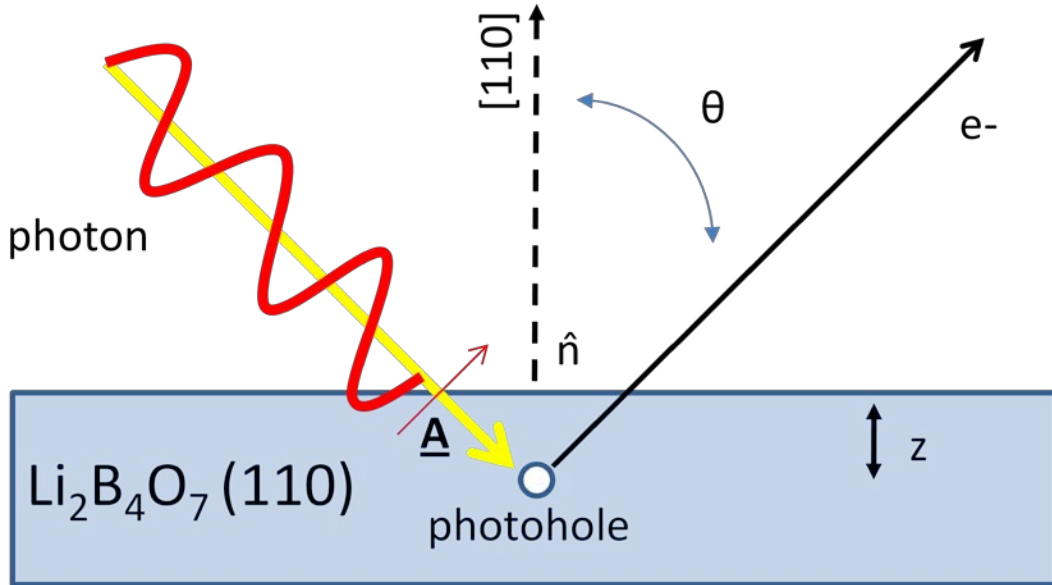
Figure 5.2. Standard experimental technique using angle resolved photoemission spectroscopy on $Li_2B_4O_7(110)$ as discussed by Spanjaard et al [2] as well as pictorial representation of the Beer-Lambert Law.

What is represented in Figure 5.2 is also mathematically described by the Beer-Lambert Law, which suggests that the greater the off normal emission angle (θ), the less bulk intensity (I_{bulk}) one can expect to see:

$$I_{bulk} = I_o exp(-z/\lambda cos\theta) \tag{50}$$

I_o and z are the intensity at the surface and the perpendicular depth from the sample surface, respectively. Consequently, a spectral feature that is surface dependent should be enhanced if one biases the analyzer by changing its acceptance angle to count those electrons that originate at or near the surface. In other words, it is a reasonable expectation to observe an increase in the relative intensity of the surface component of the core level with an increase in emission angle. This is based on prior studies of surface-to-bulk core level shifts [2, 3].

97

There is an alternate PES technique that could also be used to observe if a spectral feature was indeed tied to the surface. If a spectral feature were to decrease with increasing photon energy at the same crystal orientation, off normal angle and temperature, this would also lead to the conclusion that the feature was tied to the surface electronic structure. As the photon energy was increased, the penetration depth of the sample was increased. Consequently, the relative intensity contribution to the bulk as compared to the surface component would increase whereas the relative surface contribution should decrease.

5.5. The Li 1s Surface-To-Bulk Core Level Shift

The Li 1s core level photoemission feature, as shown in Figure 5.3, was identified through the use of angle resolved photoemission spectra taken from $Li_2B_4O_7(110)$ with **E** oriented along [001] and at a photon energy of 95 eV.
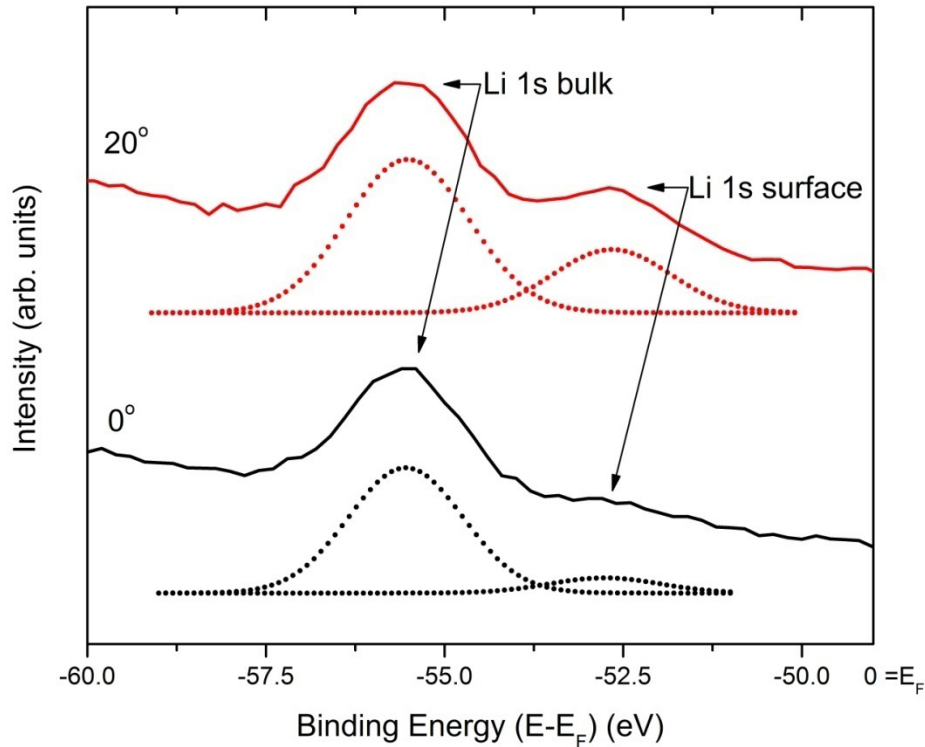
Figure 5.3. Angle-resolved photoemission spectra of $Li_2B_4O_7(110)$ in the region of the Li 1s core level, for photoelectron emission angles of 20° and 0°. In both cases, the in-plane component of <u>E</u> was oriented along [001] with a light incidence angle 45 degrees and with photon energy of 95 eV. The figure shows spectra with the instrumental background and secondary electron tail subtracted from the spectra with fittings to the Li 1s bulk and surface peaks. The sample temperature for these measurements was 623 ± 5 K, to reduce surface charging.

After corrections for photovoltaic charging (as discussed above and elsewhere [12]), we place the Li 1s shallow core level binding energies at -56.7 ± 0.4 to -56.5 ± 0.4 eV depending on the surface termination (crystal orientation), but these values are largely dominated by the bulk Li 1s core level binding energy because of the normal photoelectron emission geometry. By increasing the electron emission angle, two components can be easily resolved for the $Li_2B_4O_7(110)$ surface at -56.5 ± 0.4 eV and -53.7 ± 0.5 eV, as illustrated in Figure 5.3.

99

The intensity of the Li 1s core level component for the $Li_2B_4O_7(110)$ surface at the smaller binding energy of -53.7±0.5 eV is shown to increase with increasing emission angle and thus we assign this Li 1s component at this binding energy as the surface component. The feature at a higher binding energy of -56.5±0.4 eV is attributed to the Li 1s bulk component for $Li_2B_4O_7(110)$.

The binding energy for the bulk Li 1s component (-56.5±0.4 eV) tends to be somewhat higher than reported previously for lithium tetraborate $Li_2B_4O_7$ [1] at -55.7 eV. Without adequate preparation of the stoichiometric clean surface, there is reason to believe that surface contributions (with a core level binding energy of -53.7±0.5 eV) will dominate even the core level photoemission spectra and lead to an artificial decrease in the core level binding energies that might otherwise be attributed solely to the bulk of lithium tetraborate and similar compounds. No surface component was reported for the Li 1s core in that prior study [1].

The photoemission spectra was deconvoluted in the manner discussed in Chapter 4, in the region of the Li 1s shallow core for both 0° and 20° photoelectron emission angles, as shown in Figure 5.3. Any components other than those observed and attributed to the Li 1s surface-to-bulk core level shift do not appear to be significant, after the instrumental background spectra and secondary electron tail spectra have been subtracted, as indicated in Figure 5.3. There is no component of the Li 1s that provides a significant contribution to the photoemission in this binding energy region beyond those two components that can be assigned to the Li 1s surface and bulk core level components.

The observed large binding energy separation between the surface and bulk components of the Li 1s core suggest the surface electronic structure of lithium tetraborate $Li_2B_4O_7(110)$ may differ significantly from the bulk.

Aside from the positive results following standard practices indicating the presence of a surface-to-bulk core level shift, there also exists corroborating evidence that support this. These will be addressed in the following sections.

5.6. Light Polarization-Dependent Evidence

Within the angle resolved photoemission, there is evidence for states within the valence band maximum to conduction band minimum gap (the insulator band gap), as shown in Figure 5.4 and denoted by "S".
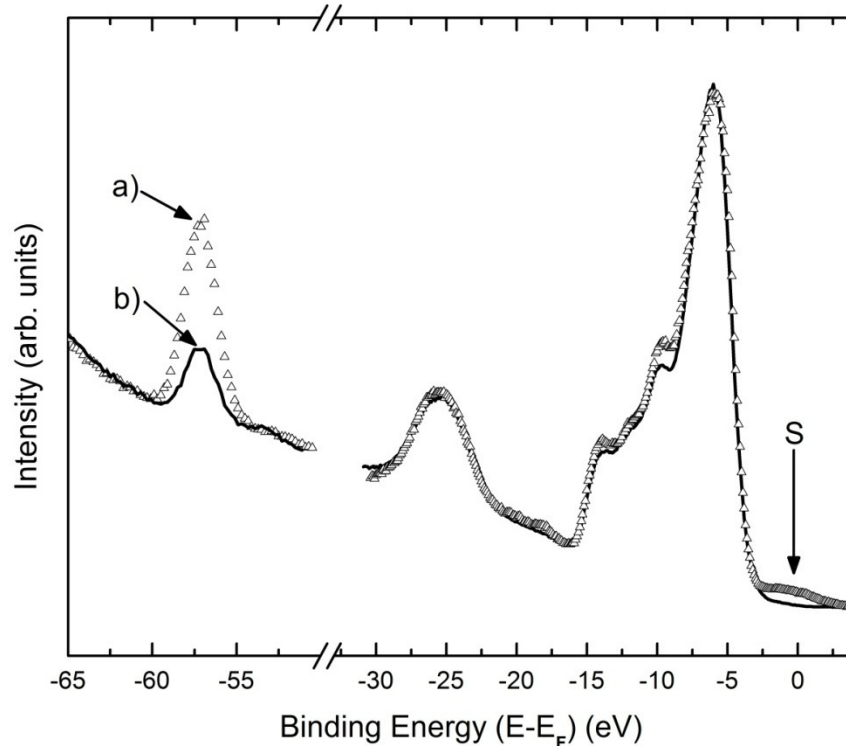
Figure 5.4. Experimental light polarization dependent photoemission spectra for Li$_2$B$_4$O$_7$(110) oriented along [001] with regards to the in-plane component of <u>E</u>. The photon energy is 95 eV with the photoelectrons collected along the surface normal; the light incidence angle was (a) 70 degrees {△ △ △} or (b) 45 degrees {——} with respect to surface normal. The arrow indicates the position of a surface state contribution (S) to the occupied density of states above the bulk density of states valence band maximum.

The light polarization dependent photoemission in the valence band region of the

Li$_2$B$_4$O$_7$(110) surface exhibits few differences between a light incidence angle of 70°,

placing the electric vector **<u>E</u>** more along the surface normal and a light incidence angle of

45°. The enhancement of the Li 1s along with other spectral features will be addressed in

detail in Chapter 7. A clear surface state is evident on the (110) surface. However, one

does not observe the same surface state in the light polarization dependent photoemission

spectra for (100). The absence of differences in the light polarization dependent

102

photoemission of the lithium tetraborate valence band region is consistent with the characterization of $Li_2B_4O_7(110)$ as a largely non-polar surface.

The cause of this is the weak surface component within the band gap(s) in the photoelectrons being collected along the surface normal as in Figure 5.3. Contributions, though, from the surface electronic structure are to be expected. What is of interest here is the presence of a surface state on a very clean sample surface. As these states fall into the gap of the projected bulk band structure, as will be discussed in Chapter 6, we can initially conclude these are in fact surface states. The observed intensity of these surface states are clearly affected by light polarization in photoemission and are likely of s or p_z character given that they are enhanced with incident light where the electric vector **E** is more along the surface normal.

These states within the gap do not appear to be the result of surface defects. The states shown at binding energies in photoemission above the valence band maximum, close to the Fermi level, are shown for one incident light polarization but not the other (Figure 5.4). This light polarization dependent photoemission would be very unusual for surface defects; and it can reasonably be surmised that this is additional evidence for a surface electronic structure differing from that of the bulk.

5.7. IPES Collateral Evidence for Surface State

The same $Li_2B_4O_7(110)$ surface was also characterized, via inverse photoemission, as having a k-vector-dependent, strongly dispersing image potential state as indicated by Figure 5.5.

103
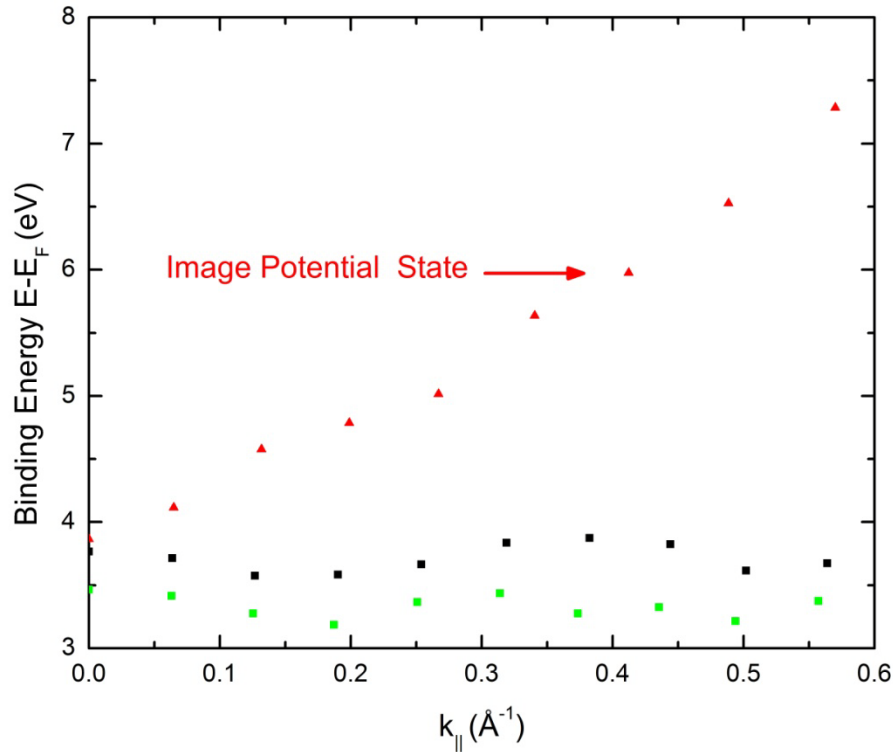
Figure 5.5. Evidence of presence of an image potential state within Li₂B₄O₇(110), with E aligned along [001]. Theoretical Brillouin Zone equals 0.23 Å⁻¹. Surface sample is normal with respect to electron gun and temperature is 293 °C.

Most of the details of this feature will be discussed further in Chapter 7. What is important here—as indicated by Figure 5.5—is the clear presence of a non-Brillouin Zone-repeating, parabolic feature, known as an image potential state [14]. Observation of such an image potential state would not be likely if the surface contained even a small number of surface defects. Image potential (Rydberg-like) states are typically suppressed by surface defects and the dispersion of the image potential states is strongly suppressed by surface defects [14]. This further supports our earlier assertion of a relatively defect-free surface, and hence enhances the determination of a differing surface electronic structure from that of bulk.

104

5.8. Concluding Remarks

For the $Li_2B_4O_7(110)$ surface, a very large surface-to-bulk core level shift, slightly less than 3 eV, has been observed for the Li 1s shallow core; which is also the most likely culprit for previously reported undervalued Li 1s energies [1]. The large Li 1s surface-to-bulk core level shift suggests there is a surface electronic structure for $Li_2B_4O_7(110)$. This contention is supported by the valence band photoemission where states within the band gap of the projected bulk density of states are observed in the region of the Fermi level. The observed photoemission states fall into the gap between the valence band and conduction band edges. These states shown in the light polarization dependent photoemission which is further supported by inverse photoemission results are consistent with surface states and indeed no other assignment appears possible. The correct assignment of the Li 1s core level binding energies must take into account the different binding energies of the surface and bulk contributions for lithium tetraborate and other related compounds. Consequently, rather than using previously published results, the values determined in this section were as the initial reference point in this research.

5.9. References

1. A. Y. Kuznetsov, A. V. Kruzhalov, I. N. Ogorodnikov, A. B. Sobolev, and L. I. Isaenko, "Electronic structure of lithium tetraborate $Li_2B_4O_7$ crystals. Cluster calculations and x-ray photoelectron spectroscopy," Phys. Solid State **41,** 48 (1999).

2. D. Spanjaard, C. Guillot, M. -. Desjonquères, G. Tréglia, and J. Lecante, "Surface core level spectroscopy of transition metals: A new tool for the determination of their surface structure," Surf. Sci. Repts. **5,** 1-85 (1985).

3. P. H. Cirtrin, G. K. Wertheim, and Y. Baer, "Core-Level Binding Energy and Density of States from the Surface Atoms of Gold," Phys. Rev. Lett. **41,** 1425 (1978).

4. J. A. Appelbaum and D. R. Hamann, "Electronic structure of the Cu(111) surface," Solid State Commun. **27,** 881-883 (1978).

5. B. Johansson and N. Mårtensson, "Core-level binding-energy shifts for the metallic elements," Phys. Rev. B **21,** 4427-4457 (1980).

6. A. Rosengren and B. Johansson, "Calculated transition-metal surface core-level binding-energy shifts," Phys. Rev. B **22,** 3706-3709 (1980).

7. P. J. Feibelman, J. A. Appelbaum, and D. R. Hamann, "Electronic structure of a Ti(0001) film," Physical Review B **20,** 1433 (1979).

8. P. J. Feibelman and D. R. Hamann, "Surface States of Sc(0001) and Ti(0001)," Solid State Commun. **31,** 413-417 (1979).

9. J. Zhang, P. A. Dowben, D. Li, and M. Onellion, "Angle-resolved photoemission study of oxygen chemisorption on Gd(0001)," Surf. Sci. **329,** 177 (1995).

10. A. Kuznetsov, A. Kruzhalov, I. Ogorodnikov, A. Sobolev, and L. Isaenko, "Electronic structure of lithium tetraborate $Li_2B_4O_7$ crystals. Cluster calculations and x-ray photoelectron spectroscopy," Physics of the Solid State **41,** 48-50 (1999).

11. K. Smith, *Private communication to P. A. Dowben* (, 2009).

12. D. Wooten, I. Ketsman, J. Xiao, Y. B. Losovyj, J. Petrosky, J. McClory, Y. Burak, V. Adamiv, and P. A. Dowben, "Differences in the Surface Charging at the (100) and (110) Surfaces of $Li_2B_4O_7$ in *Nuclear Radiation Detection Materials — 2009,*" in *Nuclear Radiation Detection Materials — 2009,* D. L. Perry, A. Burger, L. Franks, K. Yasuda, and M. Fiederle, eds. (MRS, 2009), pp. 1164-L04-04.

13. D. Wooten, I. Ketsman, J. Xiao, Y. B. Losovyj, J. Petrosky, J. McClory, Y. V. Burak, V. T. Adamiv, R. Hengehold, and P. A. Dowben, "Electronic Structure of $Li_2B_4O_7$(110) and $Li_2B_4O_7$(100) (in preparation)," (2009).

14. N. V. Smith, "Inverse Photoemission," Rept. Prog. Phys. **51,** 1227-1294 (1988).

6. Lithium Tetraborate (110) and (100) Experimental Band Gap

6.1. Overview

In this chapter, the combined experimental results from angle resolved photoemission and inverse photoemission spectroscopy is presented. Valence to conduction band gap estimates will be provided for both surfaces along two high symmetry directions; along with an overall analysis of the results. A more detailed discussion regarding the occupied and unoccupied states will be dealt with in subsequent chapters.

6.2. $Li_2B_4O_7(110)$ and $Li_2B_4O_7(100)$ Valence to Conduction Band Gaps

Following the procedures, as discussed in Chapter 4 and elsewhere [1], the valence to conduction band gaps were determined along two high symmetry directions, both the $Li_2B_4O_7(100)$ and $Li_2B_4O_7(110)$ directions as displayed in Figure 6.1 (inset). Both $Li_2B_4O_7(100)$ and $Li_2B_4O_7(110)$ exhibit a density of states in the vicinity of the valence band maximum and conduction band minimum, as shown in Figure 6.1(b-e) that qualitatively agrees with the results from model bulk band structure calculations for $Li_2B_4O_7$ [2, 3], as shown in Figure 6.1(a).
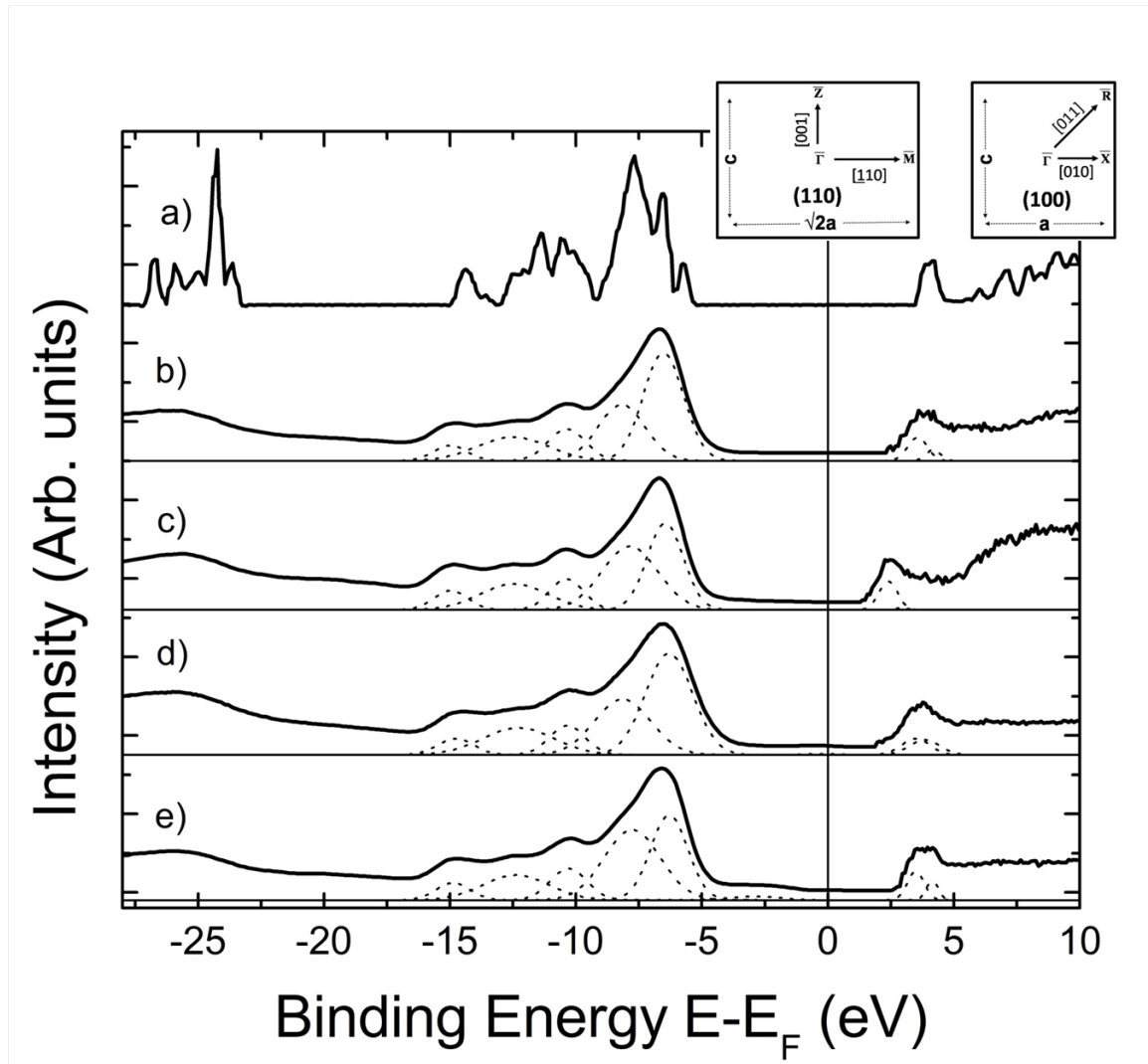
Figure 6.1. (a) The theoretical density of states of solid $Li_2B_4O_7$, as published by Islam et al. [2]. (b) The combined experimental photoemission, inverse photoemission results for $Li_2B_4O_7(100)$ with $\underline{E}$ oriented along [011]; (c) oriented along [010] (d) $Li_2B_4O_7(110)$ oriented along [001]; and (e) oriented along [$\underline{1}$10]. The specific features are highlighted as indicated by their respective deconvolution. (Inset) Schematic of both the Li2B4O7(100) and Li2B4O7(110) surfaces investigated here, depicting the four directions used in the band mapping studies and denoting the real space lattice but with the labels for the Brillouin zone critical points included.

For $Li_2B_4O_7(100)$ the band gaps obtained from combined photoemission and inverse photoemission are 10.1 ± 0.5 eV and 8.9 ± 0.5 eV in the [011] and [010] orientations, respectively. For $Li_2B_4O_7(110)$, the band gaps are 9.8 ± 0.5 eV in both the [001] and [$\underline{1}$10] orientations.

6.3. Discussion

In general, the combined photoemission and inverse photoemission measures the direct band gap, but as final state spectroscopies as opposed to initial state spectroscopies. It is worth recalling from Chapter 3 and elsewhere [4], that deducing band structure from the experimental measurement of photoemitted electrons as they are captured in their final state by the analyzer cannot perfectly correlate with their actual initial state as they truly exist in the solid prior to their interaction with a photon. Consequently, perfect agreement with a ground state calculation, such as density functional theory, is generally not possible and unlikely. However, the agreement as shown here between experiment and the prior band structure calculations [2] is surprisingly quite good considering that DFT usually obtains a band gap too small for most semiconductors.

After adjusting for charging as discussed in Chapter 4, a few general assertions can be made. First, the experimental band gaps for these two $Li_2B_4O_7$ surfaces are indeed large, as expected [2]. Doping will be required to be useful in any realistic device. The Fermi level is placed slightly closer to the conduction band edge in the combined experimental photoemission and inverse photoemission spectra, as shown in Figure 6.1. This indicates that both the $Li_2B_4O_7(100)$ and $Li_2B_4O_7(110)$ surfaces are n-type, although (100) is more n-type than (110). While we have not measured the majority

109

carrier, the Fermi level placement is consistent with the known bulk properties where the majority of defects shown in these $Li_2B_4O_7(100)$ and $Li_2B_4O_7(110)$ were oxygen vacancies [5].

6.4. Concluding Remarks

Experimental results indicated that the bulk valence to conduction band gap ranged from 8.9 to 10.1 eV; with the most consistent surface being the $Li_2B_4O_7(110)$. Along the two orthogonal directions, the band gaps at this surface were within 0.01 eV of each other.

What is vital to this research effort is that $Li_2B_4O_7(110)$ is the less polar, more stable surface, as compared to $Li_2B_4O_7(100)$. Assuming one can fabricate contacts from the former, $Li_2B_4O_7(110)$ would be the best choice from the two for potential inclusion in a solid state neutron detector, although making an ohmic contact may be easier with the more defective surface.

6.5. References

1. D. Wooten, I. Ketsman, J. Xiao, Y. B. Losovyj, J. Petrosky, J. McClory, Y. V. Burak, V. T. Adamiv, R. Hengehold, and P. A. Dowben, "Electronic Structure of $Li_2B_4O_7(110)$ and $Li_2B_4O_7(100)$" (2009), in press.

2. M. M. Islam, V. V. Maslyuk, T. Bredow, and C. Minot, "Structural and Electronic Properties of $Li_2B_4O_7$," J. Phys. Chem. B **109,** 13597-13604 (2005).

3. V. T. Adamiv, Y. B. Burak, I. V. Kityk, J. Kasperczyk, R. Smok, and M. Czerwinski, "Nonlinear optical properties of $Li_2B_4O_7$ single crystals doped with potassium and silver," Opt. Mater. **8,** 207-213 (1997).

4. S. Hüfner, "Photoemision of Valence Electrons from Metallic Solids," in *Photoelectron Spectroscopy Principles and Applications,* (Springer-Verlag, 1995), pp. 348.

5. M. W. Swinney, J. W. McClory, J. C. Petrosky, Y. V. Burak, S. Yang, A. T. Brant, and L. E. Halliburton, "Identification of electron and hole traps in lithium tetraborate ($Li_2B_4O_7$) crystals: Oxygen vacancies and lithium vacancies," Journal of Applied Physics (2010), in press.

7. The Occupied States of Lithium Tetraborate (110) and (100)

7.1. Overview

In this chapter, an overview of the band structure and origin of the spectral weight density (experimental) of the $Li_2B_4O_7(100)$ and $Li_2B_4O_7(110)$ occupied states is provided. This includes both surface and bulk band structure features below E_{Fermi}. Additionally, energy dependent resonant features and observed surface states are discussed.

7.2. ARPES Binding Energy versus Relative Intensity

Both the $Li_2B_4O_7(100)$ and $Li_2B_4O_7(110)$ surfaces presented five experimentally repeatable, observable surface energy states within the valence band using ARPES as discussed in Chapter 4. Within the $Li_2B_4O_7(110)$ surface an additional energy state was observed between the valence band edge and E_{Fermi}; which will be addressed in detail in a subsequent section. Figure 7.1 presents a sample of some of the angle-resolve photoemission results for both surfaces in each of the high symmetry directions.

112
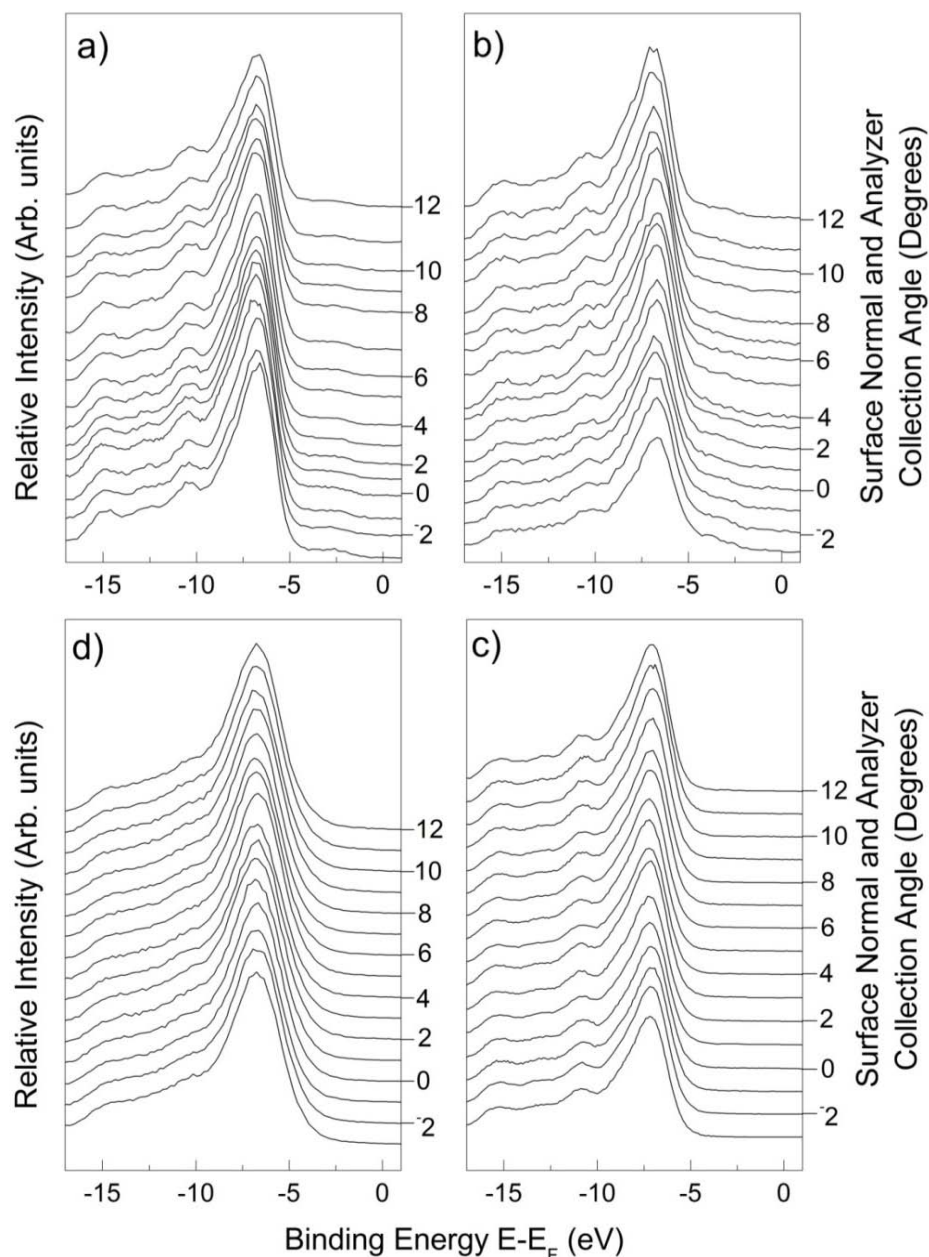
Figure 7.1. The emission angle dependent photoemission spectra for the $Li_2B_4O_7(110)$ taken with increasing wave vector (emission angle) along the a) [$\underline{1}$10] and b) [001] directions; as well as $Li_2B_4O_7(100)$ taken with increasing wave vector (emission angle) along the c) [011] and d) [010] directions. The light incidence angle was 45 degrees and the spectra were taken with photon energy of 56 eV for Figures a-c, and 70 eV for Figure d. The occupied state binding energies are given in terms of $E-E_F$.

113

7.3. Li$_2$B$_4$O$_7$(100) and Li$_2$B$_4$O$_7$(110) Binding Energy versus $k_\parallel$

Both the Li$_2$B$_4$O$_7$(110) and Li$_2$B$_4$O$_7$(100) surfaces exhibit equally little valence band dispersion and are very flat with respect to potential. The surface parallel wave vector component ($k_\parallel$) was determined along the high symmetry directions of each of the two surfaces. As discussed and demonstrated in detail in Chapters 3 and 4, the parallel momentum ($k_\parallel$) can be derived as follows from the photoelectron kinetic energy and the emission angle (θ) with respect to the surface normal [1-3]:

$$k_\parallel = \sqrt{\frac{2mE_{kin}}{\hbar^2}} \sin(\theta) = 0.512 \text{Å}^{-1} \sqrt{\frac{E_{kin}}{eV}} \sin(\theta) \tag{51}$$

The results for the Li$_2$B$_4$O$_7$(110) and Li$_2$B$_4$O$_7$(110) surfaces, obtained from the emission angle dependent photoemission spectra may be plotted as a function of wave vector $k_\parallel$, as shown in Figures 7.2(a-d). There is so little dispersion within both Li$_2$B$_4$O$_7$(110) and Li$_2$B$_4$O$_7$(100) unoccupied states, it is very difficult to resolve the theoretical periodicity within the intrinsic experimental uncertainty (± 0.05 to ± 0.1 eV) as one moves across Brillouin zones. It should be pointed out that four different energies (70 eV, 56 eV, 45 eV and 40 eV) were used, with similar outcomes, with characteristic results depicted by the spectra taken with a photon energy of 56 eV. For the two lower energies it was difficult to resolve a reference O2s peak due to an overwhelming secondary electron tail. In addition, a broken low energy grating in the beamline did not allow time to conduct additional synchrotron runs to ensure repeatable results at these lower energies. Therefore, to ensure repeatable results are presented, those with the higher energy values will be presented here.

114
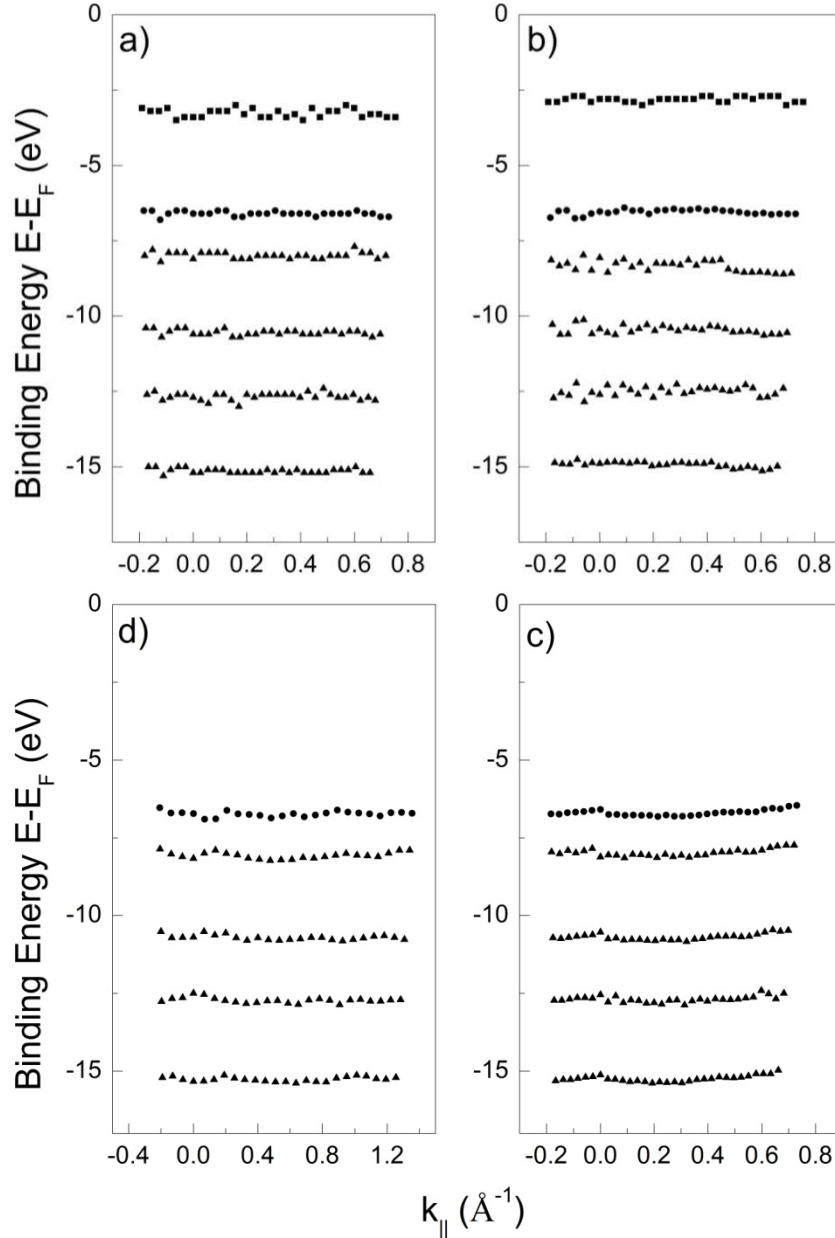
Figure 7.2. The binding energies versus the parallel component of wave vector ($k_{\parallel}$) for the occupied valence states. For $Li_2B_4O_7(110)$, the in-plane component of the incident light $\underline{E}$ is oriented along a) [$\underline{1}$10] and, b) [001]; and for $Li_2B_4O_7(100)$ it is oriented along c) [011] and d) [010]. The light incidence angle was 45 degrees, with the photoelectrons collected by a hemispherical analyzer oriented at angles ranging from -3 to 20 degrees along the surface normal. The temperature was 625±5 K. Figures a-c were derived from spectra with a photon energy equal to 56 eV, while figure d was derived from spectra with photon energy equal to 70 eV. ■ denotes a surface state, ● denotes HOMO or valence band maximum, and ▲ denotes surface state located within the valence band. (Theoretical Brillion zone dimensions are (a-d): 0.234 Å^{-1}, 0.305 Å^{-1}, 0.225 Å^{-1}, and 0.331 Å^{-1})

115

7.4. Hole Effective Mass Estimation

The periodic wave vector dependence of shallow core levels has been observed for oxides with large real space unit cells, and thus small Brillouin zones, as in the case of monoclinic Gd_2O_3(-402) [4]. The absence of any such dispersion in this borate suggests that the occupied states for both the $Li_2B_4O_7$(110) and $Li_2B_4O_7$(100) surfaces have a very heavy mass. From the absence of dispersion in the photoemission data (Figure 7.1 and 7.2), we can assign a lower bound to the hole effective mass for the Highest Occupied Molecular Orbital (HOMO) using the following:

$$m^*_{HOMO} \cong \left(\frac{\hbar^2}{2\Delta E_{kin}} \right) (\Delta k)^2; \tag{52}$$

where $\Delta E_{kin}, \Delta k, m^*_{HOMO}, m_e$ and $\hbar$ are the change in kinetic energy values between extremes in the Brillouin zone, the change in parallel component of the wave vector between extremes in the same Brillouin zone, lower bound value to the HOMO effective mass, the electron rest mass and Dirac's constant, respectively. The resulting m^*_{HOMO} values range from 10.8 to 14.2 [m*/m_e] for $Li_2B_4O_7$(110) and $Li_2B_4O_7$(100). As the lower bound is limited by the feature widths in photoemission and the limited wave vector and energy resolution, this value suggests a very heavy hole or occupied band state mass for both the $Li_2B_4O_7$(110) and $Li_2B_4O_7$(100) surfaces, consistent with the DFT band structure calculations [5].

7.5. Light Polarized Dependent Photoemission Results

From Figures 7.3 and 5.4, it is clear that the light polarization dependent photoemission differs for $Li_2B_4O_7$(100) and $Li_2B_4O_7$(110). The valence band density of

states, as indicated by the angle-resolved photoemission, is strongly enhanced for Li$_2$B$_4$O$_7$(100), with incident light polarization placing the electric vector **E** more along the surface normal (Figure 7.3(d)). This is not the case for Li$_2$B$_4$O$_7$(110), where there is little influence of incident light polarization on the angle resolved photoemission (Figure 7.3a), except for the Li 1s shallow core as is generally expected for an Li 1s shallow core with a strong surface contribution (Figure 5.4). In Figure 7.3(b), along the non-polar face (110) with **E** along [$\underline{1}$10] there is an enhancement from the s-polarized light. This leads to the conclusion that there is a band weighting of 2p$_x$ ± 2p$_y$, most likely from boron and oxygen. Within the (100) face, Figure 7.3(c) leads to the conclusion that there is still a slight enhancement towards 2p$_z$ weighted bands, albeit not to the degree measured with **E** along [010].

117
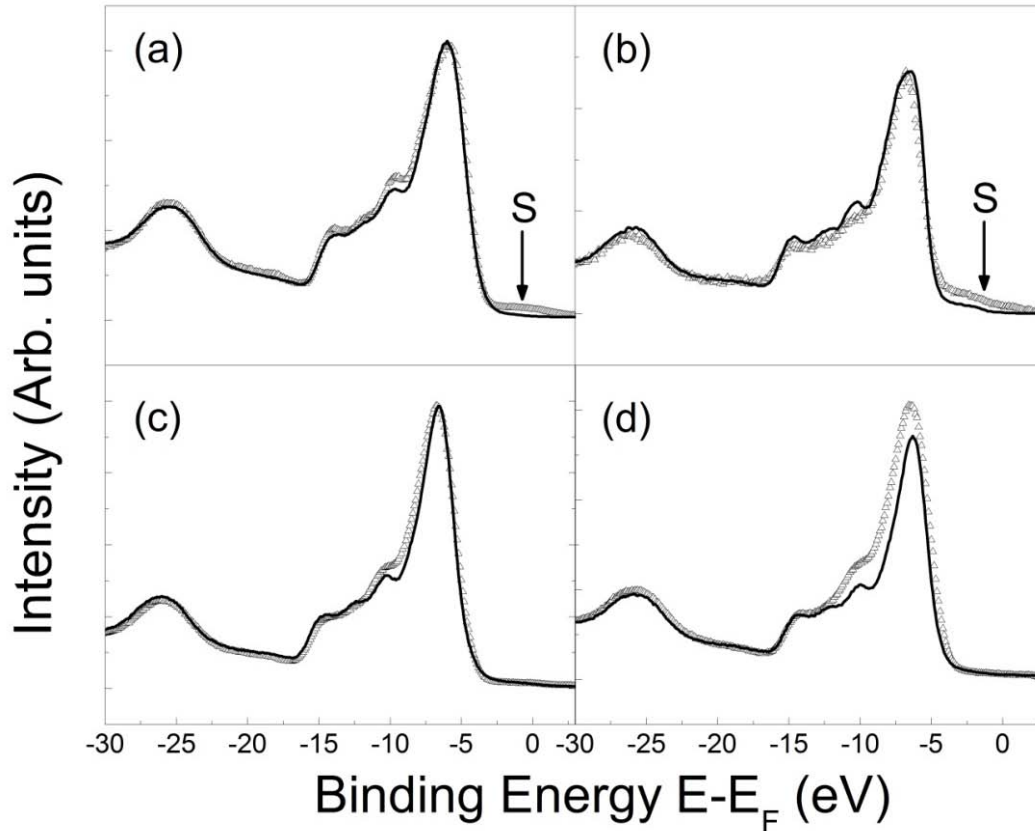
Figure 7.3. The light polarization dependent photoemission spectra for the $Li_2B_4O_7(110)$ (a, b) and $Li_2B_4O_7(100)$ (c, d) surfaces. The in-plane component of the incident light $\underline{E}$ for photoemission from $Li_2B_4O_7(110)$ oriented along [001] (a) or [$\underline{1}$10] (b). For $Li_2B_4O_7(100)$, the incident light $\underline{E}$ for photoemission was oriented along [011] (c) or [010] (d). The orientation of light incidence angle was either 70 degrees {-Δ-Δ-Δ-} or 45 degrees {—} with respect to surface normal and the spectra were taken with a photon energy of 70 eV with the photoelectrons collected along the surface normal. The (S) denotes a surface state. The occupied state binding energies are given in terms of E-E$_F$.

The general enhancement of the photoemission spectra for $Li_2B_4O_7(100)$, with the electric vector $\underline{\mathbf{E}}$ of the incident light polarization placed more along the surface normal, is indicative of a polar termination for this surface. The surface dipoles of the A_1 irreducible representation are placed along the surface normal, while for $Li_2B_4O_7(110)$, these surface dipoles must lie more in the plane of the surface. From the comparison with theory [5], the photoemission must be largely dominated in the valence band region by

118

boron and oxygen 2p weighted bands. So these surface dipoles for $Li_2B_4O_7(100)$ are related to the oxygen and boron p_z weighted bands [5].

7.6. Surface States within the Gap of the Projected Bulk Band Structure

As indicated from Figures 7.2, 7.3, 7.4 and 5.4 there is an additional state that appears with the band gap in $Li_2B_4O_7(110)$ that is not present within the $Li_2B_4O_7(100)$ surface . States that appear within the band gap are states not predicted by theory [5]. The detailed photoemission spectrum of this "gap" state is displayed in Figure 7.4.
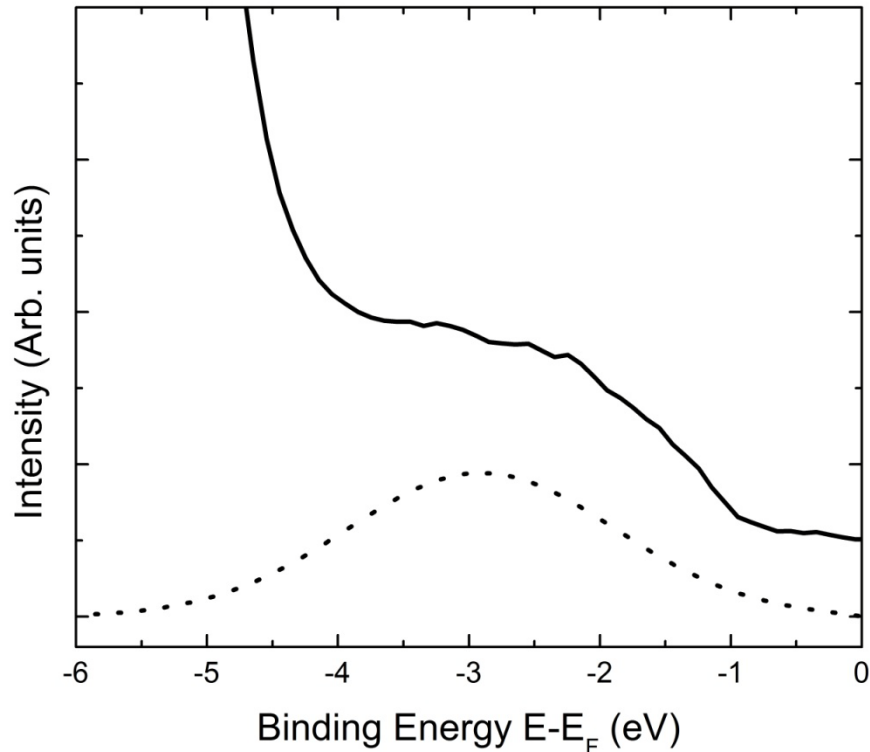
Figure 7.4. The angle resolved photoemission spectrum (ARPES) (—) for the $Li_2B_4O_7(110)$ surface illustrating the presence of an occupied surface state within the gap of the projected bulk band structure. The component (---) that does not include contributions from the valence band maximum or background is also shown. The spectrum was taken at a photon energy of 56 eV, with a light incidence angle of 45 degrees with respect to sample surface normal and the in-plane component of the incident light $\underline{E}$ oriented along the [001] direction. The occupied state binding energies are given in terms of E-E_F.

119

Corroborating evidence from light polarization dependent spectra observed in the photoemission spectra taken for both the $Li_2B_4O_7(100)$ and $Li_2B_4O_7(110)$ surfaces also supports this as a possible surface state. As shown in Figure 7.3(a) and (b), the light polarization dependent photoemission in the valence band region of the $Li_2B_4O_7(110)$ surface exhibits few differences between a light incidence angle of 70°, placing the electric vector **E** more along the surface normal and a light incidence angle of 45°. Yet with a light incidence angle of 70° there is a greater density of states within the known band gap indicating a state exists that is placed close to the Fermi level. This region, with the presence of a surface state located within the bulk band gap and below E_F, has been marked by an "S" in Figure 7.3. In other words, by increasing the incident angle of the linearly polarized light, an A_1 symmetry feature is enhanced compared to bulk denied features.

This is a true surface state for four reasons. First, after correcting for charging, there exists clear evidence of a density of states centered approximately 3 eV below E_F and 1 eV above the top edge of the valence band; a location not easily ascribed to any bulk transition [5]. Second, as discussed in detail above, the light polarization photoemission data exhibited an enhancement with increased surface normal and light incidence angle. Third, during energy dependent photoemission, the findings to be discussed in a subsequent section, there is no apparent change in peak location with differences of incident photon energy. This is in contrast to that shown with ARPES data. This is consistent with a feature having the characteristic of a surface state. Namely, one would expect a true surface state to have wave vector dependence in the parallel direction only. Finally, this state is surface sensitive, as shown in Figure 7.2(a-b)

120

for (110), so is difficult to ascribe it to a bulk state. This state exhibits the expected behavior: as displayed in Figures 7.6(a), (d), 7.10 and 7.11, the surface feature contribution in photoemission will generally decrease relative to the bulk contribution with increasing photon energy. This observed surface state feature meets these criteria in both crystal directions for the (110) surface.

The existence of these energy states would not be possible within a theoretically infinite crystal, an often used theoretical construct. However, with the modifications to the electronic wave functions necessary to meet the boundary conditions of a "semi-infinite", real crystal, real surface states are observable as displayed in Figure 7.3 and Figure 7.4 and depicted theoretically in Figure 7.5.
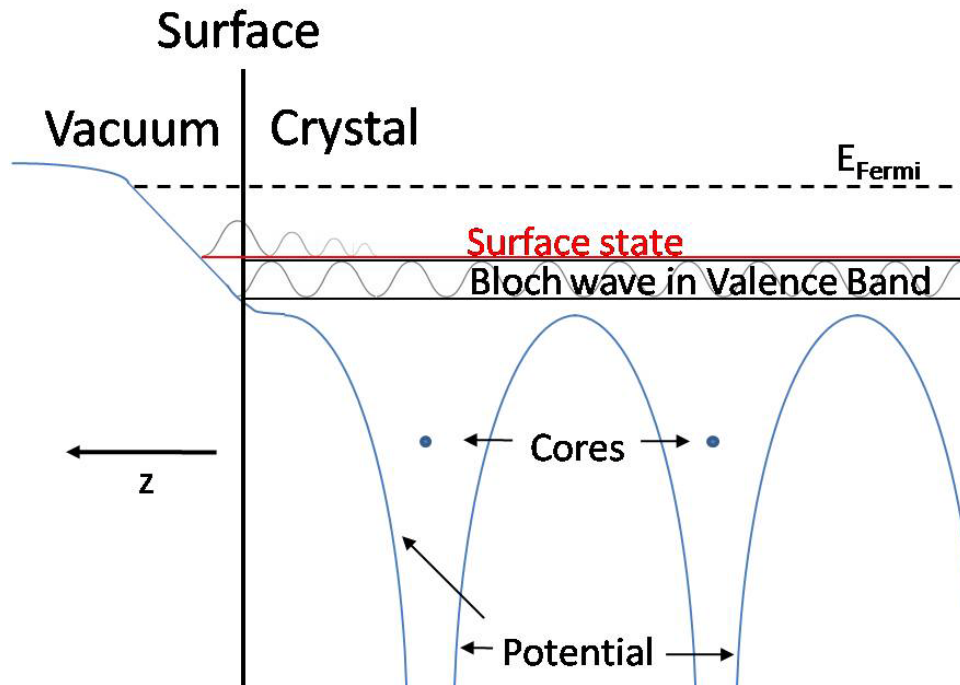

Figure 7.5. Theoretical depiction of a surface state as compared to an occupied valence band for an n-type material. Construction of this figure is based partially on material from Hüfner [6].

Figure 7.5 depicts a Bloch wave both in the valence band as well as in a location between E_{Fermi} and the top of the valence band. Although fundamentally the same as other states since it is still a Bloch wave, one could sub-classify this feature (Figure 7.5) as a possible Shockley or Tamm state; i.e. a surface state, because of the energetic overlap with the bulk valence band energy states [6].

The location of E_{Fermi} in Figure 7.5 is very close to the empty states indicating that this is an n-type material. This is similar to the $Li_2B_4O_7$ surfaces measured in this research and demonstrated in Figure 6.1.

Certainly for the $Li_2B_4O_7(110)$ surface, the possibility of surface states is unsurprising as a Li 1s surface to bulk core level shift has been observed for this surface as discussed in Chapter 5 and elsewhere [7] . The presence of surface states for semiconductors and insulators is certainly not new [8, 9], but these are the first examples reported for $Li_2B_4O_7(110)$. For the $Li_2B_4O_7(100)$ surface, the absence of such states within the gap between the valence band edge and the Fermi level (Figures 6.1(b), 6.1(c), 7.3(c) and 7.3(d)) in the vicinity of the Fermi level, along with a decrease in the conduction band minimum with the photons collected along [010] (Figure 6.1(c)), is consistent with some types of defects at the surface.

The observed intensities of these surface states in photoemission are clearly affected by light polarization (Figure 7.3(a) and 7.3(b)). These surface states are likely of s or p_z character (with z along the surface normal) given that they are enhanced with incident light where the electric vector $\underline{\mathbf{E}}$ is more along the surface normal. For the $Li_2B_4O_7(100)$, there is enhancement of the valence band photoemission intensities where the incident photon electric vector $\underline{\mathbf{E}}$ is more along the surface normal and the in-plane

122

component of the incident light **E** is oriented along the [010] direction (Figure 7.3(d)). It is this surface and crystallographic orientation where the conduction band edge is placed closest to the Fermi level in inverse photoemission (6.1(c)), as just noted. Both the light polarization dependence and the conduction band edge placement for this orientation of the $Li_2B_4O_7$(100) surface could be explained by an increased number of oxygen vacancies as alluded to in Chapter 6 and elsewhere [10, 11]. The loss of surface oxygen coordinated by O $2p_x$ orbitals, with x in-plane and using the surface lattice notation of Figure 6.1, would lead to what is shown as the more polar $Li_2B_4O_7$(100) surface. The placement of the conduction band edge closer to the Fermi level, as shown in Chapter 6 and 8, is consistent with the creation of surface donor states, as might be caused by the oxygen vacancies discussed above, and is evident in the inverse photoemission from the $Li_2B_4O_7$(100) surface (Chapters 6 and 8).

7.7. Energy Dependent Relative Intensity versus Binding Energy

It is also apparent in Figure 7.6 that the bulk wave component for both $Li_2B_4O_7$(110) and (100) have equally little dispersion in the valence band as found earlier for the surfaces. What can be said definitively is that dispersion is unobservable; and that if it does exist, it is less than the resolution of the system. What are noticeable are the resonance features; which will be addressed in Section 7.8.

123
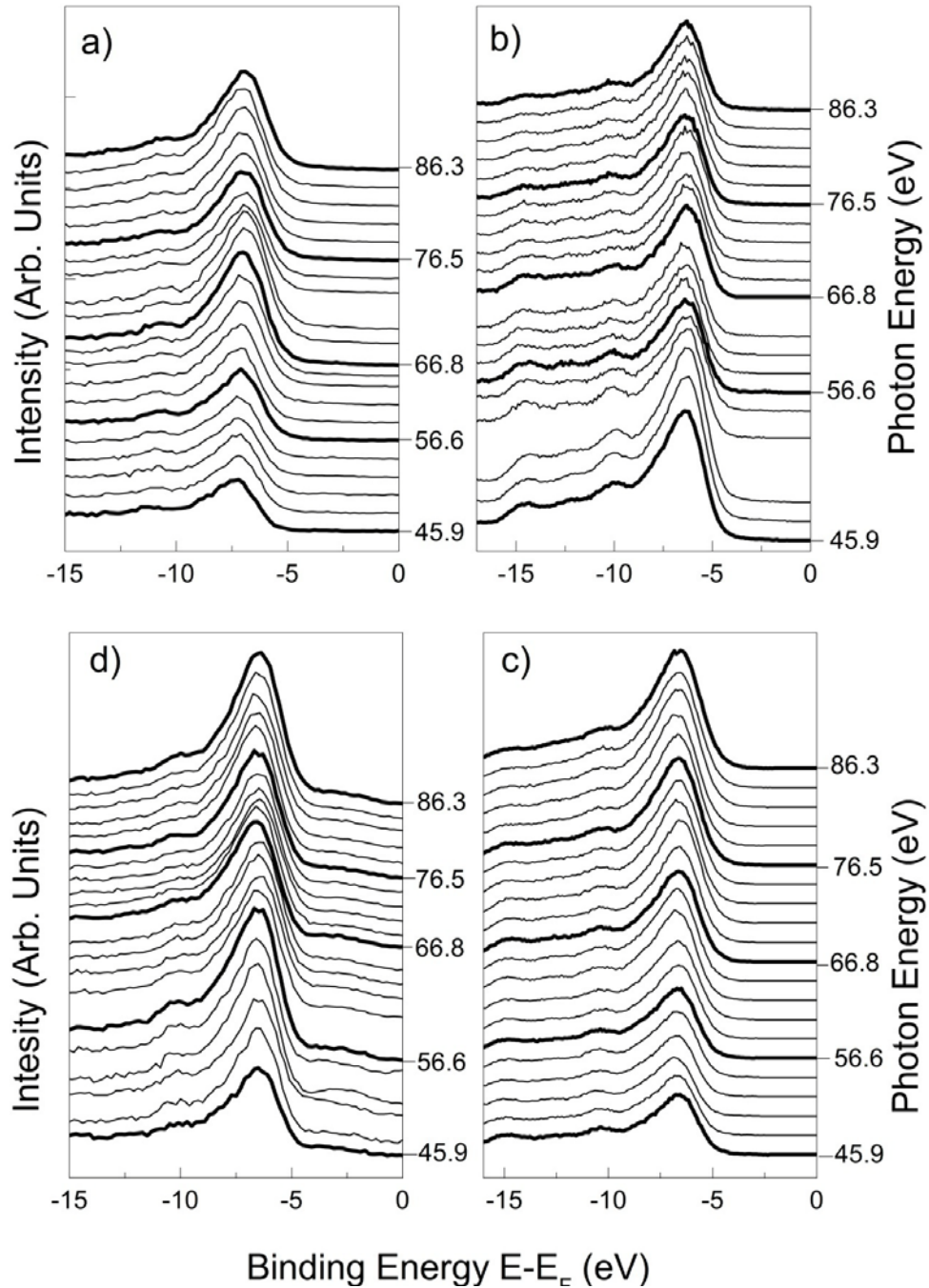
Figure 7.6. Relative intensity vs binding energy of energy dependent photoemission results for (clockwise) solid (a) $Li_2B_4O_7(110)$ oriented [$\underline{1}10$], (b) $Li_2B_4O_7(100)$ oriented [010], (c) $Li_2B_4O_7(100)$ oriented [011], and (d) $Li_2B_4O_7(110)$ oriented [001]. The analyzer is normal to sample; synchrotron light source varies from 46-86 eV in approximate steps of 2 eV and is 45 degrees with respect to sample. Temperature = $350 \pm 5^{o}C$.

124

7.8. Resonant Enhancement

As demonstrated via Figures 7.1(a-c) when compared to Figure 7.1(d), spectral features are generally less distinct as one increases the photon energy when comparing spectra at 56 eV versus 70 eV; but all the features were still resolvable and repeatable from photon energies ranging from 100 eV down to 45 eV.

In spite of the partial density of states calculated in the local density approximation [5], there are experimentally observed resonant enhancements of the valence band maximum for different **E** orientations of the synchrotron produced linear polarized photon energy. One overall enhancement that is artificial, and should therefore be marginalized, is the overall rise in intensity. Typically, one would expect this general rise to a peak value at a specified photon energy followed by a dropping of intensity. This particular artificial feature is a result of the incident wavelength tuned to a respective molecular bond length rather than indicative of any resonance caused by valence band contributions from any particular atomic species, and should be discounted.

For the (110) surface, one observes the most dramatic enhancement along the [001] direction, roughly corresponding to the Li 1s core threshold of about 55 to 56 eV [7] , as shown in Figure 7.7.

125
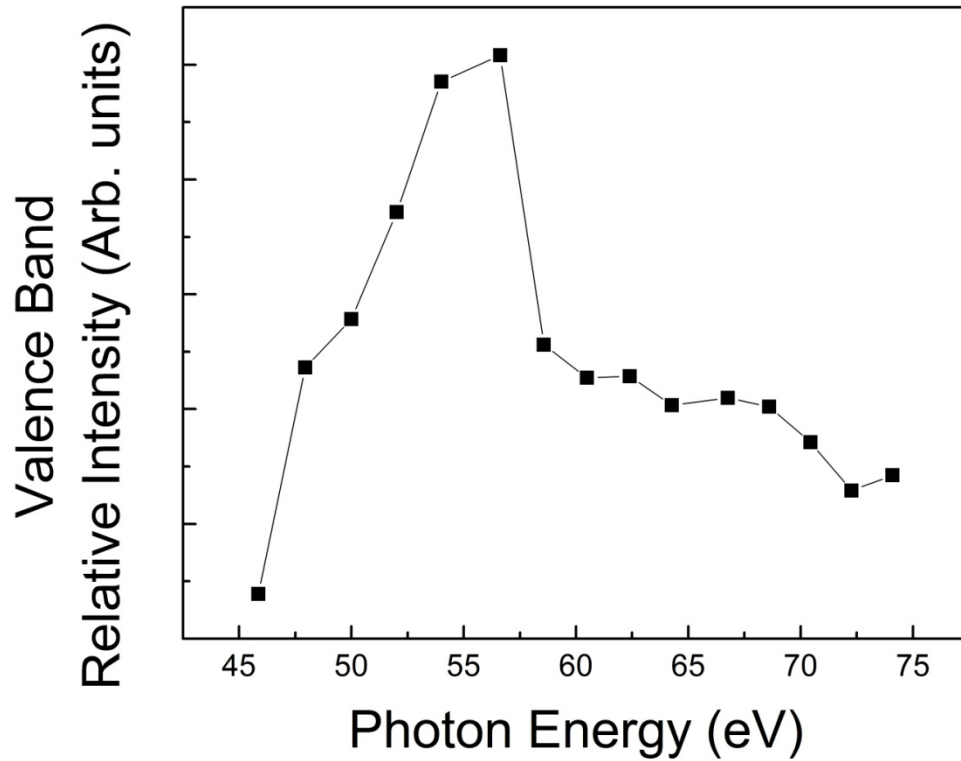
Figure 7.7. The relative intensity at the peak intensity near the valence band maximum (-6.7±0.2 eV, E-EF) versus photon energy depicting resonance for the $Li_2B_4O_7$(110) surface. For all spectra, the with plane component of the incident light, E, is oriented along [001], the light incidence angle was 45 degrees, and the photoelectrons were collected along the surface normal. Data was abstracted from a sequence of photoemission spectra such as those shown in Figure 7.6(d).

By reorienting **E** along the same surface, this time along [110], one does not observe the

same resonance feature at the same energy as indicated in Figure 7.8.
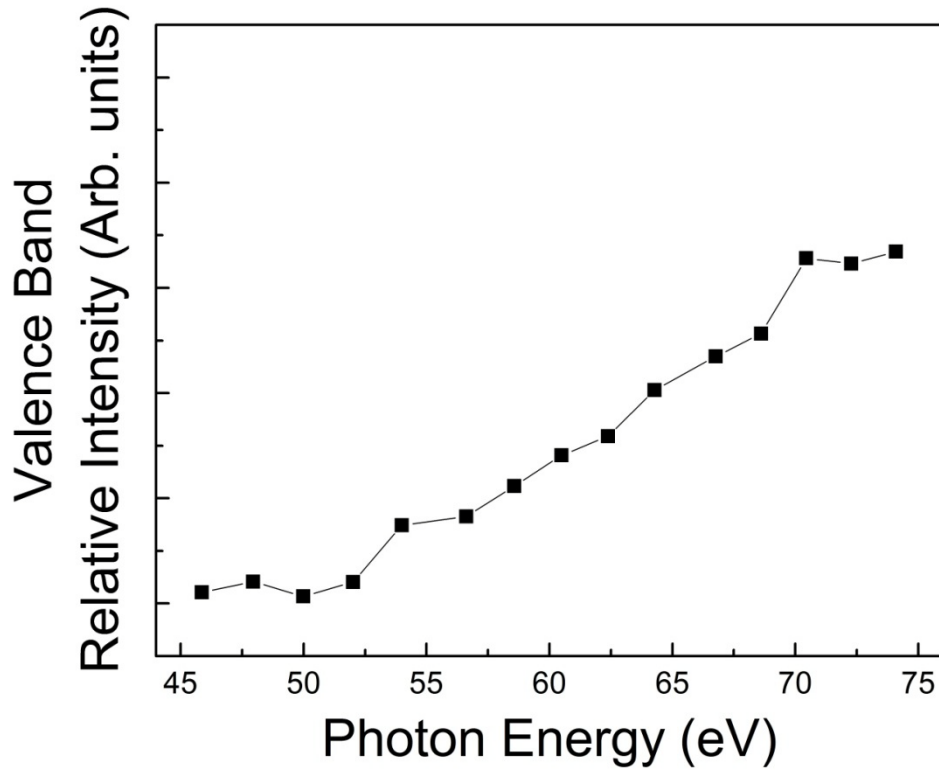
Figure 7.8. The relative intensity at the peak intensity near the valence band maximum (-6.7±0.2 eV, E-E$_F$) versus photon energy depicting resonance for the Li$_2$B$_4$O$_7$(110) surface. For all spectra, the with plane component of the incident light, $\underline{E}$, is oriented along [$\underline{1}$10], the light incidence angle was 45 degrees, and the photoelectrons were collected along the surface normal. Data was abstracted from a sequence of photoemission spectra such as those shown in Figure 7.6a.

This is not unusual given the complex unit cell. Figure 7.7 indicates that there is a

hybridized lithium contribution at the valence band maximum. This particular feature

could be theoretically explained as an Auger electron [12] or Coster-Kronig process [13]

of a Li 1s electron photoexcitation to an unoccupied 2p conduction band state. However,

due to the distance between the interstitially located Li atoms, the most likely candidate

of the two processes is Coster Kronig, which requires only one Li atom. Such a Coster

Kronig mechanism is pictorially displayed below in Figure 7.9.

127
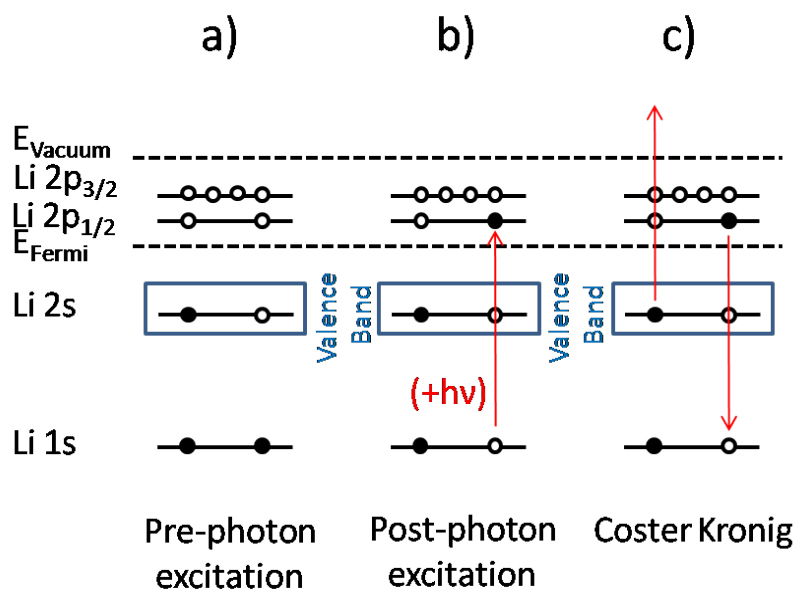
Figure 7.9. Schematic of Coster Kronig process within $Li_2B_4O_7$ that a) portrays lithium atom prior to the photo-excitation, b) excited Li atom to unoccupied state after absorbing photon and c) relaxation back to ground state which energetically requires emission of another electron from the valence band.

Such a lithium contribution, indicated by the resonant enhancement of the valence band maximum in photoemission at the lithium 1s core edge, along with boron contributions to the valence band maximum, could contribute to a more polar (100) surface in the presence of surface oxygen vacancies. Since the lithium atoms are localized interstitially along the longitudinal axis of the crystal lattice [14-21], this is not entirely unexpected.

7.9. $Li_2B_4O_7$(100) and $Li_2B_4O_7$(110) Binding Energy Versus $k\perp$

Throughout the next series of figures (Figures 7.10-13), the perpendicular component of the wave vector is presented along with the binding energy in order to provide a first look at experimental bulk band structure. Broadly, it is clear that both the (110) and (100) surfaces are relatively flat in potential as has been discussed

128

previously [7, 10, 22].

$Li_2B_4 O_7(110)$ exhibits six experimentally repeatable energy levels within the occupied states; the last being a surface state as discussed previously. One can see evidence of this surface state in both directions. Along [$\underline{1}$10] with an increase in photon energy, the surface state feature diminishes below background and is not evident. Along [001] this particular state is apparent up through 100 eV. At first blush, one could argue that there appears some semi-ordered dispersion, but it is not evident where the repeatable Brillioun Zones are which should theoretically be approximately 0.23 Å^{-1} apart.

Figure 7.10. The valence band binding energies versus perpendicular component of wave vector (k⊥) for Li$_2$B$_4$O$_7$(110) surface for valence and shallow core occupied energy states. For all ARUPS spectra used, the in-plane component of the incident light $\underline{E}$ is oriented along [001], the light incidence angle was 45 degrees, and the photoelectrons were collected along the surface normal, and temperature is 625±5 K. ■ denotes a surface state, ● denotes the Highest Occupied Molecular Orbital (HOMO) and ▲ denotes other energy states further from E_F but still located within the valence band.

130

Figure 7.11. The valence band binding energies versus perpendicular component of wave vector ($k\perp$) for $Li_2B_4O_7(110)$ surface for valence and shallow core occupied energy states. For all ARUPS spectra used, the in-plane component of the incident light $\underline{E}$ is oriented along [$\underline{1}$10], the light incidence angle was 45 degrees, and the photoelectrons were collected along the surface normal, and temperature is 625±5 K. ■ denotes a surface state, ● denotes the Highest Occupied Molecular Orbital (HOMO) and ▲ denotes other energy states further from E_F but still located within the valence band.
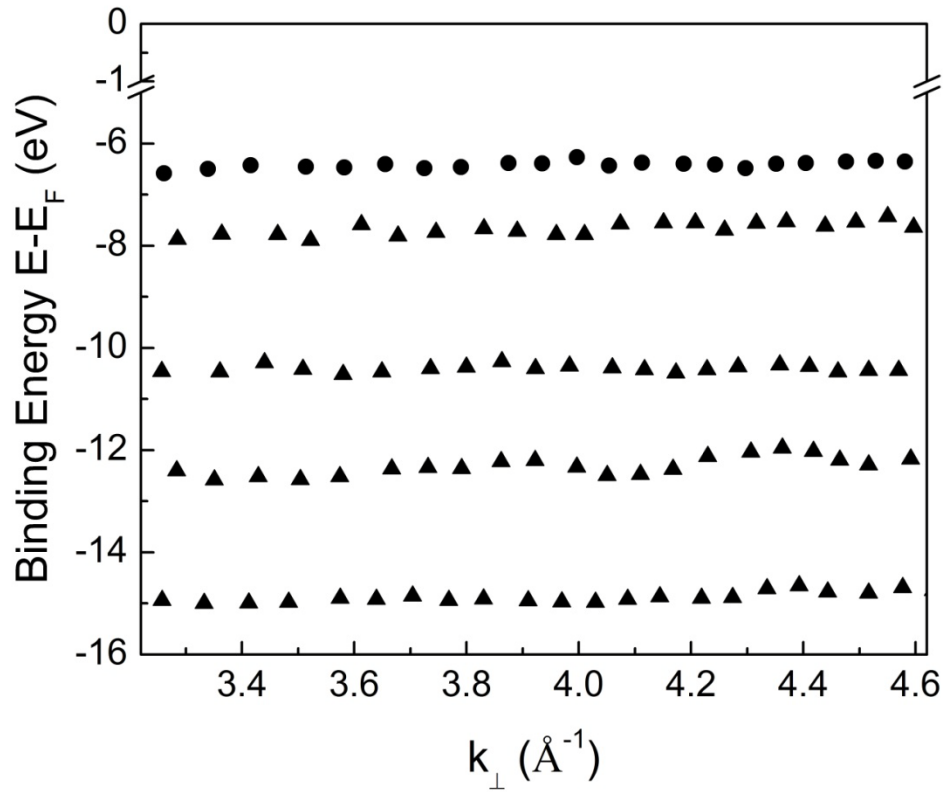
Figure 7.12. The valence band binding energies versus perpendicular component of wave vector ($k_\perp$) for $Li_2B_4O_7$(100) surface for valence and shallow core occupied energy states. For all ARUPS spectra used, the in-plane component of the incident light $\underline{E}$ is oriented along [011], the light incidence angle was 45 degrees, and the photoelectrons were collected along the surface normal, and temperature is 625±5 K. ● denotes the HOMO and ▲ denotes other energy states further from E_F but still located within the valence band.
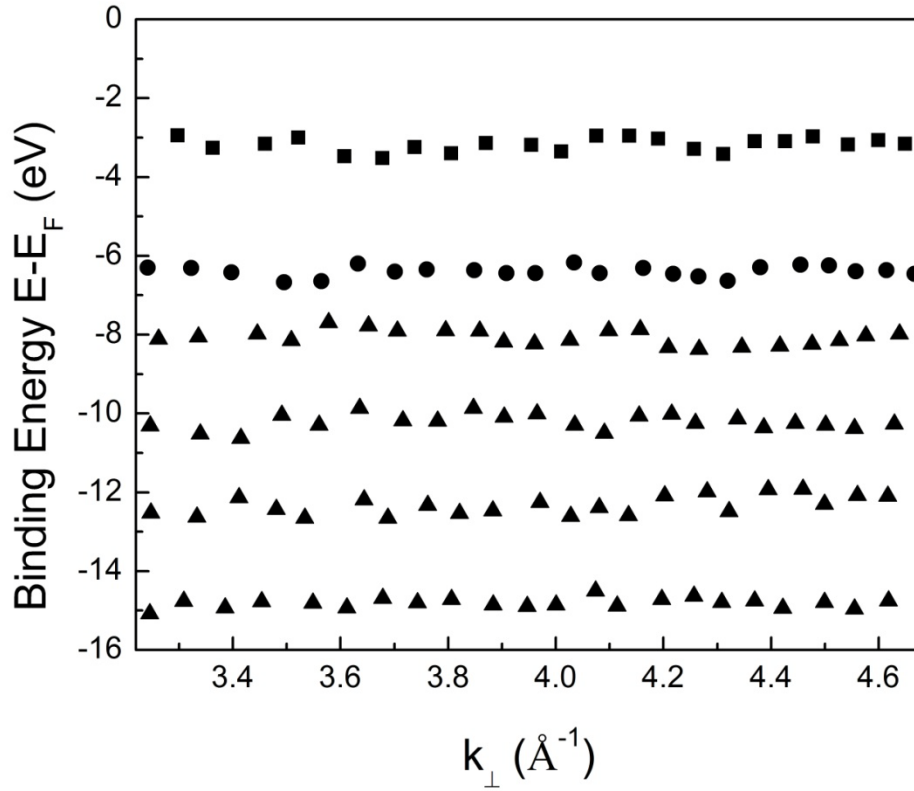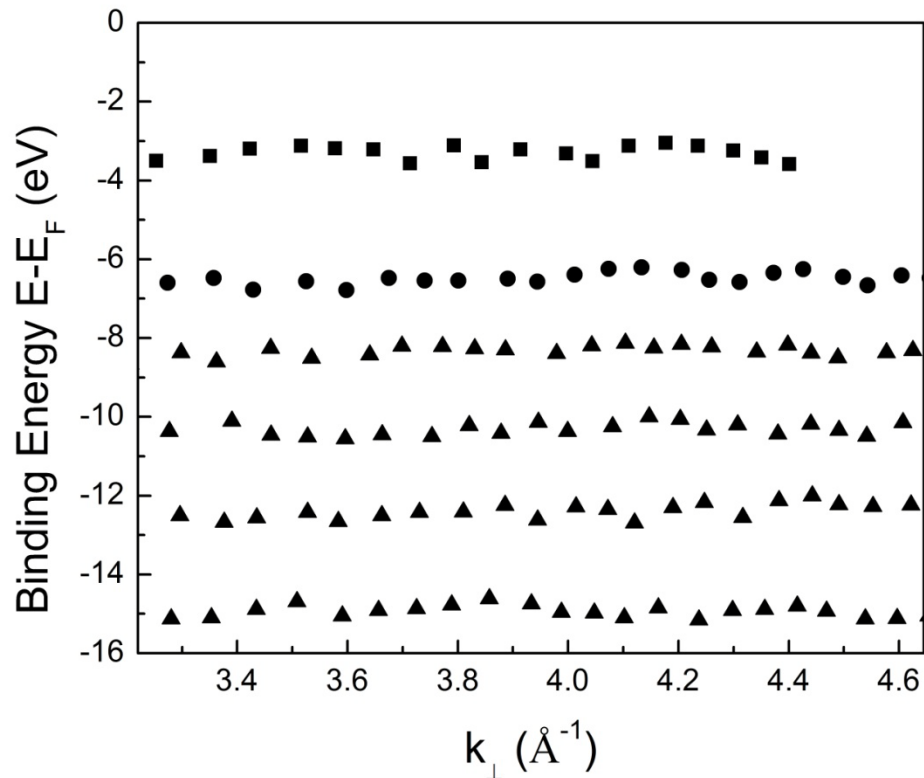
132
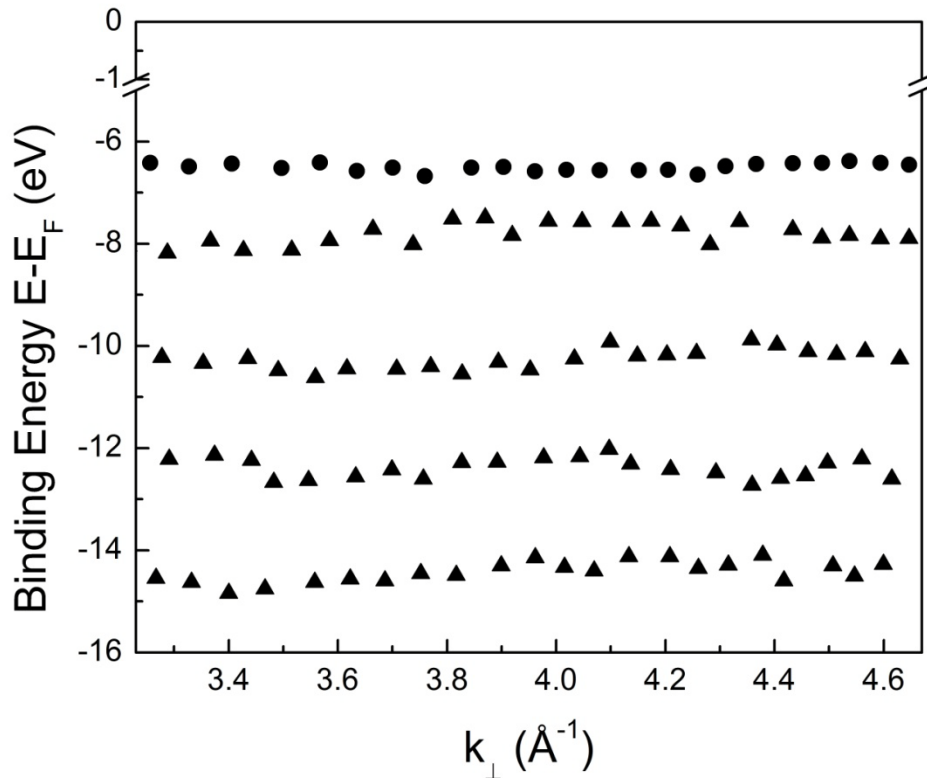
Figure 7.13. The valence band binding energies versus perpendicular component of wave vector ($k_\perp$) for $Li_2B_4O_7(100)$ surface for valence and shallow core occupied energy states. For all ARUPS spectra used, the in-plane component of the incident light $\underline{E}$ is oriented along [010], the light incidence angle was 45 degrees, and the photoelectrons were collected along the surface normal, and temperature is 625±5 K. ● denotes the HOMO and ▲ denotes other energy states further from E_F but still located within the valence band.

Within the more polar $Li_2B_4O_7(100)$, five energy states can be discerned. One does not observe the surface state in either the [011] or [010] directions. Despite a large difference between the [011] and [010] directions as observed in the band gap, the surface is also relatively flat in potential for the bulk occupied states. The theoretical 0.331 $Å^{-1}$ width Brillioun Zone, however, also remains unresolvable as indicated by the data as presented in Figure 7.12 or 7.13, either due to the heavy effective mass or insufficient resolution.

7.10.   Concluding Remarks

Experimental results presented in this chapter indicated that there exists relatively little dispersion within the bulk or surface occupied bands. The character of the valence band was also discussed, with an indication that the $Li_2B_4O_7(100)$ surface was indeed more polar, most likely due to the contribution of O. Various resonance features were presented and discussed with the most prevalent being along the $Li_2B_4O_7(110)$ surface, with **E** oriented [001]. Due to the aperiodicity, an estimate to the lower bounded value was made to the effective mass of the hole carrier. Finally, significant evidence for a new bulk band gap surface state was presented and discussed.

In this chapter, what was relevant to the overall motivation was the further confirmation to the earlier assertion that $Li_2B_4O_7(110)$ was a less polar, more stable surface than $Li_2B_4O_7(100)$.

7.11.   References

1. P. A. Dowben, J. Choi, E. Morikawa, and B. Xu, "The Band Structure and Orientation of Molecular Adsorbates on Surfaces by Angle-Resolved Electron Spectroscopies," in *Handbook of Thin Films,* (Academic Press, 2002), pp. 61-114.

2. E. W. Plummer and W. Eberhardt, "Angle-Resolved Photoemission as a Tool for the Study of Surfaces," in *Advances in Chemical Physics,* I. Prigogine and S. A. Rice, eds. (John Wiley & Sons, Inc., 1982), pp. 533-656.

3. N. V. Richardson and A. M. Bradshaw, "Electron Spectroscopy: Theory, Techniques and Applications," in C. R. Bundle and A. D. Baker, eds. (Academic Press, 1984), pp. 153.

4. Y. B. Losovyj, D. Wooten, J. C. Santana, J. M. An, K. D. Belashchenko, N. Lozova, J. Petrosky, A. Sokolov, J. Tang, W. Wang, N. Arulsamy, and P. A. Dowben, "Comparison of n-type Gd_2O_3 and Gd-doped HfO_2," Journal of Physics: Condensed Matter **21,** 045602 (8pp) (2009).

5. M. M. Islam, V. V. Maslyuk, T. Bredow, and C. Minot, "Structural and Electronic Properties of $Li_2B_4O_7$," J. Phys. Chem. B **109,** 13597-13604 (2005).

6. S. Hüfner, "Surface States, Surface Effects," in *Photoelectron Spectroscopy Principles and Applications,* (Springer-Verlag, 1995), pp. 501.

7. D. Wooten, I. Ketsman, J. Xiao, Y. B. Losovyj, J. Petrosky, J. McClory, Y. V. Burak, V. T. Adamiv, and P. A. Dowbenb, "The Surface Core Level Shift for Lithium at the Surface of Lithium Borate," Phys. B Cond. Mat. (2010).

8. C. Sebenne, "High-resolution photoemission yield and surface states in semiconductors," Il Nuovo Cimento B (1971-1996) **39,** 768-780 (1977).

9. R. Manzke and M. Skibowski, "Occupied and Unoccupied Electronic States on III-V Semiconductor Surfaces," Phys. Scripta **T31,** 87-95 (1990).

10. D. Wooten, I. Ketsman, J. Xiao, Y. B. Losovyj, J. Petrosky, J. McClory, Y. V. Burak, V. T. Adamiv, R. Hengehold, and P. A. Dowben, "Electronic Structure of $Li_2B_4O_7$(110) and $Li_2B_4O_7$(100) (in preparation)," (2009).

11. M. W. Swinney, J. W. McClory, J. C. Petrosky, Y. V. Burak, S. Yang, A. T. Brant, and L. E. Halliburton, "Identification of electron and hole traps in lithium tetraborate ($Li_2B_4O_7$) crystals: Oxygen vacancies and lithium vacancies," Journal of Applied Physics (submitted for publication).

12. M. Nic, J. Jirat, and B. Kosata, "Auger Effect," in *Compendium of Chemical Terminology,* D. McNaught and A. Wilkinson, eds. (Blackwell Scientific Publications, 2006).

13. D. Coster and R. Kronig, "New type of auger effect and its influence on the x-ray spectrum," Phys. **2,** 13-24 (1935).

14. J. Krogh-Moe, "The crystal structure of lithium diborate, $Li_2O.2B_2O_3$," Acta Crystallogr. **15,** 190-193 (1962).

15. J. Krogh-Moe, "Refinement of the crystal structure of lithium diborate $Li_2O.2B_2O_3$," Acta Crystallographica Section B **24,** 179-181 (1968).

16. M. Natarajan, R. Faggiani, and I. O. Brown, "Dilithium tetraborate $Li_2B_4O_7$," Cryst. Struct. Commun. **8,** (1979).

17. S. V. Radaev, L. A. Muradyan, L. F. Malakhova, Y. V. Burak, and V. I. Simonov, Sov. Phys. Cryst. **34,** 842-846 (1989).

135

18. Y. V. Burak, B. V. Padlyak, and V. M. Shevel, "Neutron-Induced Defects in the Lithium Tetraborate Single Crystals," Radiation Effects & Defects in Solids **157,** 1101-1109 (2002).

19. V. T. Adamiv, Y. V. Burak, and I. M. Teslyuk, "Growth and properties of new nonlinear $LiKB_4O_7$ single crystals," Journal of Crystal Growth **289,** 157-160 (2006).

20. E. Day, M. J. Diaz, and S. Adenwalla, "Effect of bias on neutron detection in thin semiconducting boron carbide films," J. Phys. D **39,** 2920-2924 (2006).

21. A. Y. Kuznetsov, A. V. Kruzhalov, I. N. Ogorodnikov, A. B. Sobolev, and L. I. Isaenko, "Electronic structure of lithium tetraborate $Li_2B_4O_7$ crystals. Cluster calculations and x-ray photoelectron spectroscopy," Phys. Solid State **41,** 48 (1999).

22. D. Wooten, I. Ketsman, J. Xiao, Y. B. Losovyj, J. Petrosky, J. McClory, Y. Burak, V. Adamiv, and P. A. Dowben, "Differences in the Surface Charging at the (100) and (110) Surfaces of $Li_2B_4O_7$ in *Nuclear Radiation Detection Materials — 2009*," in *Nuclear Radiation Detection Materials — 2009,* D. L. Perry, A. Burger, L. Franks, K. Yasuda, and M. Fiederle, eds. (MRS, 2009), pp. 1164-L04-04.

136

8. The Unoccupied States of Lithium Tetraborate (110) and (100)

8.1. Overview

In this chapter, experimental results pertaining to angle-resolved inverse photoemission spectroscopy (AR-IPES) of $Li_2B_4O_7(110)$ and $Li_2B_4O_7(100)$ and its analysis will be presented. A representation of the surface band structure in the [$\underline{1}$10], [001], [010] and [011] directions for the unoccupied states will be provided. Additionally, this chapter will discuss the presence of an image state on $Li_2B_4O_7(110)$, make estimations regarding the effective mass of the Lowest Unoccupied Molecular Orbital (LUMO), and make estimates of the respective work functions.

8.2. AR-IPES Relative Intensity versus Binding Energy

After obtaining and adjusting the AR-IPES spectra for charging and finding E_{Fermi} using an Au standard ($E_{Fermi} = 7.2$ eV) as discussed in Chapter 4 and elsewhere, several general features were apparent. The LUMO is found between 2.3 and 3.8 eV above E_{Fermi} depending on the crystal orientation along with a higher unoccupied state. Additionally, a non-periodic feature was also identified only in the $Li_2B_4O_7(110)$ surface along both the [$\underline{1}$10] and [001] orientations, which will be discussed in detail later. As expected, the intensity continues to generally increase with an increase in the number of incident electrons; until reaching a continuum of states consistent with those outside the influence of the crystal. Figure 8.1 provides intensity versus binding energy examples in all four directions and both crystal faces.

137
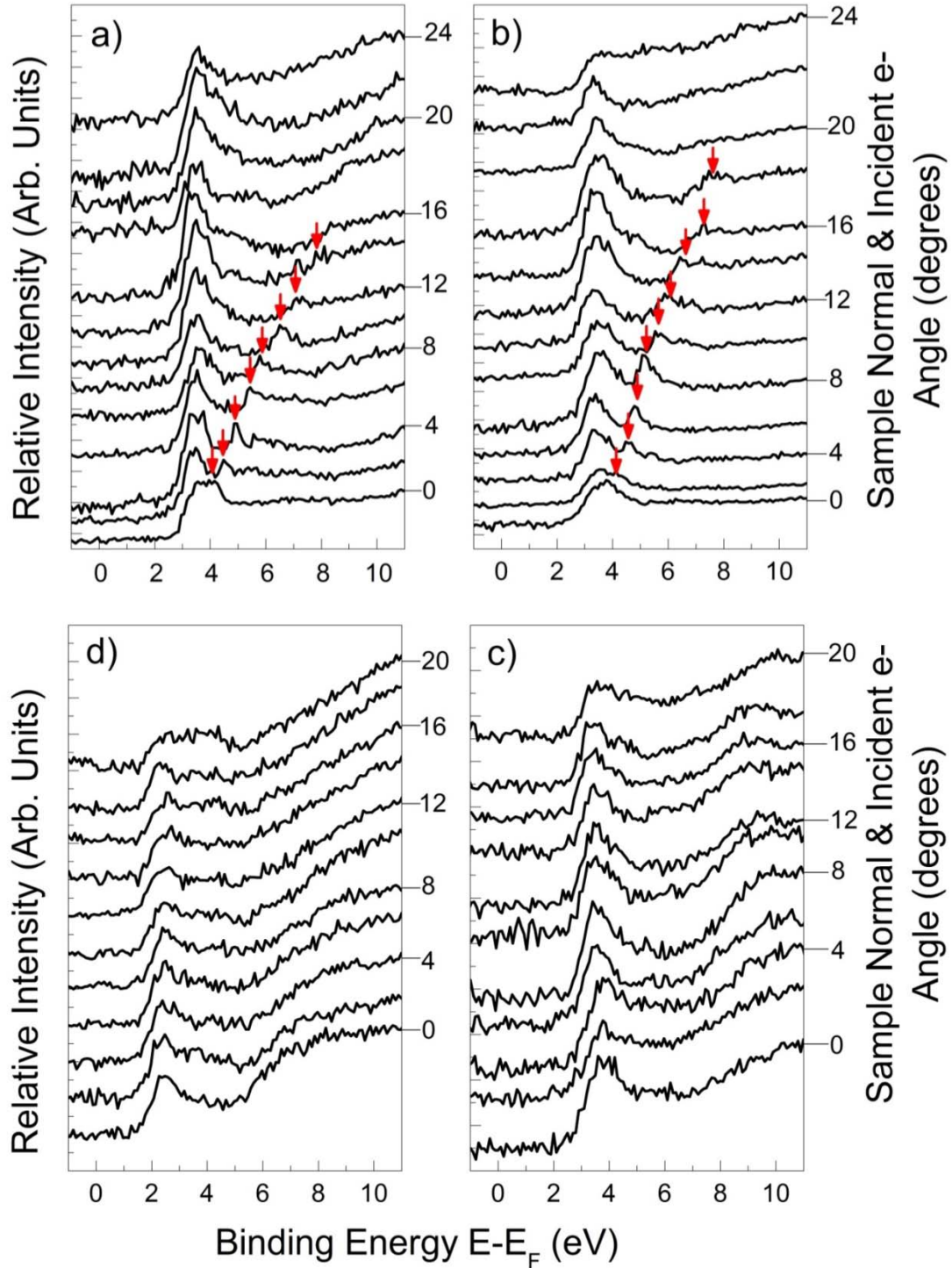
Figure 8.1. The incidence angle inverse photoemission spectra for $Li_2B_4O_7(110)$ with increasing incidence angle (wave vector) along the a) [$\underline{1}10$] and b) [001] direction; and $Li_2B_4O_7(100)$ along c) [011] and d) [010] directions. The image state wave vector dependent (incidence angle) dispersion (see text) is indicated by the arrows($\downarrow$). The unoccupied state binding energies are given in terms of $E\text{-}E_F$.

8.3. Binding Energy versus $k_{\parallel}$

Similar to what was done with the occupied states, the parallel momentum ($k_{\parallel}$) can be derived as follows from the incident electron kinetic energy and the electron incidence angle (θ) with respect to the surface normal [1-3]:

$$k_{\parallel} = \sqrt{\frac{2mE_{kin}}{\hbar^2}} \sin(\theta) = 0.512\text{Å}^{-1} \sqrt{\frac{E_{kin}}{eV}} \sin(\theta). \tag{53}$$

In contrast to the results garnered from the angle-resolved photoemission, dispersion is clearly evident in empty states from the AR-IPES results obtained as a function of electron incidence angle (θ), as shown in Figures 8.1 and 8.2. Using the incident electron kinetic energy and Equation (53) [4, 5], an experimental unoccupied state band dispersion has been mapped, as shown in Figure 8.2.

Figure 8.2. The unoccupied state binding energies versus the surface parallel wave vector are mapped for the $Li_2B_4O_7(110)$ along the a) [$\underline{1}10$] and b) [001] directions. The surface Brillouin zone critical points are denoted at top. ● denotes the Lowest Unoccupied Molecular Orbital, ▲ indicates a higher energy empty state and ■ exhibits an image state. Theoretical Brillouin zone widths are a) 0.234 $\mathring{A}^{-1}$ and b) 0.305 $\mathring{A}^{-1}$, respectively.

Despite the lower resolution of inverse photoemission, one is able to observe dispersion of the bands at the conduction band minimum, as shown in Figure 8.2. The periodicity of the dispersion of the states at the conduction band minimum is consistent with the expected Brillouin zone of the $Li_2B_4O_7(110)$ surface, as plotted in Figure 8.2, along both the [$\underline{1}10$] and [001] directions. A nearly parabolic light mass band is also shown to disperse independent of the surface Brillouin zone, as shown in Figure 8.1 and Figure 8.2. This latter light mass band observed for the $Li_2B_4O_7(110)$ surface, along

140

both the [001] and [$\underline{1}$10] directions of the surface Brillouin zone, at binding energies (E-E$_F$) well above the Fermi level, is an image state as will be discussed later. Although such a feature could theoretically be present in Li$_2$B$_4$O$_7$(100), it is not evident in either direction as shown in Figure 8.3. Further discussion of this feature will be covered in Section 8.5.

As can be shown in Figure 8.3, this dispersion in the unoccupied states is not as apparent in Li$_2$B$_4$O$_7$(100); which does exhibit dispersion but only roughly matches periodically what is theoretically predicted:

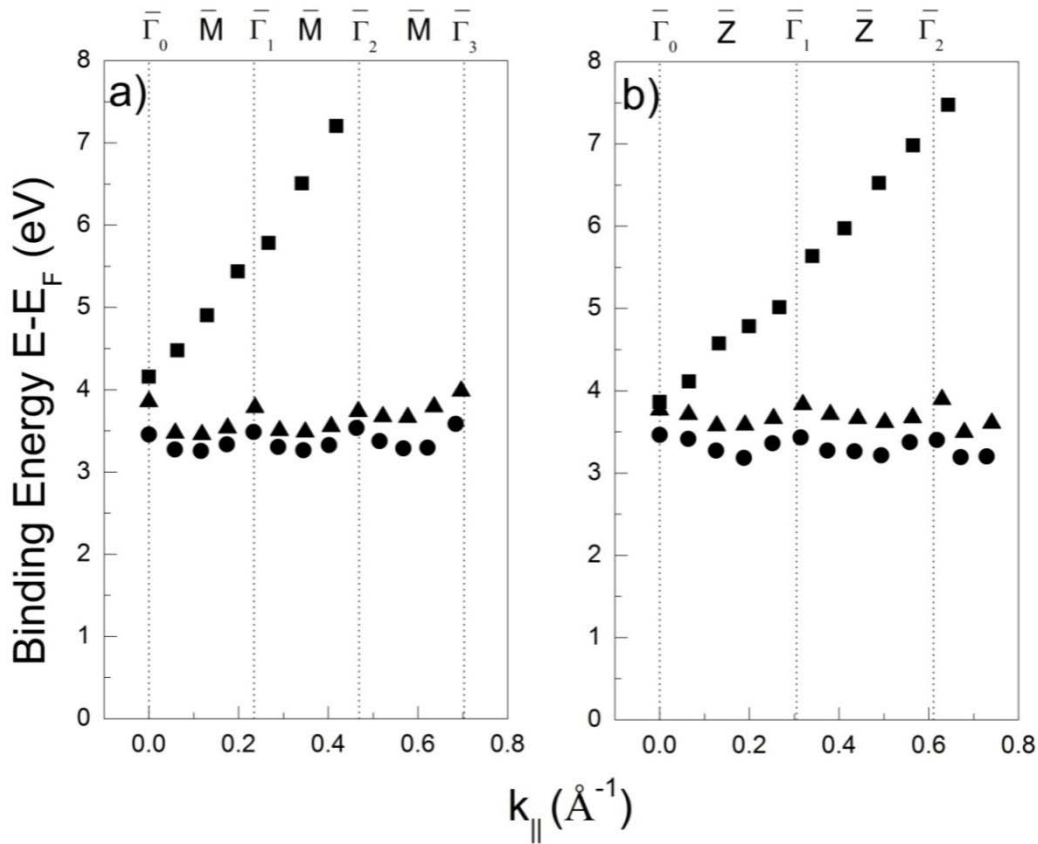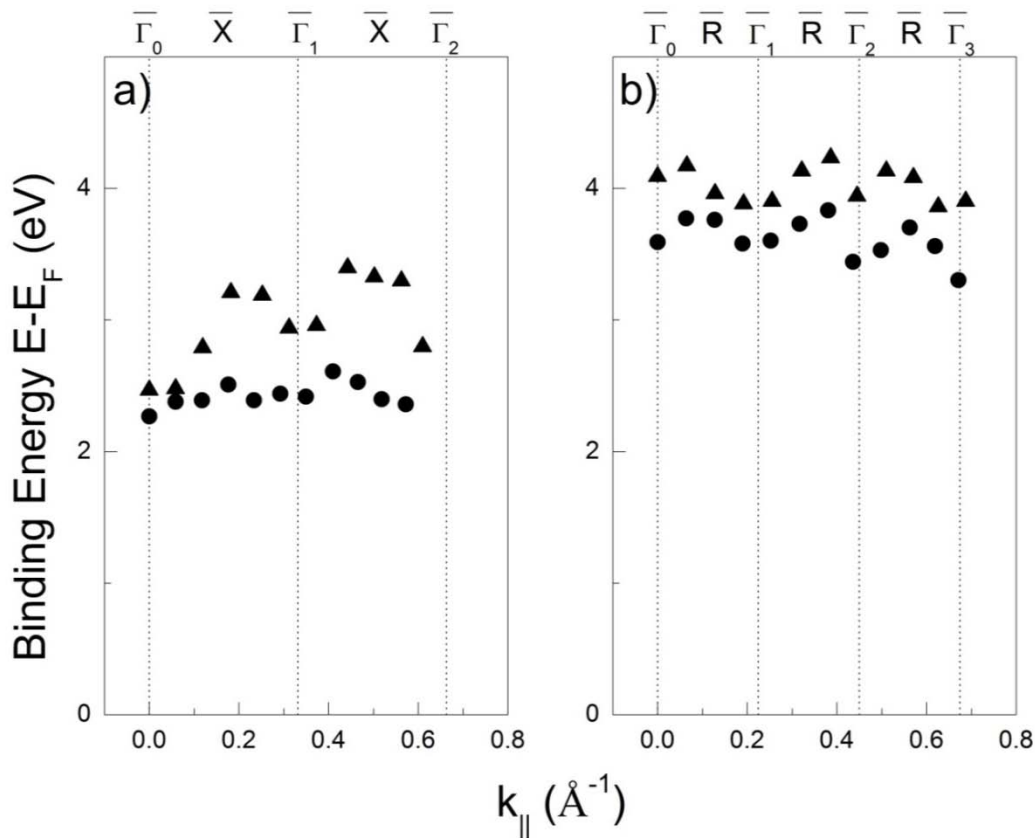**Figure 8.3. The unoccupied state binding energies versus the surface parallel wave vector are mapped for the Li$_2$B$_4$O$_7$(100) along the a) [010] and b) [011] directions. The surface Brillouin zone critical points are denoted at top. ● denotes the Lowest Unoccupied**

Molecular Orbital and ▲ indicates a higher energy empty state. Theoretical Brillouin Zone widths are a) 0.331 Å^{-1} and b) 0.225 Å^{-1}, respectively.

Given that both surfaces were prepared and cleaned identically (Chapter 4), the most likely explanation of this difference is due to $Li_2B_4O_7(100)$ being the more polar surface; which would mask an image potential state. This changing dipole with changing angle could create a slight shift in unoccupied surface states, which translates to a less periodic dispersion curve as shown in Figure 8.3. The presence of O defects in $Li_2B_4O_7(100)$ could explain the slightly less ordered surface, which would account for the lack of observation of this feature.

8.4. Effective Mass Estimates

By linearly fitting the derivative of the binding energy with respect to the parallel wave vector component versus the parallel wave vector component ($\frac{dE}{dk_\parallel}$ vs $k_\parallel$), an estimate of the carrier effective masses for the unoccupied $Li_2B_4O_7(110)$ and $Li_2B_4O_7(100)$ states can be determined.

$$\frac{dE}{dk_\parallel} = \frac{\hbar^2}{m^*} k_\parallel \tag{54}$$

Examples of this technique that were used for the Lowest Unoccupied Molecular Orbital (LUMO) are provided in Figure 8.4.
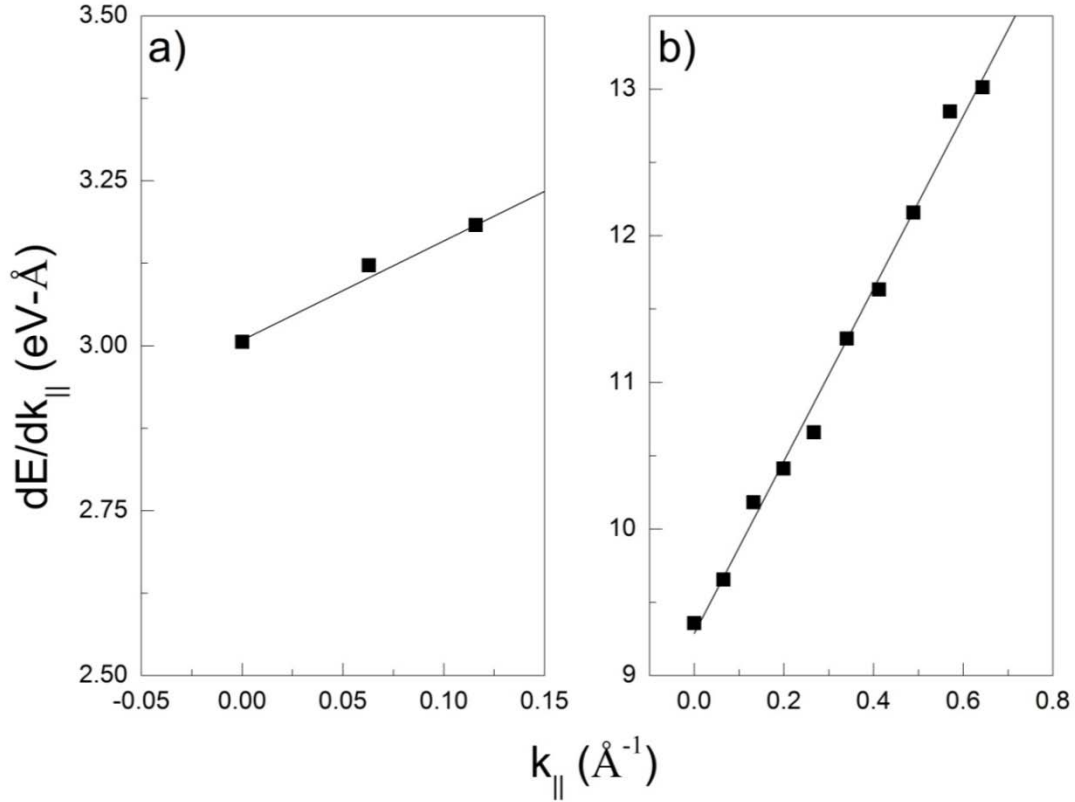
Figure 8.4. $dE/dk_\parallel$ versus $k_\parallel$ of unoccupied states for a) $Li_2B_4O_7(100)$ LUMO oriented along [011] and the $Li_2B_4O_7(110)$ image state oriented along [$\underline{1}$10].

Near the conduction band minimum, the LUMO ranges from 3.9 to 4.6 [m^*/m_e], with the greatest consistency in the $Li_2B_4O_7(110)$ surface. The image state, to be discussed later, yielded 1.6 and 2.5 [m^*/m_e] for the [$\underline{1}$10] and [001] directions. It is evident that compared to the estimated occupied states' effective masses (discussed in Chapter 7) the unoccupied states possess considerably lighter effective masses, as summarized in Table 8.4.

143

Table 8.4. Summary of effective mass values in both surfaces for HOMO, LUMO and image states. Note: Due to inability to resolve any periodicity, the HOMO values are only lower bound estimates. The provided ratio is with respect to the electron rest mass.

Band of interest	Li$_2$B$_4$O$_7$(110) surface (m^*/m_e)		Li$_2$B$_4$O$_7$(100) surface (m^*/m_e)	
	Along [$\underline{1}$10]	Along [001]	Along [010]	Along [011]
HOMO	≥11.22	≥11.49	≥10.81	≥14.17
LUMO	4.29±0.26	4.32±0.26	3.93±0.24	4.61±0.28
Image State	1.60±0.10	2.50±0.15	N/A	N/A

Recalling the Drude electron transport model [6, 7], an illustrative, albeit overly simplistic, model [8] we can also see how charge carrier velocity ($\vec{v}$) is (roughly) inversely proportional to effective mass (m^*):

$$\vec{v} = \frac{e\tau}{\|m^*\|}\vec{E}, \qquad (55)$$

where e, τ and $\vec{E}$ are the electron charge, mean time between collisions and electric field, respectively. In essence, this model makes the point that the heavier the effective mass the slower the charge carrier will be; a generally undesirable characteristic for responsive solid state devices.

8.5. Li$_2$B$_4$O$_7$(110) Image State

An image potential state is a feature best described as actual electrons trapped between the surface barrier potential and the crystal surface. This interesting feature was first predicted by Echenique and Pendry [9] and has been proven experimentally on several occasions since. [9, 10] Figure 8.2 provides evidence of such a feature for

144

Li$_2$B$_4$O$_7$(110) surface. There was no image potential state observed for the

Li$_2$B$_4$O$_7$(100) surface.

Image states are characteristic of clean, flat, largely defect free surfaces. The

absence of any image states for the Li$_2$B$_4$O$_7$(100) surface is consistent with the presence

of defects at this surface; defects which are very likely surface oxygen vacancies, as has

been noted in Chapters 6 and 7. The presence of an image state for the Li$_2$B$_4$O$_7$(110)

surface would indicate that this surface is largely defect free with a very flat surface

potential. A flat potential would allow a potential image state to not be perturbed by the

surface crystallography and to disperse almost independently of the surface Brillouin

zone. The Li$_2$B$_4$O$_7$(110) Rydberg-like state's dispersion is certainly not periodic in

nature and, in fact, is shown to be simply parabolic both the along [001] and [$\underline{1}$10]

directions of the surface as indicated in Figure 8.2(a-b) and Figure 8.4(b).

As noted in Chapter 7, the Li$_2$B$_4$O$_7$(110) surface is also distinguished by a

surface that exhibits very little light polarization dependence in the bulk valence band

states, is flat in potential (Figure 8.2), and, as will be discussed in detail in Chapter 9, is

also characterized by an off-axis pyroelectric effect [11]. All these effects may combine

to explain the reduction of the surface potential variations leading to the parabolic image

potential state that is shown above in Figure 8.2. Using Equation (54), one can also see

that the image state for the Li$_2$B$_4$O$_7$(110) surface possesses a very light effective mass of

$m*/m_e$, as expressed in Table 8.1.

In addition, this is indeed an image potential state for two other reasons. First,

this feature was not observable via PES, leading to the assumption that this is an empty

145

state feature. Second, the feature is considerably more pronounced after thorough

cleaning of the surface as expected for an actual image state [12].

Further corroborating evidence to support the assertion of a $Li_2B_4O_7(110)$ image

state would be gained if this same feature was temperature independent and pinned to

E_{vacuum}. The experiment to test the former attribute was inconclusive, due to the

temperature difference being so minute between spectra. Testing whether the feature is

pinned to E_{vacuum} can be simply done, as in [13], by observing the shift with the

introduction of a work function changing adsorbate. One would observe a true image

state if the feature maintained the same distance in energy between itself and E_{vacuum}. If a

slight amount of an adsorbate was added, the work function (the energy difference

between E_F and E_{vacuum}) will shift accordingly. Additionally, the image potential state

would shift by the same amount as the difference between the pure $Li_2B_4O_7(110)$ and

$Li_2B_4O_7(110)$ plus adsorbate work functions, with a corresponding reduction of image

state intensity as it starts to get masked [13]. This aspect was not addressed in the work

presented here; but should be considered for future work.

8.6. Experimentally Derived Work Function

By focusing on mapping the $Li_2B_4O_7(110)$ and $Li_2B_4O_7(100)$ empty states AR-IPES

also yielded another ancillary characteristic, an estimate of the work function. The

bottom of the image state indicate the Rydberg states of the surface, but one must make

the reasonable assumption that the surface momentum ($\hbar k$) of the trapped electrons is

minimized, i.e. the parallel wave vector component, $k_{\parallel}$ is equal to zero. As depicted in

146

Figure 8.2, one can estimate the work function of $Li_2B_4O_7(110)$ oriented along $[\underline{1}10]$ from the position of the image state, as 4.0 ± 0.3 eV.

8.7. Concluding Remarks

AR-IPES measurements on the $Li_2B_4O_7(110)$ and $Li_2B_4O_7(100)$ surfaces resulted in several notable findings. Unlike the occupied states, measurable dispersion was apparent in both surfaces in all four directions. Additionally, a Rydberg-like, image potential state was evident in $Li_2B_4O_7(110)$ that was not present in $Li_2B_4O_7(100)$; yet further evidence of the presence of surface defects in the latter. An estimation of charge carrier effective mass was made, which indicated considerably lighter values in the unoccupied states versus the occupied states. Finally, a rough estimate of work function was determined for these surfaces.

By mapping the empty states, the overall motivation of this research was supported. First, there is the further confirmation that $Li_2B_4O_7(110)$ is the more stable, less defect filled of the two surfaces. Second, an estimation of the undoped effective mass for LUMO and HOMO and the work function of both surfaces have been provided, which would be a starting point as input information for inclusion in various modeling programs in order to determine doping optimization.

8.8. References

1. E. W. Plummer and W. Eberhardt, "Angle-Resolved Photoemission as a Tool for the Study of Surfaces," in *Advances in Chemical Physics,* I. Prigogine and S. A. Rice, eds. (John Wiley & Sons, Inc., 1982), pp. 533-656.

2. N. V. Richardson and A. M. Bradshaw, "Electron Spectroscopy: Theory, Techniques and Applications," in C. R. Bundle and A. D. Baker, eds. (Academic Press, 1984), pp. 153.

147

3. P. A. Dowben, J. Choi, E. Morikawa, and B. Xu, "Characterization and Spectroscopy of Thin Films," in *Handbook of Thin Films,* H. Nalwa, ed. (Academic Press, 2002), pp. 61-114.

4. N. V. Smith, "Inverse Photoemission," Rept. Prog. Phys. **51,** 1227-1294 (1988).

5. D. Q. Feng, D. Wisbey, Y. B. Losovyj, Y. Tai, M. Zharnikov, and P. A. Dowben, "Electronic structure and polymerization of a self-assembled monolayer with multiple arene rings," Phys. Rev. B **74,** (2006).

6. P. Drude, "Zur Elektronentheorie der Metalle," Annalen der Physik **306,** 566-613 (1900).

7. P. Drude, "Zur Elektronentheorie der Metalle; II. Teil. Galvanomagnetische und thermomagnetische Effecte," Annalen der Physik **308,** 369-402 (1900).

8. N. W. Ashcroft and N. D. Mermin, "Solid State Physics," in (Thomas Learning, 1976), pp. 1-62.

9. P. M. Echenique and J. B. Pendry, "The existence and detection of Rydberg states at surfaces," J. Phys. C **11,** 2065 (1978).

10. W. Steinmann, "Spectroscopy of image-potential states by two-photon photoemission," Appl. Phys. A **49,** 365-377 (1989).

11. I. Ketsman, D. Wooten, J. Xiao, Y. B. Losovyj, Y. V. Burak, V. T. Adamiv, A. Sokolov, J. Petrosky, J. McClory, and P. A. Dowben, "The off-axis pyroelectric effect observed for lithium tetraborate," APL (2010).

12. G. Thörner, G. Borstel, V. Dose, and J. Rogozik, "Unoccupied electronic surface resonance at Cu(001)," Surf. Sci. **157,** L379-L383 (1985).

13. V. Dose, W. Altmann, A. Goldmann, U. Kolac, and J. Rogozik, "Image-Potential States Observed by Inverse Photoemission," Phys. Rev. Lett. **52,** 1919 (1984).

9. $Li_2B_4O_7$ Hysteretic, Pyroelectric and Piezoelectric Attributes

9.1. Overview

This chapter provides analysis of additional surface and bulk characteristics that were observed during the course of this research that were ancillary in nature; and outside the initial focus of determining the electronic structure via band mapping. Beyond a solid state physics interest, the above characteristics explored in this chapter have only an indirect support to the overall motivation as described in Chapter 2. What is novel is the idea of using $Li_2B_4O_7(110)$ to demonstrate the tensor nature of the pyroelectric coefficient, something that had been theoretically predicted over fifty years previous, but never experimentally demonstrated. What is essential according to our overall motivation as expressed in Chapter 2 is actually a subtle detail; that is, the ability to conduct these types of measurements implies that we were able to manufacture workable contacts on the samples. This is an important milestone for any device that would incorporate lithium tetraborate. An example of these contacts incorporated in a device will be addressed in the final chapter.

After providing the background as well as additional experimental details not covered in Chapter 4, this chapter demonstrates the hysteretic behavior in the heating-cooling cycles. Sections on off-axis pyroelectricity and surface piezoelectric effects will follow.

9.2. Background

Any given crystal may exhibit a combination of many different thermal, mechanical, electrical and magnetic properties. These attributes are not always

149

independent and often interact in a complex manner. A visual model can best

demonstrate this complex correlation between the thermal, electrical, and mechanical

properties and is displayed in Figure 9.1:
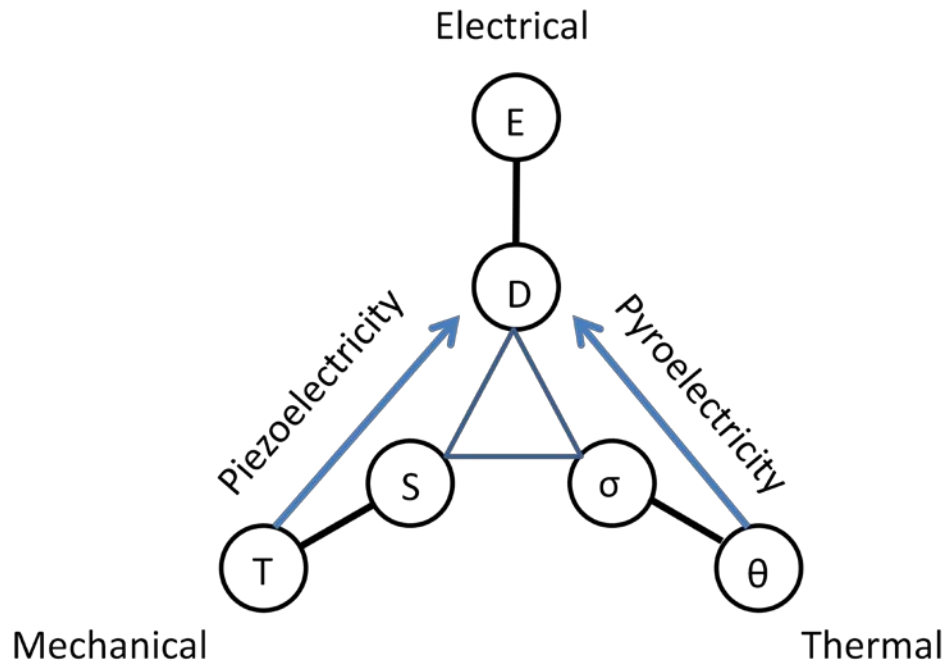
Figure 9.1. Thermal, electric and mechanical properties illustrating thermodynamically reversible interactions as well as their co-dependence. Three pairs of circles: stress (T) and strain (S); electric field (E) and electric displacement (D); as well as temperature (θ) and entropy (σ) define the physical properties of elasticity and electrical permittivity and heat capacity. Magnetic properties are not included for this model. Portions of this diagram are abstracted from Lang's work [1].

Depicted above and highlighted via two arrows in Lang's model are two effects

that were observed with undoped $Li_2B_4O_7$: pyroelectricity and piezoeletricity. In its

simplest definition, pyroelectricity relates a general change in temperature with a

subsequent change in electrical displacement; while piezoelectricity's electrical

displacement's is produced by a change in the mechanical stress [1, 2]. Using the same

150

Figure 9.1, one can easily surmise the inverse relationships. As an example, the inverse piezoelectric effect is simply a general reversal of the latter, that is, any change in the electric field will induce an additional change in the mechanical strain of the crystal.

The study of pyroelectricity has a long and rich history [1], but there have been good reasons to suspect for more than half a century [2] that the general models of pyroelectricity tend to be simplistic. Pyroelectricity is usually measured as a current that occurs with changing temperature along the direction of spontaneous polarization [1-4]. All pyroelectric materials are piezoelectric, because the necessary spontaneous polarization only occurs in materials with a unique polar axis [2, 3]. This is one of three conditions for any material to exhibit the pyroelectric effect, the other two include having either a single axis of rotational symmetry, or none at all and possessing no center of symmetry [1].

For a piezoelectric material we expect that the charge density D_i is related to the stress X_{jk} by [2, 3]:

$$D_i = d_{ijk}X_{jk} \tag{56}$$

where the piezoelectic coefficients d_{ijk} form a third rank tensor. An electric field can alter the surface charge density D_i as the strain is related to the applied electric field $\underline{\mathbf{E}}$ by:

$$X_{ij} = d_{ijk}\underline{E_k}. \tag{57}$$

Assuming that the material is within the elastic region, Hooke's (generalized) law applies to describe the relationship between stress (X_{ij}) and strain (ϵ_{kl}), tensors via the fourth order elastic stiffness tensor, C_{ijkl} [5]:

151

$$X_{ij} = C_{ijkl}\epsilon_{kl}. \tag{58}$$

The pyroelectric effect should also be a tensor because the surface charge density D_i, induced by a change in temperature T, is also related to the change in static polarization $P_{S,i}$. This, in turn is related to the pyroelectric coefficient p_i:

$$D_i = \Delta P_{S,i} = \frac{dP_{S,i}}{dT}\Delta T = p_i\Delta T. \tag{59}$$

From Equations (58) and (59), with changes in temperature, there is an expected anisotropy of the electric constants and the resulting "stress" with temperature, particularly in a noncubic pyroelectric crystal [2]. Although the pyroelectric coefficient is generally treated as a vector [2, 3], from observing Equations (56) and (58) one notes the implied tensor character that is greater than a first order tensor. This is the result of the coupling to the stress-strain tensor as well as the accompanying tensor character of the piezoelectric effect. Indeed it is recognized that there is a secondary pyroelectric effect that can occur if the pyroelectric crystal is allowed to deform along directions other than the polar direction [2]. This is schematically depicted in Figure 9.2.
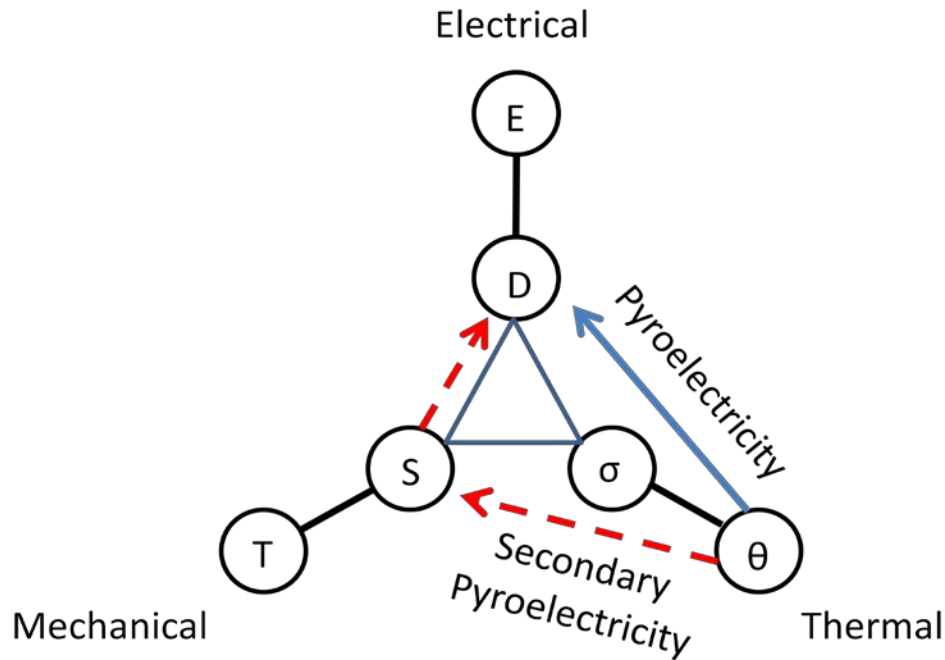
Figure 9.2. Thermal, electric and mechanical properties illustrating thermodynamically reversible interactions depicting primary pyroelectric effect (solid arrow) and secondary pyroelectric effect (dashed arrows). The symbols are defined as in Figure 9.1. Portions of this diagram are abstracted from Lang's work [1].

This shows that Equation (59), relating the surface charge density D_i to the pyroelectric coefficients p_i, is over-simplistic, as this effort conclusively demonstrates for lithium tetraborate. Prior optical studies have provided some indications of an off- axis pyroelectric effect along crystal directions orthogonal to the polar axis of some translucent pyroelectric crystals [6], but not for lithium tetraborate.

Lithium tetraborate is a tetragonal crystal as discussed in Chapter 1 and elsewhere [7-9] with an appreciable pyroelectric coefficient in the region of 100 K to 250 K [10, 11]. As the tetragonal crystal lattice of lithium tetraborate is the result of stretching a cubic lattice along one lattice vector, so that the unit cell is a rectangular prism with a square base (*a* by *a*) and height (*c*, which differs from *a*). The [110] and

[100] crystal directions are orthogonal to the polar [001] direction for the tetragonal crystal lattice and thus candidates for the study of an off-axis pyroelectric effect.

9.3. Experimental Considerations

Pertinent details regarding the lithium tetraborate (110) and (100) samples used for this study, determination of the Fermi level, and the techniques used in conducting temperature dependent angle-resolved photoemission have already been addressed in Chapter 4 and elsewhere [12-17].   Only those aspects not covered in Chapter 4 are addressed in this section.

The pyroelectric measurements along the [110] and [100] directions were performed in a manner similar to prior studies [10, 18] over a range of heating rates from 0.015 to 0.4 K/sec. At the lowest temperatures (50 K – 70 K), the heat and cooling rates deviate from the linear, and these deviations have been taken into account in the analysis. To avoid tertiary pyroelectricity (false secondary pyroelectricity) due to uneven heating [2], the pyroelectric measurements were undertaken in a copper enclosed apparatus to ensure uniform heating and an absence of illumination. Figure 9.3 depicts a schematic of the procedure used by Bhalla et al [1, 10, 18]:
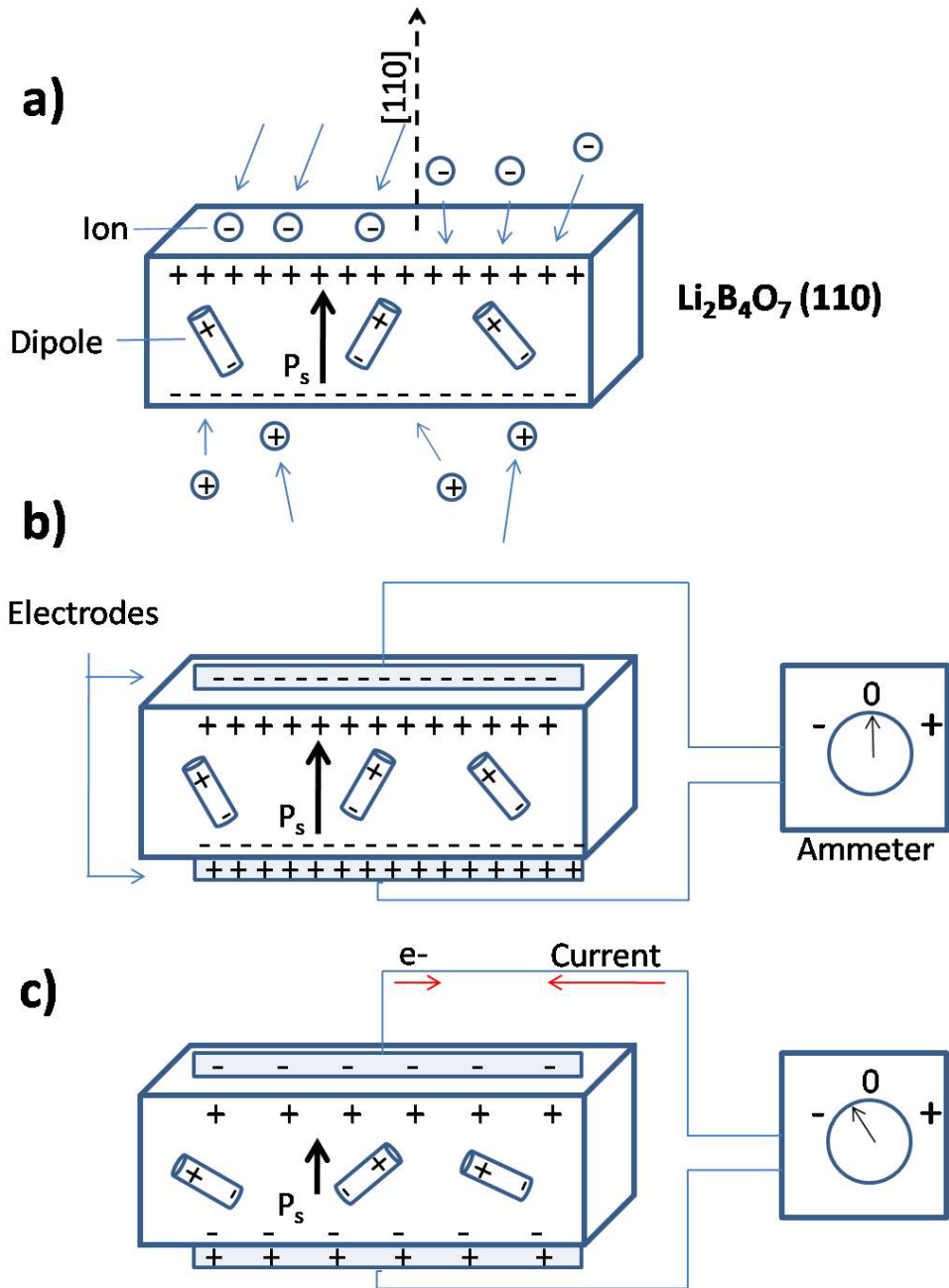
Figure 9.3. Schematic depicting pyroelectric measurement for $Li_2B_4O_7(110)$. a) prior to attaching electrodes, the sample possess an intrinsic dipole moment—even orthogonal to the historic dipole direction of [001]; **b)** sample with attached electrodes but with no change in temperature yields no pyroelectric current; and **c)** a sample that raises the temperature which leads to a decrease in the spontaneous polarization (P_s) due to the average decreasing magnitude of the dipole moments as indicated by their tilting. The created current flow compensates for this decrease and one sees a negative current. This figure is abstracted from works of Bhalla et al [1, 10, 18].

155

Although [110] is orthogonal to the dipole direction of [001], and $Li_2B_4O_7$ certainly does not exhibit a strong polarization, the principles remain as depicted in Figure 9.3. Along the direction of interest, [110] for example, polarization is non-zero, which is the equivalent of a bound surface charge despite the absence of an applied electric field. Following Lang's scheme [1], we see this in Figure 9.3(a). Assuming (initially) constant temperature, conductive electrodes are connected to a low resistance ammeter (Figure 9.3(b)). There would not be an expected change in current without a change in temperature. However, as the temperature is increased, the dipole moment is expected to decrease along [001] and increase along [110] in this material. The subsequent spontaneous polarization, in the [110] direction, and amount of bound charge would increase. The pyroelectric current is actually this redistribution of bound charge, which we only see as the temperature is changing; in this case a negative current. By cooling the sample, we would expect to see, and do so in Figure 9.3(c), just the opposite (a positive current), because of a decreased dipole moment along [110] and an increase along [001]; leading to an increase in bound charge along [001]. This produces a positive current via the redistribution of bound charge, along [001].

9.4. Off-Axis Pyroelectricity

A series of pyroelectric current measurements, were taken along the [110] direction in the absence of illumination. A generally negative current with increasing temperature and a mirror positive current with decreasing temperature, in the region of 70 K to 250 K, was observed. This is the same temperature region where the greatest

156

pyroelectric currents were measured in prior studies [10, 11] along the polar [001] direction, although the current measured here is along an orthogonal direction.

From the current and rate of change in temperature [2-4, 10, 11], we can extract the approximate pyroelectric coefficient along the [110] direction using Equation (59). While along the polar [001] direction, the pyroelectric coefficient p_i is about 125 μC/m^2•K at 120 K [11], along [110] the pyroelectric coefficient p_i only reaches a maximal value of about 0.2 to 0.4 μC/m^2•K, as illustrated in Figure 9.4. This pyroelectric coefficient p_i along the [110] direction is some 300 to 1000 times smaller than the conventional pyroelectric coefficient measured along the polar [001] lithium borate crystallographic direction and remains qualitatively similar in temperature dependence for a currents measured from a range of heating and cooling rates.

As in some prior measurements [10], we found strong variations with temperature in the pyroelectric current and associated pyroelectric coefficient, as shown in Figure 9.4.
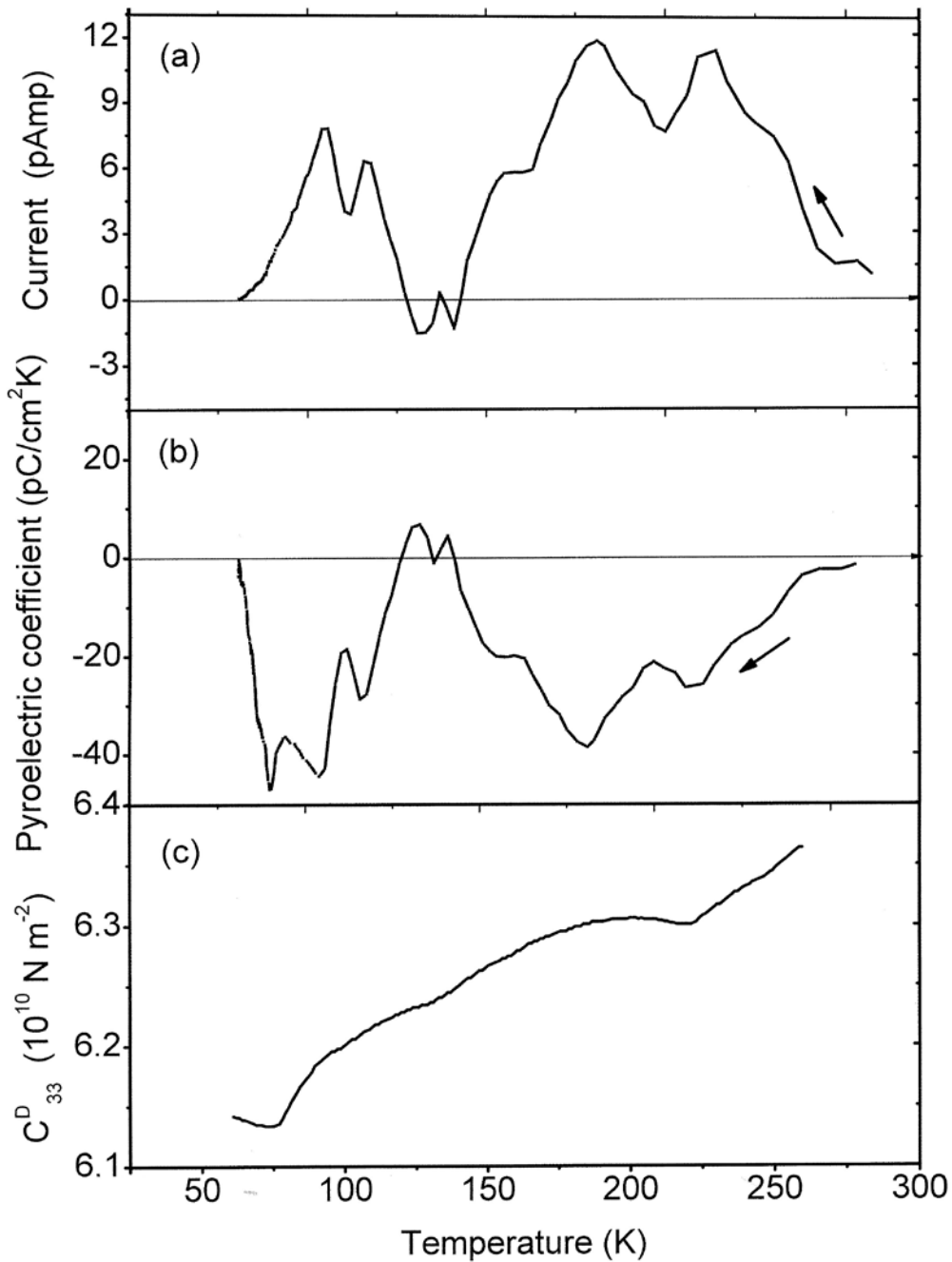
Figure 9.4. (a) Pyroelectric current in the cooling cycle for the $Li_2B_4O_7$ single crystal in the [110] direction, at a cooling rate of roughly 0.25°/sec; (b) temperature dependence of the pyroelectric coefficient in the cooling cycle for the $Li_2B_4O_7$ single crystal in the [110] direction; (c) temperature dependence of the elastic stiffness constant CD_{33} for the $Li_2B_4O_7$ single crystal along the polar c-axis, adapted from [19].

158

Indeed, the pyroelectric coefficient does not exhibit the same temperature dependence along the [110] direction as has been described [10, 11] along the [001] direction. The fact that the measured pyroelectric currents and resulting pyroelectric coefficients along the [110] direction differ qualitatively from those measured along to the [001] polar direction [11] is further compelling evidence that our measured pyroelectric coefficient is not simply a result a crystal miscut and therefore not a simple projection of the expected [001] pyroelectric current off the polar axis.

The pyroelectric current's dependence upon temperature results in dramatic relative changes in the pyroelectric coefficient along the [110] direction with temperature. There are large decreases in the magnitude of the off-axis pyroelectric coefficient at about 80 K, 130 K and 240 K (Figure 9.4(b)). These temperatures are close to the observed anomalies (Figure 9.4(c)) in the elastic stiffness observed at 75, 125 and 215 K [19]. While the elastic constant C_{33}^{D} decreases with decreasing temperature, reaching a minimum at about 75 K, these anomalies in the elasticity have been observed not only along the polar [001] direction, but also along other crystallographic directions, although of significantly smaller magnitude [19]. This qualitative agreement between the elastic constant anomalies and the magnitude of the off-axis pyroelectric coefficient suggests that the nonzero pyroelectric coefficient observed along the [110] direction is a result of anharmonic dipole oscillations or asymmetric dipole canting. The off-axis pyroelectric coefficient effect would not be expected to be as significant when the lattice is particularly soft, as may occur in the temperature regions near the elastic stiffness anomalies observed at 75, 125 and 215 K [19]. This is not unexpected for a secondary

159

pyroelectric effect, where temperature dependent crystal lattice deformations are permitted to occur.

9.5. Surface Piezoelectric Effects

While not all piezoelectric crystals are pyroelectrics, piezoelectric behavior is a requirement for pyroelectricity [2, 3], as noted at the outset of this chapter. If there is a surface electric field, one might be able to observe a surface pyroelectric effect. This measurement is not possible using traditional transport measurements but could be observed in photoemission by exploiting the surface photovoltage effect [20-24]. These measurements cannot be directly compared with the pyroelectric measurements (Figure 9.4), as illumination is required and such surface photovoltage measurements would tend to work best for a lithium borate surface that is largely defect free [25], as appears to be the case for the (110) surface. Using wave vector dependent inverse photoemission as discussed in Chapter 4, we have observed a highly dispersive image potential state for the (110) surface, the results of which were addressed in Chapters 5 and 7. These results tend to be characteristic of largely defect free surface as discussed previously [26].

At 623 K, where surface photovoltage charging was found to be negligible, both $Li_2B_4O_7(100)$ and $Li_2B_4O_7(110)$ exhibit a density of states that qualitatively resembles that expected from the model bulk band structure of $Li_2B_4O_7$ [27, 28] as discussed in detail in Chapter 6. The highlights are presented in the inset to Figure 9.5, where the valence band maximum is in reasonable agreement with prior investigations [16, 17, 28].
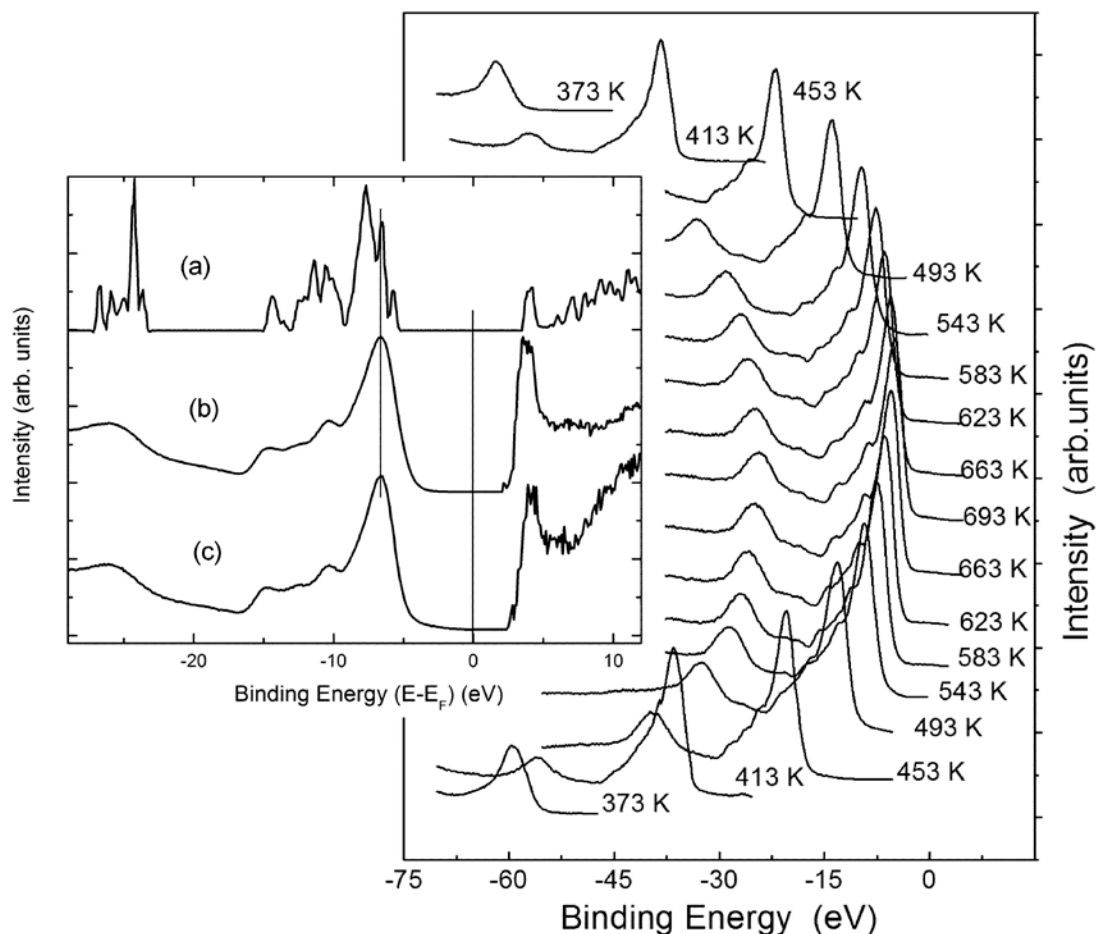
160

Figure 9.5. The photoemission spectra from $Li_2B_4O_7$(110) surface for a succession of temperatures in a heating-cooling cycle (from bottom to top). In the inset, the combined experimental photoemission and inverse photoemission results for bulk $Li_2B_4O_7$ taken at 623 K are compared with theory: (a) the theoretical density of states of solid $Li_2B_4O_7$ abstracted from the work of Islam et al. [28]; (b) combined experimental photoemission and inverse photoemission results for $Li_2B_4O_7$(110) surface, taken with the in-plane $\underline{E}$ vector oriented along [1$\underline{1}$0], and (c) $Li_2B_4O_7$(100) surface, taken with the in-plane $\underline{E}$ vector oriented along [011]. The photoemission spectra were taken at a photon energy of 56 eV with electrons collected along the surface normal, while the inverse photoemission was taken with electrons incident normal to the sample.

Lithium tetraborate is a dielectric [11], so that decreasing the temperature below 600 K

increases the photovoltaic charging. This in turn leads to an increase in the apparent

binding energies, as shown in Figure 9.5. The shifts in the photoemission spectra along

161

the binding energy scale, due to surface charging, are temperature dependent and demonstrate hysteretic behavior in the heating-cooling cycles, as also indicated in Figure 9.5.

In the region of 600 K, there is a huge increase in the absolute magnitude of the current with increasing temperature and a huge decrease in current with decreasing temperature. These current changes in the region of 600 K are likely the result of trapped charges being freed or charge trapping, with the onset of increasing or decreasing conductivity, respectively, as indicated in Figure 9.6, and may have little to do with the more conventional pyroelectric effect. Below 500 K, the surface photo-voltaic charging is both temperature and time dependent, particularly at the (110) surface.

The measured effective binding energy, for the oxygen 2s at -26.0 ± 0.6 eV binding energy (E-E$_F$) at 623 ± 5 K (Figure 9.6), shows a strong decrease following an increase in temperature, below 600 K.
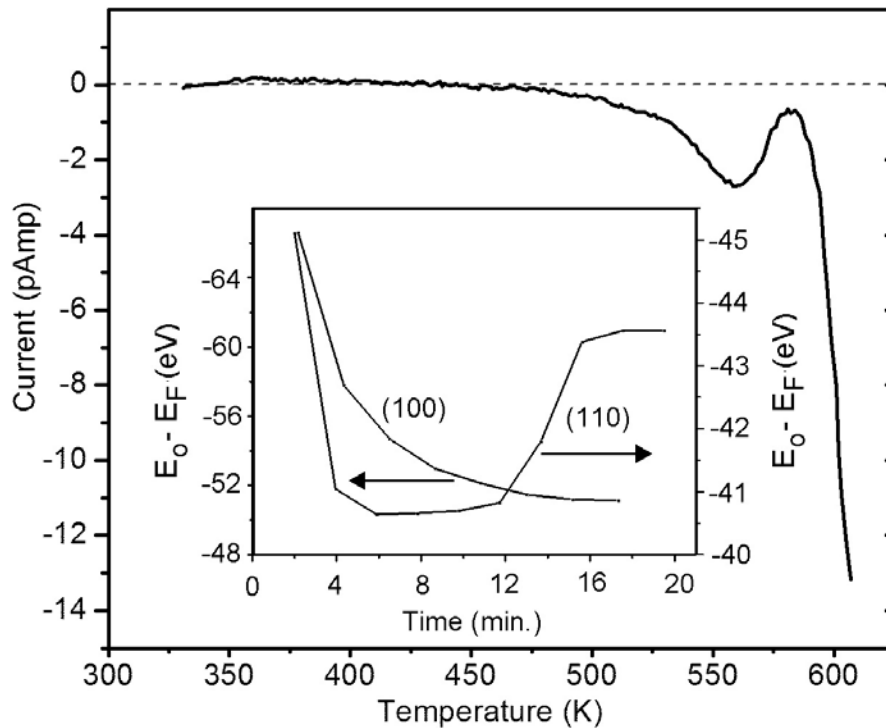
Figure 9.6. Increase in the current magnitude, due to trapped charges, in the [110] direction of lithium tetraborate single crystal with increasing temperature in the region of 600 K. In the inset, change of the magnitude of the apparent O 2s binding energy, with time, indicative of the surface photovoltaic charging of the $Li_2B_4O_7(110)$ surface following a temperature increase to 390 K compared to the $Li_2B_4O_7$ (100) surface following a temperature increase to 420 K.

At temperatures below 500 K, using the oxygen 2s shallow core as a benchmark, this

observed decrease in binding energy (and associated photovoltaic charging) can be

understood as establishment of a steady state surface temperature and surface

conductivity. At the (110) surface, there is not only a decrease in binding energy, but this

is followed by a increase in binding energy later in time, as plotted in Figure 9.6. This

latter increase in binding energy later in time is observed at the (110) but not the (100)

surface (Figure 9.6) and this time dependent hysteresis effect is increasingly more evident

at lower temperatures. This occurs in a region where there is little or no bulk current,

163

pyroelectric or otherwise, with changes in temperature (Figure 9.6). This effect suggests that while the surface photovoltage effect is initially dominated by the establishment of a steady state surface temperature and surface conductivity, the surface charge density D_i is later altered by the local electric field resulting from the surface photovoltage effect. In other words, at the (110) surface, there are changes in surface charge density D_i by applying an electric field.

While this time dependent hysteresis is likely a result of a surface piezoelectric effect, this surface piezoelectric effect does not exclude the possibility of a surface pyroelectric effect. Further evidence to support its existence is found in Figure 9.7:

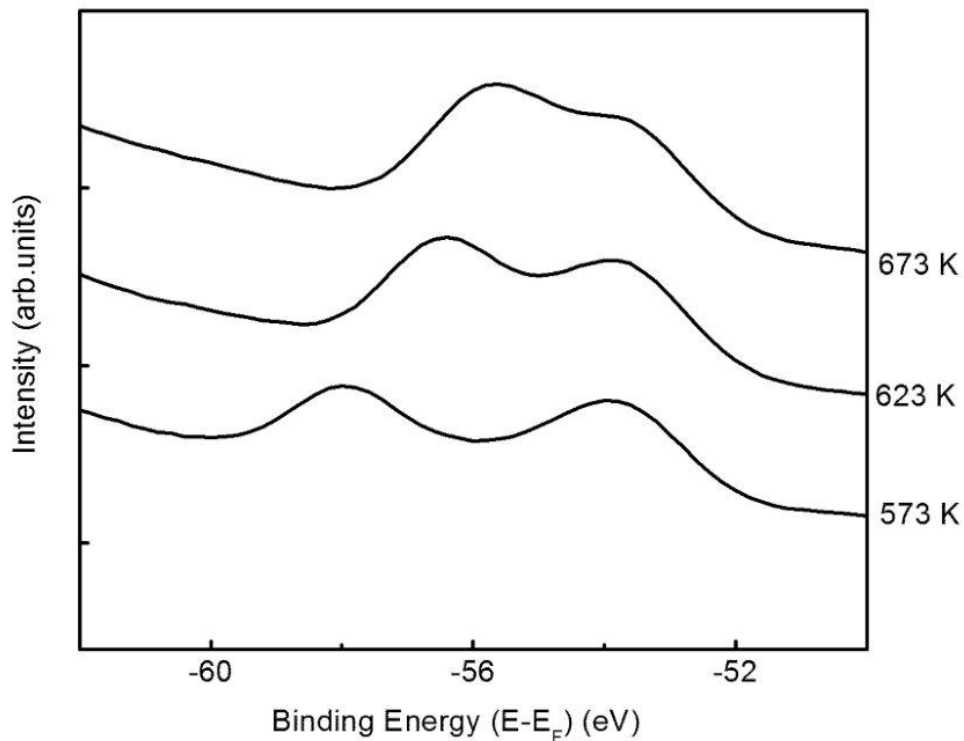**Figure 9.7. Li 1s surface-to-bulk core level shift for $Li_2B_4O_7$(110) for three different temperatures. The in-plane component of $\underline{E}$ was oriented along [001] with a light incidence angle 45 degrees; the surface normal at 0° with respect to analyzer; and photon energy of 95 eV. The bulk (left) and surface (right) contributions are different for all three temperatures.**

164

Figure 9.7 shows the shift in the Li 1s core with temperature that affects the bulk significantly more than the surface. This is additional evidence that there is a compensating surface charge in the region of 623 K that is not present at the bulk. This, further supports the contention that there may well be a surface piezoelectric if not a surface pyroelectric effect along the $Li_2B_4O_7(110)$ direction. Certainly the surface piezoelectric effect does occur at some (but not all) surfaces perpendicular to the direction of spontaneous polarization for lithium tetraborate, as shown from the surface photovoltage effect (Figure 9.6). This adds credence to the idea [2] that the pyroelectric coefficients, p_i, that include the secondary pyroelectric effect likely have some tensor character and would probably be more accurately expressed as a third order tensor p_{ijk}.

9.6. Concluding Remarks

Additional attributes of lithium tetraborate are presented in this chapter that do not directly support the main thrust of the motivation as delineated in Chapter 2; but certainly of some interest in a solid-state physics sense. By presenting results that indicate a time dependent hysteretic effect, as well as results that indicate pyroelectric as well as piezoelectric effects, one can surmise that $Li_2B_4O_7$ along the [110] direction possesses a non-zero, off-axis pyroelectric coefficient. All of these effects support the concept that the pyroelectric coefficients, p_i, and the piezoelectric coefficients likely have some tensor character, so that the former should more accurately be expressed as p_{ijk}.

What is of vital importance in this chapter according to the Chapter 2 motivation is that a pyroelectric effect and inverse surface pyroelectric effect do exist, and could be either an advantage or disadvantage to a potential device incorporating $Li_2B_4O_7(110)$.

The advantage is that a device would experience an increased gain due to the enhanced **E**. However, there is also a disadvantage. The presence of inverse surface piezoelectric effect would mechanically change the physical dimensions the crystal to some degree, a generally undesirable effect in a potential device. Both of these attributes need to be carefully quantified in future studies, and were outside the scope of this particular research. Finally, the ability to do these measurements indicates successful contacts being manufactured for this material; an important milestone as will be addressed in the final chapter.

9.7. References

1. S. B. Lang, "Pyroelectricity: From Ancient Curiosity to Modern Imaging Tool," Phys Today **58,** 31-36 (2005).

2. J. F. Nye, "Thermodynamics of Equilibrium Properties of Crystals," in *Physical Properties of Crystals,* (Oxford University Press, 1985), pp. 171-191.

3. D. Damjanovic, "Ferroelectric, dielectric an piezoelectric properties of ferroelctric thin films and ceramics," Rep. Prog. Phys. **61,** 1267-1324 (1998).

4. C. G. Wu, W. L. Zhang, Y. R. Li, Z. Liu, and J. Zhu, "Measurement of Induced Pyroelectric Coefficient Using Dynamic Method: Theory and Experiments," Jap. J. Appl. Phys. **45,** 2674-2677 (2006).

5. S. Keith, "Chapter 10," in *Mechanics,* (Addison-Wesley, 1971).

6. V. Y. Shur, A. L. Gruverman, and S. B. Zalyuk, *Ferroelectrics and Piezoelectrics* (1989).

7. J. Krogh-Moe, "Refinement of the crystal structure of lithium diborate $Li_2O.2B_2O_3$," Acta Crystallographica Section B **24,** 179-181 (1968).

8. J. Krogh-Moe, "The crystal structure of lithium diborate, $Li_2O.2B_2O_3$," Acta Crystallogr. **15,** 190-193 (1962).

9. M. Natarajan, R. Faggiani, and I. O. Brown, "Dilithium tetraborate $Li_2B_4O_7$," Cryst. Struct. Commun. **8,** (1979).

10. Y. V. Burak, "Pyroelectroluminescence and its influence on the structure investigation in the $Li_2B_4O_7$ crystals," J. Phys. Studies **2,** 62 (1998).

11. A. S. Bhalla, L. E. Cross, and R. W. Whatmore, "Pyroelectric and Piezoelectric Properties of Lithium Tetraborate Single Crystal," Japanese Journal of Applied Physics **24S2,** 727-729 (1985).

12. Y. Losovyj, I. Ketsman, E. Morikawa, Z. Wang, J. Tang, and P. Dowben, "Optimization of the 3m TGM beamline, at CAMD, for constant initial state spectroscopy," Nucl. Instrum. Methods Phys. Res. A **582,** 264 (2007).

13. P. A. Dowben, D. LaGraffe, and M. Onellion, "Final-state symmetry effects in photoemission of thin Gd overlayers," J. Phys. Cond. Matter **1,** 6571-6587 (1989).

14. J. Hormes, J. D. Scott, and V. P. Suller, "Facility Update: The Center for Advanced Microstructures and Devices: A Status Report," Synchrotron Radiation News **19,** 27 (2006).

15. D. Wooten, I. Ketsman, J. Xiao, Y. B. Losovyj, J. Petrosky, J. McClory, Y. Burak, V. Adamiv, and P. A. Dowben, "Differences in the Surface Charging at the (100) and (110) Surfaces of $Li_2B_4O_7$ in *Nuclear Radiation Detection Materials — 2009,*" in *Nuclear Radiation Detection Materials — 2009,* D. L. Perry, A. Burger, L. Franks, K. Yasuda, and M. Fiederle, eds. (MRS, 2009), pp. 1164-L04-04.

16. D. Wooten, I. Ketsman, J. Xiao, Y. B. Losovyj, J. Petrosky, J. McClory, Y. V. Burak, V. T. Adamiv, and P. A. Dowbenb, "The Surface Core Level Shift for Lithium at the Surface of Lithium Borate," Phys. B Cond. Mat. (2009).
17. A. Y. Kuznetsov, A. V. Kruzhalov, I. N. Ogorodnikov, A. B. Sobolev, and L. I. Isaenko, "Electronic structure of lithium tetraborate $Li_2B_4O_7$ crystals. Cluster calculations and x-ray photoelectron spectroscopy," Phys. Solid State **41,** 48 (1999).

18. A. S. Bhalla, L. E. Cross, and R. W. Whatmore, "Pyroelectric and Piezoelectric Properties of Lithium Tetraborate Single Crystal," Jpn. J. Appl. Phys. **24 Supplement,** 727-729 (1985).

19. A. A. Sehery and D. J. Somerford, "Low-temperature elastic anomalies in lithium tetraborate," Journal of Physics: Condensed Matter **1,** 2279-2281 (1989).

20. W. H. Brattain and J. Bardeen, Bell Syst. Tech. J. **32,** 1-41 (1953).

21. D. K. Schroder, "Surface voltage and surface photovoltage: history, theory and applications," Measurement Science and Technology **12,** R16-R31 (2001).

22. J. E. Demuth, W. J. Thompson, N. J. DiNardo, and R. Imbihl, "Photoemission-Based Photovoltage Probe of Semiconductor Surface and Interface Electronic Structure," Physical Review Letters **56,** 1408-1411 (1986).

23. M. Alonso, R. Cimino, and K. Horn, "Surface photovoltage effects in photoemission from metal-GaP(110) interfaces: Importance for band bending evaluation," Physical Review Letters **64,** 1947-1950 (1990).

24. K. Stiles and A. Kahn, "Correlation between E_F pinning and development of metallic character in Ag overlayers on GaAs(110)," Physical Review Letters **60,** 440-443 (1988).

25. C. Kim, J. Park, B. K. Moon, H. Seo, B. Choi, Y. Hwang, H. K. Kim, and J. N. Kim, "ac conductance of surface layer in lithium tetraborate single crystals," J. Appl. Phys. **94,** 7246-7249 (2003).

26. N. V. Smith, "Inverse Photoemission," Rept. Prog. Phys. **51,** 1227-1294 (1988).

27. V. T. Adamiv, Y. B. Burak, I. V. Kityk, J. Kasperczyk, R. Smok, and M. Czerwinski, "Nonlinear optical properties of $Li_2B_4O_7$ single crystals doped with potassium and silver," Opt. Mater. **8,** 207-213 (1997).

28. M. M. Islam, V. V. Maslyuk, T. Bredow, and C. Minot, "Structural and Electronic Properties of $Li_2B_4O_7$," J. Phys. Chem. B **109,** 13597-13604 (2005).

168

10. Conclusion

10.1.   Overview

In this chapter, I present an overall summary of the major findings for the $Li_2B_4O_7(110)$ and (100) band mapping research, as well as a recommendation for future work, which logically follows from this effort.

10.2.   Research Summary

First, in the process of finding an adequate reference point, we observed a previously undiscovered Li 1s surface to core level shift in the $Li_2B_4O_7(110)$ surface [1], which also explained the wide variation of previously published experimental and theoretical binding energies assignments for the Li 1s core [2-4].

After verifying the binding energies of the Li 1s and O 2s core levels, the band mapping of both the $Li_2B_4O_7(110)$ and $Li_2B_4O_7(100)$ surfaces was undertaken. The combined PES and AR-IPES spectra yielded experimental densities of states that qualitatively agrees with the theoretical results from model bulk band structure calculations for $Li_2B_4O_7$; albeit with a larger band gap than predicted [2-5], consistent with the known deficiencies of LDA and DFT calculations. $Li_2B_4O_7(110)$ yielded the more consistent values in orthogonal directions for band gap energies, indicative of a more stable surface [5].

After examining four different high symmetry directions, two for each of the surfaces, it was determined that the $Li_2B_4O_7(100)$ and $Li_2B_4O_7(110)$ occupied states were extremely flat; to the degree that resolving periodic dispersion of the occupied states was inconclusive, within the resolution of the system. However, both surfaces

169

demonstrated clear periodic dispersion within the empty states very close to theoretical Brillouin zone values. These attributes also translated to a lighter charge carrier effective mass in the unoccupied states. Of the two surfaces, $Li_2B_4O_7(110)$ yielded the more consistent values in orthogonal directions for energy states [6]. The presence of a bulk band gap surface state and image potential state in $Li_2B_4O_7(110)$ was indicative of a defect-free surface. The absence of both in the more polar, more dielectric $Li_2B_4O_7(100)$ was attributed to the presence of defects determined to be O vacancies [1, 6-8].

The pyroelectric and piezoelectric character of $Li_2B_4O_7$ was explored more deeply; with the determination that $Li_2B_4O_7$ along the [110] direction possessed a non-zero, off-axis pyroelectric coefficient [9]. Further, the fact that measurements of this nature were conducted indicated successful contacts could be produced on the $Li_2B_4O_7(110)$ surface; a critical step to eventually manufacturing a solid state device.

From the overall perspective of $Li_2B_4O_7$ solid state device incorporation, several attributes are worth summarizing: One is qualitatively confident in the various modeling programs ability to provide density of state estimates. Due to the measured large band gap (9-10 eV), only by doping will this material be of efficient use in a detector. The determined HOMO and LUMO effective mass measurements can now be used as inputs for various semiconductor modeling programs in order to optimize the various dopants that will be have to be explored. Of the two surfaces studied in this research, $Li_2B_4O_7(110)$ is the flatter, more stable, more ordered, less polar surface and will be more efficient as a detector material in multiple directions. As discussed at the end of Chapter 9, the observation of off-axis pyroelectric and surface piezoelectric effects will require

further study to determine if the enhanced **E** advantage outweighs the adverse mechanical effect.

10.3. Future Work

If this material is to be optimally incorporated in a future solid state device, considerable work remains to be done. First, it is important to properly characterize the charge mobility of this material. Effective masses of the charge carriers at the HOMO and LUMO have been determined, and will be helpful for various modeling programs. However, to truly determine the actual charge mobility, I recommend conducting Hall measurements on $Li_2B_4O_7(110)$ similar to those outlined for any standard material [10]. Since contacts on both the $Li_2B_4O_7(110)$ and $Li_2B_4O_7(100)$ are now a reality, this measurement is possible. In essence, one would find the point where the transverse Hall field (E_y) cancels the Lorentzian force through a material, produced by a known current (j_x) through a known perpendicular magnetic field (B), thus providing the Hall coefficient (R_{Hall}) [11]:

$$\frac{E_y}{j_x B} = R_{Hall} = \frac{-1}{ne},$$
(60)

where e is the electron charge and n is the charge carrier concentration. (Equation 60 assumes the same relaxation times and only one charge carrier-electrons that are independent of velocity.) The overarching goal would be to seek the charge carrier concentration, n.

With the electron and hole charge carrier concentrations (n_e and n_p), one could then estimate the electrical conductivity [12]:

171

$$\sigma = n_e e \mu_e + n_p e \mu_p, \qquad\qquad (61)$$

with the electron and hole mobilities (μ_e, μ_p) already estimated based on effective mass as discussed in this research (Chapter 8).

This should be done to understand the baseline before adding any dopants to the material. Given its high resistivity [13] and large band gap [6], doping the crystal will be essential and the next logical step. Fortunately, this material has already been doped with various materials; K, Ag [4, 14], Cu [15, 16], Yb, Co and Mn [17, 18] to name a few.

We have already accomplished some proof of concept work with Cu doped $Li_2B_4O_7$ that indicates a mobility times charge carrier lifetime product much larger than that of undoped $Li_2B_4O_7$ [16]. From previous work, we know that electron life-times are increased in $Cu:Li_2B_4O_7$ as opposed to $Li_2B_4O_7$ [19], which gives rise to the possibility of an increase in surface and, possibly bulk conductivity with copper doping [16]. This increased surface conductivity can be observed in Figure 10.1, where the binding energies of the valence band maximum have been plotted versus temperature.
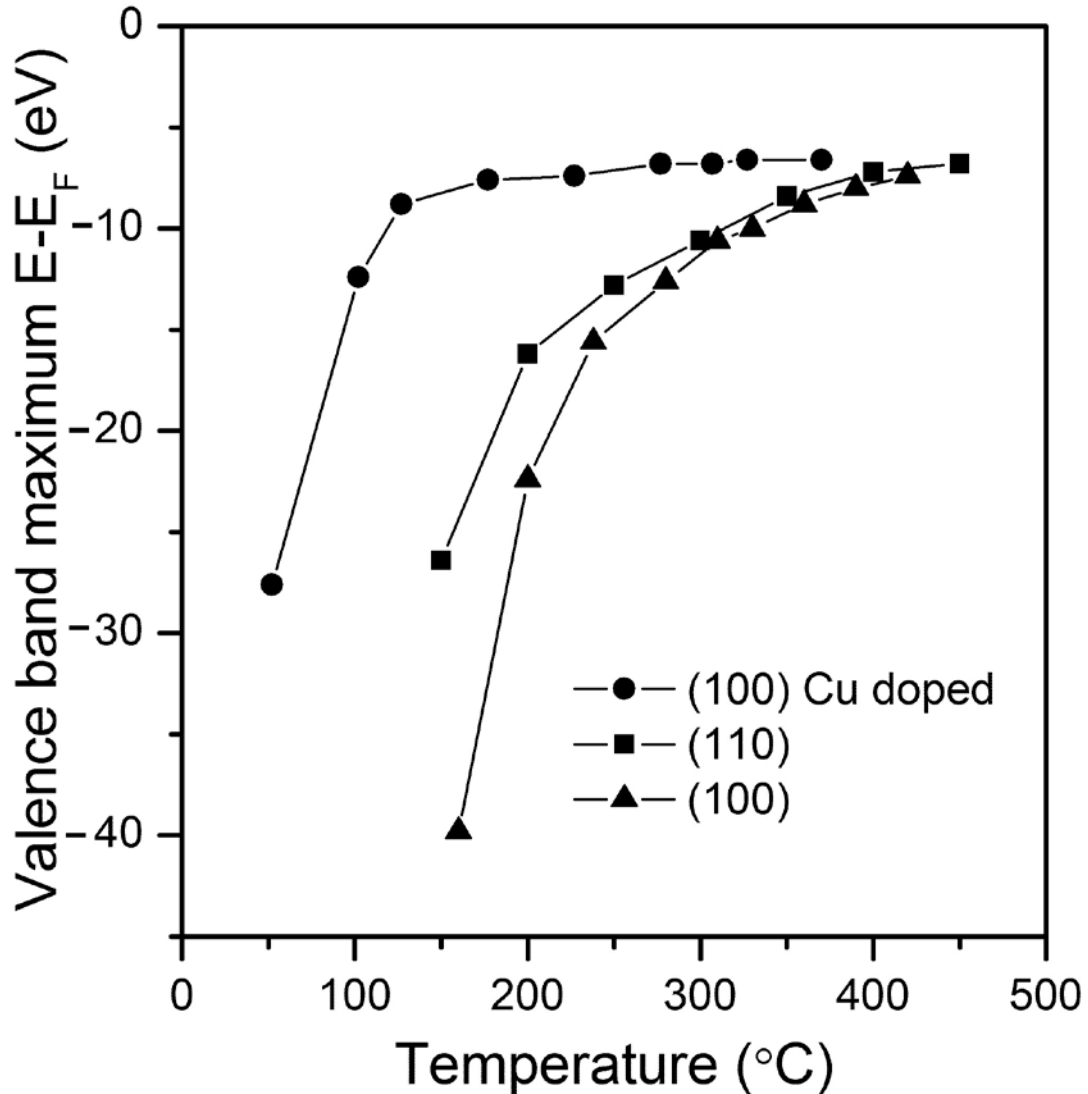
Figure 10.1. Position of the apparent valence band maximum for both the (110) and (100) surfaces of undoped $Li_2B_4O_7$, as well as Cu doped $Li_2B_4O_7(100)$, as a function of temperature. The data was obtained from photoemission spectra taken at a photon energy of 90 eV, with the photoelectrons collected normal to the surface [16].

The shift in the valence band maximum is much greater for $Li_2B_4O_7(100)$ than for

$Li_2B_4O_7(110)$, but significantly reduced with Cu doping of $Li_2B_4O_7(100)$. In many such

cases, the surface voltaic charging can be dominated by surface conductivity. The

decreased charging observed for the Cu doped $Li_2B_4O_7(100)$ surface over the nominally

173

undoped $Li_2B_4O_7(100)$ and $Li_2B_4O_7(110)$ surfaces is consistent with the unoccupied

density of states that tails off towards the Fermi level, indicating a persistent presence of

donor states. This may well be due to the Cu doping [16].

The surface photovoltaic charging for both Cu doped and undoped $Li_2B_4O_7(100)$

surfaces exhibits similar dependence on temperature but is shifted in temperature by

130°. The trend in the temperature dependence for the doped and undoped $Li_2B_4O_7(100)$

surfaces, shown in Figure 10.1, differs from the temperature dependence shown for the

undoped $Li_2B_4O_7(110)$ surfaces. This suggests that it is the carrier concentration that is

altered with Cu doping, not the surface termination. Ultimately, this attribute would

mean a better charge sweep out and improved device performance for Cu doped $Li_2B_4O_7$

in contrast to undoped $Li_2B_4O_7$; a highly desired characteristic of a future solid state

device [16].

Given that the next step in the research will be to test this doped material in a

neutron environment, one should use caution in selecting any dopant material that will be

easily activated and cause an intrinsic background error or potential hazard. The example

given for Cu (above) has some isotopes that meet these criteria. Following successful

doping of the material, the same initial steps must then be repeated, conduct Hall

measurements and obtain carrier concentrations and mobility values.

The next step will be to characterize this doped material in a neutron environment.

As demonstrated conceptually in Figure 10.2 for undoped $Li_2B_4O_7$ [20], and elsewhere

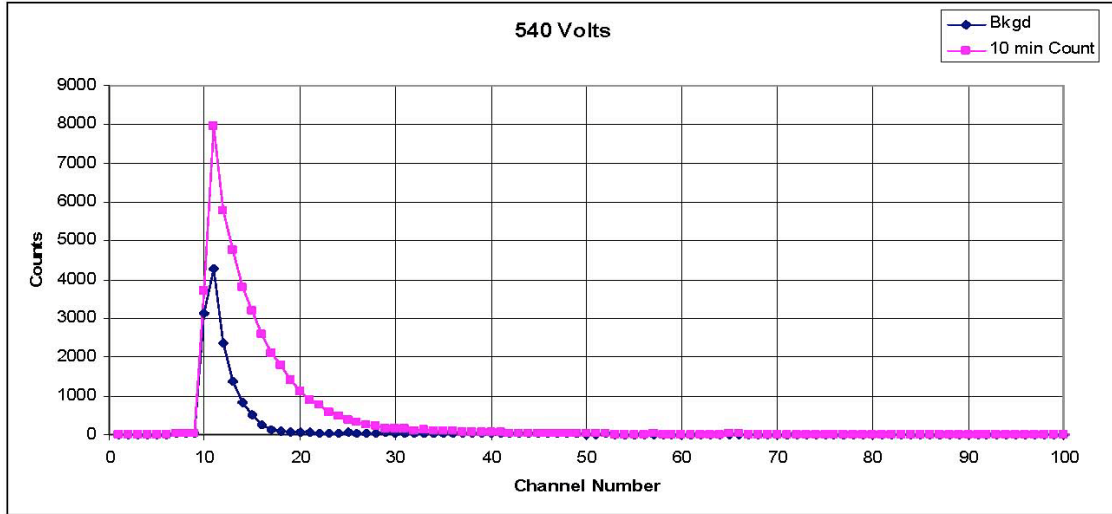[13, 21-23], this material shows considerable promise for neutron detection.

174

Figure 10.2. n counts of undoped $Li_2B_4O_7$ crystal that was placed in the radial neutron beam of the TRIGA Mark II nuclear reactor. The reactor power was set to 100 kW (approximately 10^6 n/cm^2-s).   Because the mobility of the carriers or what type of charge carrier was dominant in the crystal was unknown, both positive and negative biases were used during testing procedures. The shutter to the beam was opened and the operating bias was increased positively until pulses were observed; the same was done for the negative bias. Once operating biases were obtained, 10 minute radiation measurements and 10 minute background measurements were obtained using a multi-channel analyzer [20].

It would be expected that the doped $Li_2B_4O_7$ crystal would be considerably more efficient.

After fully characterizing this material, the same should be done with the Gd oxide that is chosen to accompany this material as discussed in Chapter 2. After making a successful *p-n* junction or *p-i-n* trilayer diode as planned [24], this new combined solid state device must again be characterized in the same neutron environments.

Finally, after fabricating one such device, a reasonable estimate of the energy of the initial neutron can be made by layering a series of the same type of semiconductors described previously that are collimated and between (neutron) transparent material;

175

which has been proposed in a provisional patent [25]. One could then estimate a clear direction of the neutron source by arraying three sets of these same series of collimated semiconductors in three orthogonal directions. For the characterization of this final device, it would be important to use different sources (with different neutron energies) at different directions and distances to ensure a correct reference baseline.

10.4. References

1. D. Wooten, I. Ketsman, J. Xiao, Y. B. Losovyj, J. Petrosky, J. McClory, Y. V. Burak, V. T. Adamiv, and P. A. Dowbenb, "The Surface Core Level Shift for Lithium at the Surface of Lithium Borate," Phys. B Cond. Mat. (2010).

2. A. Kuznetsov, A. Kruzhalov, I. Ogorodnikov, A. Sobolev, and L. Isaenko, "Electronic structure of lithium tetraborate $Li_2B_4O_7$ crystals. Cluster calculations and x-ray photoelectron spectroscopy," Physics of the Solid State **41,** 48-50 (1999).

3. M. M. Islam, V. V. Maslyuk, T. Bredow, and C. Minot, "Structural and Electronic Properties of $Li_2B_4O_7$," J. Phys. Chem. B **109,** 13597-13604 (2005).

4. V. T. Adamiv, Y. B. Burak, I. V. Kityk, J. Kasperczyk, R. Smok, and M. Czerwinski, "Nonlinear optical properties of $Li_2B_4O_7$ single crystals doped with potassium and silver," Opt. Mater. **8,** 207-213 (1997).

5. D. Wooten, Y. B. Losovyj, J. Petrosky, J. McClory, J. Tang, W. Wang, and P. A. Dowben, "Surface charging of n-type Gd_2O_3 and HfO_2 thin films in *Rare-Earth Doping of Advanced Materials for Photonic Applications--2008* ," in (, 2008), pp. D07.

6. D. Wooten, I. Ketsman, J. Xiao, Y. B. Losovyj, J. Petrosky, J. McClory, Y. V. Burak, V. T. Adamiv, R. Hengehold, and P. A. Dowben, "Electronic Structure of $Li_2B_4O_7(110)$ and $Li_2B_4O_7(100)$ (in preparation)," (2009).

7. D. Wooten, I. Ketsman, J. Xiao, Y. B. Losovyj, J. Petrosky, J. McClory, Y. Burak, V. Adamiv, and P. A. Dowben, "Differences in the Surface Charging at the (100) and (110) Surfaces of $Li_2B_4O_7$ in *Nuclear Radiation Detection Materials — 2009*," in *Nuclear Radiation Detection Materials — 2009,* D. L. Perry, A. Burger, L. Franks, K. Yasuda, and M. Fiederle, eds. (MRS, 2009), pp. 1164-L04-04.

8. M. W. Swinney, J. W. McClory, J. C. Petrosky, Y. V. Burak, S. Yang, A. T. Brant, and L. E. Halliburton, "Identification of electron and hole traps in lithium tetraborate $(Li_2B_4O_7)$ crystals: Oxygen vacancies and lithium vacancies," Journal of Applied Physics (submitted for publication).

9. I. Ketsman, D. Wooten, J. Xiao, Y. B. Losovyj, Y. V. Burak, V. T. Adamiv, A. Sokolov, J. Petrosky, J. McClory, and P. A. Dowben, "The off-axis pyroelectric effect observed for lithium tetraborate," APL (2010).

10. Electronics and Electrical Engineering Laboratory, "Resistivity and Hall Measurements," .

11. C. Kittel, "Free Electron Fermi Gas," in *Introduction to Solid State Physics,* (John Wiley & Sons, Inc., 2005), pp. 152-156.

12. C. Kittel, "Semiconductor Crystals," in *Introduction to Solid State Physics,* (John Wiley & Sons, Inc., 2005), pp. 187-208.

13. Sangeeta, K. Chennakesavulu, D. G. Desai, S. C. Sabharwal, M. Alex, and M. D. Ghodgaonkar, "Neutron flux measurements with a $Li_2B_4O_7$ crystal," Nuclear Instruments and Methods in Physics Research Section A: Accelerators, Spectrometers, Detectors and Associated Equipment, **571,** 699-703 (2007).

14. V. T. Adamiv, Y. V. Burak, and I. M. Teslyuk, "Growth and properties of new nonlinear $LiKB_4O_7$ single crystals," Journal of Crystal Growth **289,** 157-160 (2006).

15. V. M. Holovey, V. I. Sidey, V. I. Lyamayev, and P. P. Puga, "Influence of reducing annealing on the luminescent properties of $Li_2B_4O_7$:Cu single crystals," Journal of Luminescence, **126,** 408-412 (2007).

16. J. Xiao, N. Lozova, Y. B. Losovyj, D. Wooten, I. Ketsman, M. W. Swinney, J. Petrosky, J. McClory, Y. V. Burak, V. T. Adamiv, A. T. Brant, and P. A. Dowben, "Surface Charing at the (100) Surface of Cu doped and undoped $Li_2B_4O_7$," Appl. Surf. Sci. (2010).

17. D. Podgórska, S. M. Kaczmarek, W. Drozdowski, M. Berkowski, and A. Worsztynowicz, "Growth and Optical Properties of $Li_2B_4O_7$ Single Crystals Pure and Doped with Yb, Co and Mn Ions for Nonlinear Applications," Acta Physica Polonica A **107,** 507 (2005).

18. D. Piwowarska, S. Kaczmarek, and M. Berkoski, "Growth and characterization of pure and Co2+ doped $Li_2B_4O_7$ single crystals," Cryst. Res. Technol. **42,** 1329 (2007).

19. V. T. Adamiv, V. P. Savchyn, P. V. Savchyn, I. M. Teslyuk, and T. V. Burak, Functional Mat. **16,** (2009).

20. K. Nelson, B. Montag, D. McGregor, and I. Ketsman, "Preliminary pulse counting demonstration using undoped $Li_2B_4O_7$," (2009).

177

21. Y. V. Burak, B. V. Padlyak, and V. M. Shevel, "Neutron-Induced Defects in the Lithium Tetraborate Single Crystals," Radiation Effects & Defects in Solids **157,** 1101-1109 (2002).

22. Y. V. Burak, B. V. Padlyak, and V. M. Shevel, "Radiation-induced centers in the $Li_2B_4O_7$ single crystals," Nuclear Instruments and Methods in Physics Research Section B: Beam Interactions with Materials and Atoms, **191,** 633-637 (2002).

23. Y. V. Burak, V. T. Adamiv, I. M. Teslyuk, and V. M. Shevel, "Optical absorption of isotopically enriched $Li_2B_4O_7$ single crystals irradiated by thermal neutrons," Radiat. Measure. **38,** 681-684 (2004).

24. P. Dowben, "DNDO Project Description (draft_14_edit_4-8-08v2)," (2008).

25. A. Caruso, J. Petrosky, J. McClory, and P. A. Dowben, "Gd-doped EuO Solid-state Neutron Detector," **61/274,753,** (2009).

REPORT DOCUMENTATION PAGE

Public reporting burden for this collection of information is estimated to average 1 hour per response, including the time for reviewing instructions, searching existing data sources, gathering and maintaining the data needed, and completing and reviewing this collection of information. Send comments regarding this burden estimate or any other aspect of this collection of information, including suggestions for reducing this burden to Department of Defense, Washington Headquarters Services, Directorate for Information Operations and Reports (0704-0188), 1215 Jefferson Davis Highway, Suite 1204, Arlington, VA 22202-4302. Respondents should be aware that notwithstanding any other provision of law, no person shall be subject to any penalty for failing to comply with a collection of information if it does not display a currently valid OMB control number. **PLEASE DO NOT RETURN YOUR FORM TO THE ABOVE ADDRESS.**

1. REPORT DATE *(DD-MM-YYYY)* 17-06-2010	2. REPORT TYPE Doctoral Dissertation	3. DATES COVERED *(From - To)* March 2008 - June 2010

4. TITLE AND SUBTITLE
Electronic Structure of Lithium Tetraborate

5a. CONTRACT NUMBER

5b. GRANT NUMBER

5c. PROGRAM ELEMENT NUMBER

6. AUTHOR(S)

Wooten, David J., LTC, US Army

5d. PROJECT NUMBER
09155, 10130

5e. TASK NUMBER

5f. WORK UNIT NUMBER

7. PERFORMING ORGANIZATION NAME(S) AND ADDRESS(ES)

Air Force Institute of Technology
Graduate School of Engineering and Management (AFIT/EN)
2950 Hobson Way
WPAFB OH 45433-7765

8. PERFORMING ORGANIZATION REPORT NUMBER

AFIT/DS/ENP/10-J01

9. SPONSORING / MONITORING AGENCY NAME(S) AND ADDRESS(ES)
Defense Threat Reduction Agency
DTRA/CSU ATTN: COL Mark Mattox
1900 Wyoming Blvd SE
Kirtland AFB, NM 87117-5669

10. SPONSOR/MONITOR'S ACRONYM(S)

11. SPONSOR/MONITOR'S REPORT NUMBER(S)

12. DISTRIBUTION / AVAILABILITY STATEMENT

APPROVED FOR PUBLIC RELEASE; DISTRIBUTION UNLIMITED

14. ABSTRACT

Due to interest as neutron detection material, an investigation of $Li_2B_4O_7(110)$ and $Li_2B_4O_7(100)$ was undertaken, utilizing photoemission and inverse photoemission spectroscopic techniques. The measured band gap depended on crystallographic direction with the band gaps ranging from 8.9 ± 0.5 eV to 10.1 ± 0.5 eV. The measurement yielded a density of states that qualitatively agreed with the theoretical results from model bulk band structure calculations for $Li_2B_4O_7$; albeit with a larger band gap than predicted, but consistent with the known deficiencies of LDA and DFT calculations. The occupied states of both surfaces were extremely flat; to the degree that resolving periodic dispersion of the occupied states was inconclusive, within the resolution of the system. However, both surfaces demonstrated clear periodic dispersion within the empty states very close to theoretical Brillouin zone values. These attributes also translated to a lighter charge carrier effective mass in the unoccupied states. $Li_2B_4O_7(110)$ yielded the more consistent values in orthogonal directions for energy states. The presence of a bulk band gap surface state and image potential state in $Li_2B_4O_7(110)$ was indicative of a defect-free surface. The absence of both in the more polar, more dielectric $Li_2B_4O_7(100)$ was attributed to the presence of defects determined to be O vacancies. The results from $Li_2B_4O_7(110)$ were indicative of a more stable surface than $Li_2B_4O_7(100)$. In addition, Li 1s bulk and surface core level components were determined at the binding energies of -56.5 ± 0.4 and -53.7 ± 0.5 eV. Resonance features were observed along the [001] direction and were attributed to a Coster-Kronig process. The pyroelectric and piezoelectric character of $Li_2B_4O_7$ was explored more deeply and a non-zero, off-axis pyroelectric coefficient for the $Li_2B_4O_7(110)$ direction was discovered.

15. SUBJECT TERMS
$Li_2B_4O_7$, Experimental bandgap, electronic bandmap, charge carrier effective mass, off-axis pyroelectric effect, Li surface core level shift, surface state, image potential state, neutron detection material

16. SECURITY CLASSIFICATION OF:			17. LIMITATION OF ABSTRACT	18. NUMBER OF PAGES	19a. NAME OF RESPONSIBLE PERSON John W. McClory, LTC (PhD), (ENP)
a. REPORT U	**b. ABSTRACT** U	**c. THIS PAGE** U	UU	195	**19b. TELEPHONE NUMBER** *(include area code)* (937) 255-3636 ext 7308 John.McClory@afit.edu